



Human Postural Stability Models

Final Report

*Rob Langlois
Nicholas Bourgeois
Michael James Leveille
Heather Morris
Anne Marie Wice
Carleton University*

*Prepared By:
Department of Aerospace and Mechanical Engineering
Carleton University
1125 Colonel By Drive
Ottawa, ON K1S 5B6*

Contract Number: W7707-115204/001/HAL

Contract Scientific Authority: Kevin McTaggart, 902-426-3100 x253

The scientific or technical validity of this Contract Report is entirely the responsibility of the Contractor and the contents do not necessarily have the approval or endorsement of the Department of National Defence of Canada.

Defence R&D Canada – Atlantic

Contract Report
DRDC Atlantic CR 2013-083
November 2013

This page intentionally left blank.

Human Postural Stability Models

Final Report

Rob Langlois
Nicholas Bourgeois
Michael James Leveille
Heather Morris
Anne Marie Wice

Prepared by:

Department of Aerospace and Mechanical Engineering, Carleton University
1125 Colonel By Drive, Ottawa, Ontario, K1S 5B6

Contract Number: W7707-115204/001/HAL

Contract Scientific Authority: Kevin McTaggart 902-426-3100 x 253

The scientific or technical validity of this Contract Report is entirely the responsibility of the Contractor and the contents do not necessarily have the approval or endorsement of the Department of National Defence of Canada.

Defence Research and Development Canada – Atlantic

Contract Report

DRDC Atlantic CR 2013-083

November 2013

Abstract

During naval operations in waves, loss of postural stability by crew members can cause degradations to operational effectiveness and safety. Motion-induced interruptions (MIIs) are often predicted using simplified models that assume a human being to be a rigid body. The accuracy of such models is often limited because they ignore the complexity of human dynamics. This report describes new postural stability models that consider the dynamics of humans subjected to external motions. The resulting models were validated experimentally at full scale using purpose-built physical apparatus representing the stability and load models as well as the coupling link between them. A comprehensive series of parametric experiments using the developed hardware was performed. The resulting validated models were then implemented in a distributed simulation environment.

Résumé

Pendant les opérations de navigation dans les vagues, la perte de stabilité posturale chez les membres de l'équipage peut entrainer une baisse de l'efficacité opérationnelle et constituer une menace pour la sécurité. Les interruptions induites par le mouvement (IIM) sont souvent prédites à l'aide de modèles simplifiés qui reposent sur le postulat voulant que l'humain soit un corps rigide. Or, l'exactitude de ces modèles est souvent limitée, car ces derniers ne tiennent pas compte de la complexité de la dynamique du corps humain. Ce compte rendu décrit de nouveaux modèles de stabilité posturale qui prennent en compte la dynamique d'humains soumis à des mouvements externes. Les modèles qui en résultent ont été validés à l'aide d'expériences réalisées à pleine échelle au moyen d'un accessoire fabriqué sur mesure représentant les modèles de stabilité et de charge ainsi que la relation de couplage entre les deux. Plusieurs expériences paramétriques exhaustives ont été menées avec le matériel fabriqué. Par la suite, les modèles validés dérivés ont été appliqués dans un environnement de simulation réparti.

This page intentionally left blank.

Executive summary

Human Postural Stability Models

Rob Langlois, Nicholas Bourgeois, Michael James Leveille, Heather Morris, Anne Marie Wice; DRDC Atlantic CR 2013-083; Defence Research and Development Canada – Atlantic; November 2013.

Background: During naval operations in waves, loss of postural stability by crew members can cause degradations to operational effectiveness and safety. Motion-induced interruptions (MIIs) are often predicted using simplified models that assume a human being to be a rigid body. The accuracy of such models is often limited because they ignore the complexity of human dynamics.

Principal results: This report describes new postural stability models that consider the dynamics of humans subjected to external motions. The resulting models were validated experimentally at full scale using purpose-built physical apparatus representing the stability and load models as well as the coupling link between them. A comprehensive series of parametric experiments using the developed hardware was performed. The resulting validated models were then implemented in a distributed simulation environment.

Significance of results: The validated models of postural stability could be used to obtain improved predictions of motion-induced interruptions during naval operations in waves. These models could be used to develop improved seakeeping criteria for naval ship design.

Future work: DRDC Atlantic is working on visualization of human postural stability as predicted by new dynamic models.

Sommaire

Human Postural Stability Models

Rob Langlois, Nicholas Bourgeois, Michael James Leveille, Heather Morris, Anne Marie Wice ; DRDC Atlantic CR 2013-083 ; Recherche et développement pour la défense Canada – Atlantique ; novembre 2013.

Contexte : Pendant les opérations de navigation dans les vagues, la perte de stabilité posturale chez les membres de l'équipage peut entraîner une baisse de l'efficacité opérationnelle et constituer une menace pour la sécurité. Les interruptions induites par le mouvement (IIM) sont souvent prédites à l'aide de modèles simplifiés qui reposent sur le postulat voulant que l'humain soit un corps rigide. Or, l'exactitude de ces modèles est souvent limitée, car ces derniers ne tiennent pas compte de la complexité de la dynamique du corps humain.

Principaux résultats : Ce compte rendu décrit de nouveaux modèles de stabilité posturale qui prennent en compte la dynamique d'humains soumis à des mouvements externes. Les modèles qui en résultent ont été validés à l'aide d'expériences réalisées à pleine échelle au moyen d'un accessoire fabriqué sur mesure représentant les modèles de stabilité et de charge ainsi que la relation de couplage entre les deux. Plusieurs expériences paramétriques exhaustives ont été menées avec le matériel fabriqué. Par la suite, les modèles validés dérivés ont été appliqués dans un environnement de simulation réparti.

Portée : Les modèles validés de stabilité posturale pourraient servir à obtenir de meilleures prédictions des interruptions induites par le mouvement pendant les opérations de navigation dans les vagues. Ces modèles pourraient être utilisés pour élaborer de meilleurs critères de tenue en mer à prendre en compte dans la conception des navires.

Recherches futures : RDCC Atlantique mène des recherches sur la visualisation de la stabilité posturale chez l'humain prédite par les nouveaux modèles de dynamique.

Table of contents

Abstract	i
Résumé	i
Executive summary	iii
Sommaire	iv
Table of contents	v
List of figures	ix
List of tables	xvi
1 Introduction	1
2 Literature Review	3
2.1 Introduction	3
2.2 Physiology of Human Postural Stability	3
2.3 Postural Stability Modelling	4
2.4 Laboratory Experiments and Development of Control Strategies	13
2.5 Motion Induced Interruptions	21
2.6 Discussion	25
2.7 Conclusion	28
3 Development of Motion Induced Interruption (MII) Models	29
3.1 Inverted Pendulum	29
3.1.1 Translation	30
3.1.2 Rotation	34
3.1.3 Combined Dynamic Equations	36
3.1.4 Ankle Moments	37
3.1.5 Implementation	38

3.2	Three-dimensional Graham Model	38
3.2.1	Kinematics	40
3.2.2	Dynamics	41
3.2.3	Implementation	43
3.3	Computational Validation	44
3.3.1	Experimental Validation	49
3.4	MII Detection	50
3.4.1	Standard Indices	50
3.4.2	Modified Indices for a Generic Footprint	56
4	Development of Unsteady Shipboard Load Models	59
4.1	Pendulating Load	59
4.2	Cart Load Model Derivation	59
4.3	Model Definition and Coordinate Systems	59
4.4	Kinematics for Two Body Cart	60
4.4.1	Translating Mass	60
4.4.2	Rotating Mass	61
4.5	Dynamics for Two Body Cart	63
4.5.1	Linear Dynamics of the Translating Mass	63
4.5.2	Angular Dynamics of the Translating Mass	66
4.5.3	Linear Dynamics of the Rotating Mass	67
4.5.4	Angular Dynamics of the Rotating Mass	70
4.6	Interface Force	71

5	Physical Validation Experiment	73
5.1	Mechanical Hardware	73
5.1.1	Scale Assessment	73
5.1.2	Actively Controlled Spatial Inverted Pendulum	75
5.1.3	Pendulating Load	79
5.1.4	Cart Load	81
5.1.5	Tension/Compression Link	83
5.1.6	Safety Structures	83
5.2	Instrumentation	85
5.2.1	Spatial Inverted Pendulum Rotations and Mounting Interface Reactions	85
5.2.2	Pendulating Load Rotations	85
5.2.3	Cart Load Displacement and Rotation	87
5.2.4	Tension/Compression Link Interface Force	87
5.2.5	Mass Properties	89
5.3	Control and Data Acquisition	89
5.4	Experimental Validation of the Graham and Inverted Pendulum Stability Models	90
5.5	Computational Validation of the Cart Load Model	95
5.6	Validation of the Graham and Inverted Pendulum Stability Models Coupled to the Pendulum and Cart Loads through Experimentation	105
6	Implementation and Verification of Federate Form	115
6.1	Development Environment	115
6.1.1	VFD-RT Environment	116
6.2	VFD-RT Verification	121

7	Development of Model Tuning/Calibration Approach	125
7.1	Motivation	125
7.2	Equipment	125
7.3	Safety	126
7.3.1	Participant Health	128
7.3.2	Waiver	128
7.3.3	Ethics Approval	129
7.4	Experiment Descriptions	129
7.4.1	Human Subject Only	129
7.4.2	Human Subject and Hanging Mass	129
7.4.3	Human Subject and Cart	129
8	Conclusion	131
	References	133
	Annex A: Matrices $\left[\dot{T}_{SHIN}\right]$ and $\left[\ddot{T}_{SHIN}\right]$	141
	A.1 Matrix \dot{T}_{SHIN}	141
	A.2 Matrix \ddot{T}_{SHIN}	142
	Annex B: Mass Property Data Sheets	143
	Annex C: Sample Input Files	147
	Annex D: Software Archive	151
	Annex E: DEPSM User Guide	153
	Annex F: VFD-RT User Guide	155

List of figures

Figure 1:	Feedback postural stability model	4
Figure 2:	Golliday et al. two-link inverted pendulum model	6
Figure 3:	Hemami et al. three-link inverted pendulum model	6
Figure 4:	Koozekanani four bar linkage model	8
Figure 5:	Hemami et al. two link inverted pendulum model with interface forces.	9
Figure 6:	Barin multilink inverted pendulum model.	10
Figure 7:	Iqbal et al. frontal postural stability model	11
Figure 8:	Hemami et al. muscle model for three link pendulum	13
Figure 9:	Moments on the Graham MII Model	22
Figure 10:	Frontal and sagittal plane models for articulated postural model .	24
Figure 11:	Schematic illustration of a single-link spatial inverted pendulum .	30
Figure 12:	Schematic illustration of PSM3D file structure	39
Figure 13:	Coordinate systems used in the derivation of three-dimensional Graham shipboard postural stability model	40
Figure 14:	Forces acting on the three-dimensional Graham model.	41
Figure 15:	Longitudinal force (F_x) for typical ship motion computed using GRM3D and PSM3D	45
Figure 16:	Lateral force (F_y) for typical ship motion computed using GRM3D and PSM3D	46
Figure 17:	Vertical force (F_z) for typical ship motion computed using GRM3D and PSM3D	46
Figure 18:	Longitudinal moment (M_x) for typical ship motion computed using GRAM3D and PSM3D	47
Figure 19:	Lateral moment (M_y) for typical ship motion computed using GRAM3D and PSM3D	47

Figure 20:	Vertical moment (M_z) for typical ship motion computed using GRM3D and PSM3D	48
Figure 21:	Experimental apparatus	49
Figure 22:	Representative surge, sway, and heave ship motions scaled to remain within motion platform workspace	51
Figure 23:	Representative roll, pitch, and yaw ship motions scaled to remain within motion platform workspace	52
Figure 24:	Longitudinal force (F_x) for typical ship motion measured experimentally and simulated using GRM3D	53
Figure 25:	Lateral force (F_y) for typical ship motion measured experimentally and simulated using GRM3D	53
Figure 26:	Vertical force (F_z) for typical ship motion measured experimentally and simulated using GRM3D	54
Figure 27:	Longitudinal moment (M_x) for typical ship motion measured experimentally and simulated using GRM3D	54
Figure 28:	Lateral moment (M_y) for typical ship motion measured experimentally and simulated using GRM3D	55
Figure 29:	Vertical moment (M_z) for typical ship motion measured experimentally and simulated using GRM3D	55
Figure 30:	Sliding and tipping indices based on GRM3D simulation results	56
Figure 31:	Normal force location to counteract the tipping moments on the block model with a generic footprint	57
Figure 32:	Determining the location of the normal force by the angle between the vertex points on the polygon footprint	58
Figure 33:	Coordinate systems used in the derivation of in-plane cart load model	60
Figure 34:	Free body diagram of the two cart masses with the state variables	64
Figure 35:	Schematic representation of postural stability models interacting with the pendulating load and cart load	72

Figure 36: Directed element model	72
Figure 37: Experimental set-up for spatial inverted pendulum stability model coupled with pendulating load model	74
Figure 38: Spatial inverted pendulum model	75
Figure 39: Inverted pendulum articulation motor	76
Figure 40: Inverted pendulum straight gearbox	76
Figure 41: Inverted pendulum right-angle gearbox	77
Figure 42: Inverted pendulum custom-designed universal joint	78
Figure 43: Stress analysis results for the universal joint	78
Figure 44: Solid model of the pendulating load arrangement	79
Figure 45: Displacement analysis results for the pendulating load	80
Figure 46: Stress analysis results for the pendulating load	80
Figure 47: Stress analysis results for the pendulating load securing pin	81
Figure 48: Cart load translating base design	82
Figure 49: Cart load displacement analysis results	82
Figure 50: Solid model of the assembled cart load arrangement	83
Figure 51: Implementation of the tension/compression link with the pendulating load model	84
Figure 52: Implementation of the tension/compression link with the cart load model	84
Figure 53: Inverted pendulum base load cell	86
Figure 54: Configuration of OptiTrack system	86
Figure 55: Cart load encoders	87
Figure 56: Cart load translational encoder interface wheel	88
Figure 57: Omega Engineering LC-202 load cell	88

Figure 58:	Omega Engineering DMD-464 strain amplifier	89
Figure 59:	High-level view of control and data acquisition components	91
Figure 60:	Coordinate systems for the experimental apparatus compared to the dynamic model	93
Figure 61:	Example of breaking moment into force and position vector components	94
Figure 62:	Longitudinal force (F_x) computed using GRM3D and the load cell results from the experimentation	96
Figure 63:	Lateral force (F_y) computed using GRM3D and the load cell results from the experimentation	96
Figure 64:	Vertical force (F_z) computed using GRM3D and the load cell results from the experimentation	97
Figure 65:	Longitudinal moment (M_x) computed using GRM3D and the load cell results from the experimentation	97
Figure 66:	Lateral moment (M_y) computed using GRM3D and the load cell results from the experimentation	98
Figure 67:	Vertical moment (M_z) computed using GRM3D and the load cell results from the experimentation	98
Figure 68:	Longitudinal force (F_x) for computed using PSM3D and the load cell results from the experimentation	99
Figure 69:	Lateral force (F_y) for computed using PSM3D and the load cell results from the experimentation	99
Figure 70:	Vertical force (F_z) for computed using PSM3D and the load cell results from the experimentation	101
Figure 71:	Frequency response for the cart model stabilized with a spring and damper in translation for the case where $\zeta = 0.17$	101
Figure 72:	Frequency response for the cart model stabilized with a spring and damper in rotation for the case where $\zeta = 0.085$	104
Figure 73:	Longitudinal force (F_x) computed using GRM3D coupled to pendulum load and the load cell results from the experimentation	107

Figure 74:	Lateral force (F_y) computed using GRM3D coupled to pendulum load and the load cell results from the experimentation	107
Figure 75:	Vertical force (F_z) computed using GRM3D coupled to pendulum load and the load cell results from the experimentation	108
Figure 76:	Longitudinal moment (M_x) computed using GRM3D coupled to pendulum load and the load cell results from the experimentation	108
Figure 77:	Lateral moment (M_y) computed using GRM3D couple to pendulum load and the load cell results from the experimentation	109
Figure 78:	Vertical moment (M_z) computed using GRM3D coupled to pendulum load and the load cell results from the experimentation	109
Figure 79:	Longitudinal force (F_x) computed using coupled GRM3D coupled to cart load and the load cell results from the experimentation . .	110
Figure 80:	Lateral force (F_y) computed using coupled GRM3D coupled to cart load and the load cell results from the experimentation	110
Figure 81:	Vertical force (F_z) computed using coupled GRM3D coupled to cart load and the load cell results from the experimentation	111
Figure 82:	Longitudinal moment (M_x) computed using coupled GRM3D coupled to cart load and the load cell results from the experimentation	111
Figure 83:	Lateral moment (M_y) computed using coupled GRM3D coupled to cart load and the load cell results from the experimentation . .	112
Figure 84:	Vertical moment (M_z) computed using coupled GRM3D coupled to cart load and the load cell results from the experimentation . .	112
Figure 85:	Longitudinal force (F_x) for computed using PSM3D and the load cell results from the experimentation	113
Figure 86:	Longitudinal force (F_y) for computed using PSM3D and the load cell results from the experimentation	113
Figure 87:	Vertical force (F_z) for computed using PSM3D and the load cell results from the experimentation	114
Figure 88:	Visualization of DEPSM simulation environment and flow of solution	117

Figure 89: Connection and data transfer comparison between VFD-RT and HLA architectures	119
Figure 90: Connection and data transfer comparison between VFD-RT and HLA architectures	120
Figure 91: Longitudinal force (F_x) for computed using GRM3D from the VFD-RT and the DEPSM Simulation Environment	122
Figure 92: Longitudinal force (F_y) for computed using GRM3D from the VFD-RT and the DEPSM Simulation Environment	122
Figure 93: Vertical force (F_z) for computed using GRM3D from the VFD-RT and the DEPSM Simulation Environment	123
Figure 94: Reaction Moment (M_x) for computed using GRM3D from the VFD-RT and the DEPSM Simulation Environment	123
Figure 95: Reaction Moment (M_y) for computed using GRM3D from the VFD-RT and the DEPSM simulation environment	124
Figure 96: Reaction Moment (M_z) for computed using GRM3D from the VFD-RT and the DEPSM simulation environment	124
Figure 97: Moog 6DOF2000E motion system; available degrees of freedom . .	126
Figure 98: F-Scan insole	127
Figure 99: MOOG motion platform surrounded by OptiTrack camera system	127
Figure 100: Six-axis force/torque measurement system	128
Figure B.1: Inverted pendulum stability model with rotating mass and no additional mass plates, 1 of 2	144
Figure B.2: Inverted pendulum stability model with rotating mass and no additional mass plates, 2 of 2	145
Figure C.1: Sample GRM3D input file	148
Figure C.2: Sample PSM3D input file	149
Figure F.1: VFD-RT executable graphical user interface	156
Figure F.2: Connecting providers to the VFD-RT	158

Figure F.3: Verification of connection of providers to the VFD-RT	160
Figure F.4: Connecting clients to the VFD-RT	162
Figure F.5: PSM simulation running	164

List of tables

Table 1:	Simulation parameters used with GRM3D and PSM3D	45
Table 2:	Simulation parameters used with GRM3D and PSM3D	50
Table 3:	Simulation parameters used with GRM3D and PSM3D	92
Table 4:	Simulation parameters used for CRT3D validation	100
Table 5:	Results from translational forced frequency excitation on the cart for the case where $\zeta = 0.35$	100
Table 6:	Results from translational forced frequency excitation on the cart for the case where $\zeta = 0.5$	102
Table 7:	Results from translational forced frequency excitation on the cart for the case where $\zeta = 0.25$	102
Table 8:	Results from rotational forced frequency excitation on the cart for the case where $\zeta = 0.35$	102
Table 9:	Results from rotational forced frequency excitation on the cart for the case where $\zeta = 0.5$	103
Table 10:	Results from rotational forced frequency excitation on the cart for the case where $\zeta = 0.25$	103

1 Introduction

DRDC Atlantic and the Carleton University Applied Dynamics Laboratory both have experience in the modelling of human shipboard postural stability. Most notably, DRDC Atlantic developed (and tuned) a widely-used fixed rigid body postural stability model for quantifying the frequency of motion induced interruptions (MIIs). Since 2003, the Applied Dynamics Laboratory has been working with time-domain articulated shipboard postural stability models, and in particular exploring their potential for refining the prediction of MIIs. Experience to date suggests that each of these two modelling approaches has its relative merits. In either case, model excitation has been exclusively due to the internal inertia forces developed as a direct result of ship motion. Further, the stance of the simulated human has been assumed to be regular (feet aligned with the shoulder line and fixed). It is widely acknowledged that shipboard personnel experience external loads resulting from materials that they may be handling as part of their shipboard tasks. Examples include line tensions in ropes being used to stabilize slung loads such as small boats during launch and recovery, and equipment being manipulated by an overhead crane (such as during helicopter servicing); or loads resulting from interaction with mobile equipment such as trolleys, carts, and pallet lifts.

A recent collaborative research project between DRDC Atlantic and the Applied Dynamics Laboratory at Carleton University has investigated the interaction between typical unsteady shipboard loads and versions of available MII models. In terms of MII models, the widely-used planar Graham shipboard postural stability model has been extended to three dimensions, modified such that it can have an arbitrary footprint on the deck, generalized to support externally-applied loads (unsteady shipboard loads in this case), and generalized such that it can be placed and oriented arbitrarily on the ship. A second MII model based on a spatial inverted pendulum was also extended such that it could be acted upon by externally-applied loads, have an arbitrary footprint, and be placed and oriented arbitrarily on the ship. Unsteady load models corresponding to spatial shipboard pendulating loads and cart-type loads that are constrained to move in the plane of the ship deck were developed and interfaced to the MII models using a directed element that was also modelled as a separate entity. Each of these five models was implemented in a manner such that it could be integrated into a distributed computing environment. The models, once developed, were implemented and verified in the DEPSM simulation environment - a monolithic code that interacts with the models in the same manner they would be treated by a distributed simulation environment - and subsequently in the VFD-RT distributed simulation environment that was previously developed within the Applied Dynamics Lab. The VFD-RT architecture is such that models implemented in it can readily be ported to the widely-used High Level Architecture (HLA) simulation environment. Full-scale mechanical hardware was designed and built to validate each of the de-

veloped computational models. This hardware comprised a two-degree-of-freedom spatial inverted pendulum, a fixed spacial inverted pendulum representing Graham's model, a pendulating load, a two-degree-of-freedom cart load, and a directed force element. An extensive series of experiments was run wherein the models were tested individually and in combination on the six-degree-of-freedom motion platform available in the Applied Dynamics Lab. Validation results confirmed that the models have been derived and implemented correctly, and that the physical behaviour observed during the experiments involving an unsteady slung load and mobile-equipment-type load are captured by the models.

Full-scale mechanical hardware representing a two-degree-of-freedom spatial inverted pendulum or, when constrained, Graham's model; a pendulating load; a two-degree-of-freedom cart load; and the directed force element were all designed and built to validate the developed computational models. An extensive series of experiments was run wherein the models were tested individually and in combination on the six-degree-of-freedom motion platform available in the Applied Dynamics Lab. Validation results confirmed that the models have been derived and implemented correctly, and that the physical behaviour observed during the experiments involving an unsteady slung load and mobile-equipment-type load are captured by the models.

This report provides a description of the work completed in this project. Specifically, a detailed literature review is presented in Chapter 2. Chapter 3 presents the development of motion induced interruption (MII) models. Unsteady load models are presented in Chapter 4. The mechanical design, test plan, and results of the validation experiments are discussed in Chapter 5. Details of the computer implementation are contained in Chapter 6. Finally, suggestions for subsequent model tuning and calibration are discussed in Chapter 7.

2 Literature Review

2.1 Introduction

Humans are required to cope with a wide range of postural stability conditions ranging from deceptively simple tasks such as quiet standing to more complex dynamic actions such as walking and running. Over the years many models to describe human postural stability have been developed. These models vary widely in complexity, ranging from single segment inverted pendulums up to fully articulated multi-link skeletons [1]. Initially these models were developed with the goal of understanding the human sense of balance; however, more recently they have been identified as a potential tool in quantifying the effects of motion environments on human performance. This section presents a review of current and past research on human postural stability in a motion environment. It will begin by briefly explaining the biological systems which make up the human postural control system. With the basic concepts addressed, various biomechanical models of this control system and their development over the past four decades will be presented. Additionally, validation experiments executed to understand and improve these models will also be discussed. Having explored human postural stability research from the laboratory perspective, the applications of this knowledge will then be investigated. This includes quantifications of the risks related to working in a motion environment and the application of biomechanical principles to assessing the postural stability challenges related to the ship board motion environments.

2.2 Physiology of Human Postural Stability

The human body is inherently unstable due to the height of its centre of mass [2]. Consequently, constant minor postural adjustments and muscular torques are required simply to maintain an upright posture. Basic tasks such as quiet standing require an elaborate scheme of biological systems and algorithms for proper execution [2]. The human body contains three primary sensory mechanisms that are used during postural control: vision, proprioception, and the vestibular system. Each system provides a unique set of information related to the surrounding environment and the body's motion. This information is processed by the central nervous system in order to form an overall postural state which is then used to determine an appropriate mechanical response [2]. Each of these systems is most sensitive to a different set of postural disturbance types [2, 3]. As such, the relative importance of any individual system in the overall maintenance of postural stability varies relative to motion characteristics such as amplitude, frequency, and the available sensory information [3].

The typical approach to studying the biological control system which interprets these

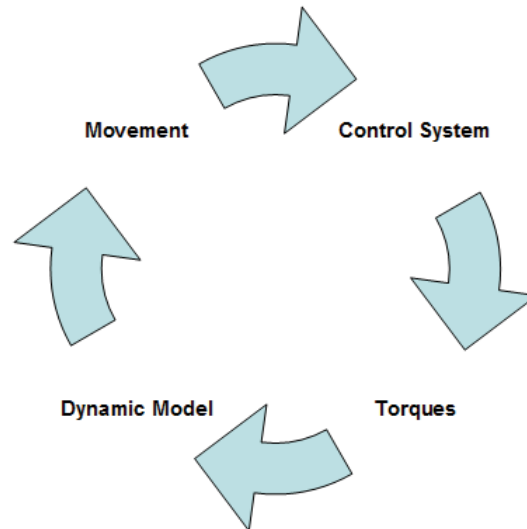


Figure 1: *Feedback postural stability model.*

sensory inputs is to represent it as a feedback model. Kinematic variables of the body as would be sensed by the three previously mentioned systems are input to a control block. This block then calculates the necessary torques and forces to be applied by the body's muscles to its various segments. The corresponding movements of the body can then be generated through the implementation of a dynamic model, which then completes the control loop by passing these calculated motions back to the control block as shown in Figure 1 [1].

More recent investigations have demonstrated that the postural control system is likely composed of both feedback and feedforward elements. It has been proposed by some researchers that the body's postural system incorporates a finely tuned set of predetermined reflexive postural responses. Although the central nervous system continuously receives postural state information, there is evidence that supports the hypothesis that it does not actually engage in postural control unless disturbances exceed a specific threshold [4, 5]. This serves to simplify the overall postural maintenance task in relatively stable environments and to compensate for time delays related to data transmission and feedback control decision processes.

2.3 Postural Stability Modelling

Postural stability models are models that define the dynamics of the human body [6]. Several of these models have been used to define the stability of humans during a walking gait and quiet standing. Although walking gait and quiet standing models are used for different applications, dynamic postural models can be used for both.

In 1972, Chow at Harvard University developed a stability model for a torso [7]. The model was to be used as the torso section of a more complex model for biped locomotion. This model consisted of a three rotational degrees of freedom single inverted pendulum. The equations of motion were derived using Lagrange's equation. The model allowed for the position of the base to follow a prescribed trajectory over time.

In relation to locomotion, Gubina et al., in 1974, developed a single-link inverted pendulum model with two moving massless legs modelled with force generators [6]. This model was constrained to the sagittal plane and modelled the torso dynamics supported by the two massless legs. The knee was modelled through the changing length of the legs and force generators to supply the torque. This model was also derived using Lagrange's equation. The equations were solved for the two translational degrees of freedom and one rotational degree of freedom of the torso.

In 1975, Murray et al. introduced a different modelling method for postural stability [8]. Unlike the pendulum models that were based more on the physical geometry of a human, Murray et al. suggested that a model could use the location of the centre of pressure on the surface and its distance within the stance. The validity of this type of modelling was verified by performing experiments involving subjects standing on a force plate, and asking them to perform various standing tasks. It was found that there were fluctuations in the centre of pressure location that were dependent on the individual.

Golliday et al., in 1976, developed a two-link inverted pendulum model designed for human locomotion [9]. Unlike the model derived by Gubina et al., the legs in this model included mass and inertia. The equations of motion were again derived using Lagrange's equation. Their model is illustrated schematically in Figure 2.

Postural stability models are dynamically unstable as humans are dynamically unstable. This requires that there be a control system in order to maintain the stability of the system. As a result, control system analysis is one of the applications for which postural models have been developed [10]. For these applications, the models do not need to be complex. In 1976, Hemami et al. used a single link inverted pendulum model to determine the applicable control algorithms.

In 1978, Hemami et al. developed a three link inverted pendulum postural model [11]. This model was constrained to the sagittal plane and had three links attached with revolute joints, as shown in Figure 3. This model was introduced to determine motions for several different tasks including sitting down, bending, and standing up. The model was derived using Newton-Euler dynamics and linearized about the applicable operating point. This model could be used to recreate typical human motions by applying an iterative solution method.

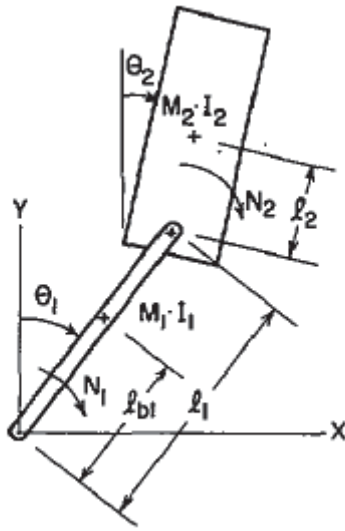


Figure 2: Golliday et al. two-link inverted pendulum model [9].

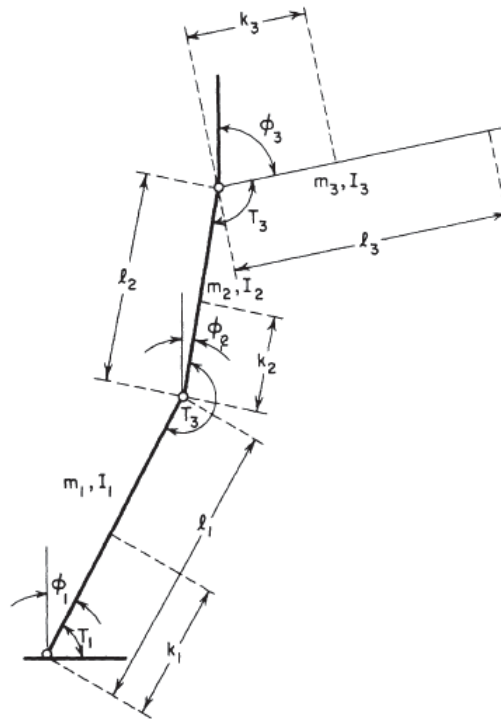


Figure 3: Hemami et al. three-link inverted pendulum model [11].

Hemami also conducted research with another team in 1978 to investigate a vestibular model. Humans control their posture using the vestibular system, which relies heavily on the otoliths and the semicircular canal within the ear [12]. The vestibular model that was used in 1978 was derived by Nashner [13]. This model of the vestibular system is defined in the frequency domain as a set of transfer functions modelling the effect from the two different parts of the vestibular system, the otoliths, and semicircular canals. The vestibular model was then applied to a single-link, and a double-link inverted pendulum postural model for control. It was found that the vestibular model could be used to successfully control the pendulum models.

Experimentation can be quite costly and time consuming. Mathematical models have been created to minimize the extent of required experimentation. In 1980, Koozekanani et al. developed a physical model in order to determine the centre of pressure of a four link inverted pendulum with a foot link [14], as seen in Figure 4. This model was not used for postural stability purposes on its own, but could be used with centre of pressure models for stability. This model did not have a control system; therefore, in order to calculate the centre of pressure, all the link properties, including the applied forces and torques, had to be known. Also, this model was limited to the sagittal plane.

In order to extend the Koozekanani et al. model to more of a postural stability model, in 1981, Stockwell et al. provided extensions to the model [15]. This model was extended with another linkage to represent the head motions and allow for more control based on the location of the centre of pressure of the linkages. Experimentation was conducted with human subjects in order to observe the postural sway effect. Stockwell suggested that a four link model should be sufficient to model the postural sway motions.

In 1982, Hemami et al. developed a spatial inverted pendulum model for use in locomotion studies [16]. The pendulum model was used to represent the torso motion for gait analysis. The model was derived using the Newton-Euler method. There are three constraining forces that act at the base attachment point of the linkage. An interesting by-product of the model is that this model not only describes the behaviour while attached at the base, but also indicates when the link slides or leaves the ground. The rotation about the linkage axis was assumed to be constrained by two possible types of constraints: a hard constraint, which the body cannot pass, and a soft constraint, which can be passed slightly. These constraints are modelled as a hard stop and as a spring/damper which restrict arm motion, respectively.

By 1984, Hemami et al. developed a model with a more biological basis. The models discussed up to this point have all had rigid connections between the links in order to lower the dimensionality of the system [9]. However, human linkages, for example the knee, are not rigidly connect at their joints [17]. For this reason Hemami et

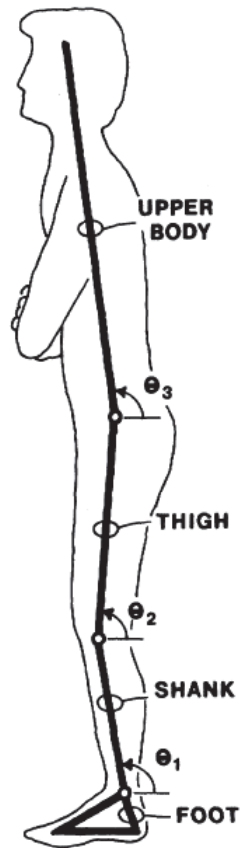


Figure 4: Koozekanani four bar linkage model [14].

al. extended a two-link model with an interface at each joint that could be used to represent tissue effects. The model can be seen in Figure 5. The model, combined with Lyapunov stability theory, was used to demonstrate stability [17].

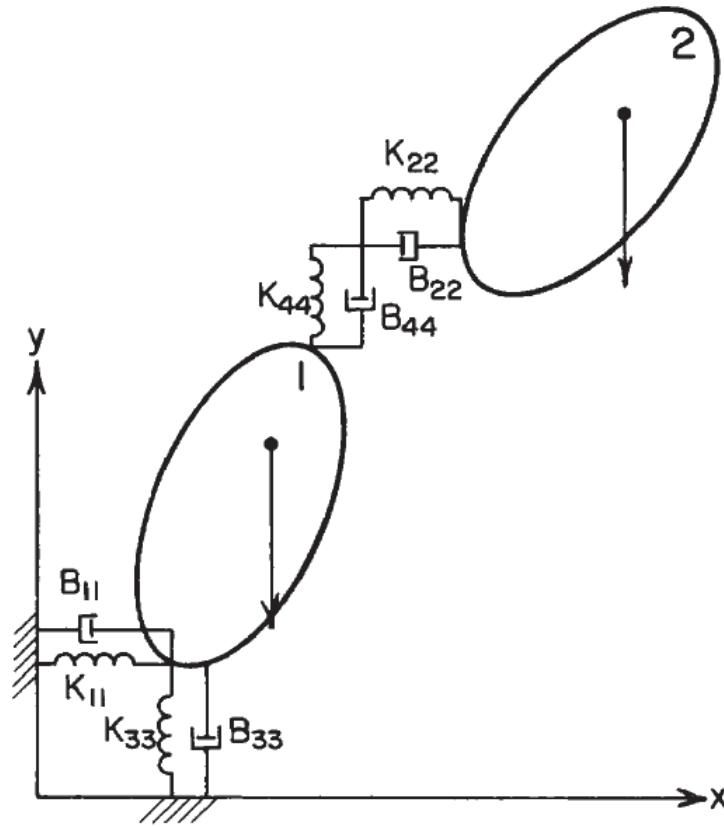


Figure 5: Hemami et al. two link inverted pendulum model with interface forces [17].

Peeters et al., in 1985, solved the single-link inverted pendulum model in the frequency domain and observed the spectral response of the system [1]. This analysis was performed to find the relationship between the motion of the body and the torque at the ankle joint. The results presented spectra in the frequency domain based on the torque.

A further development of the inverted pendulum model was achieved in 1989 by Barin. Barin created a linkage model that would allow for an arbitrary number of links in the system [18]. This model was also constrained to the two degree of freedom sagittal plane, and is illustrated in Figure 6. This model was developed to be a multi-use model given all the joint properties, and the number of links required for a particular application are known.

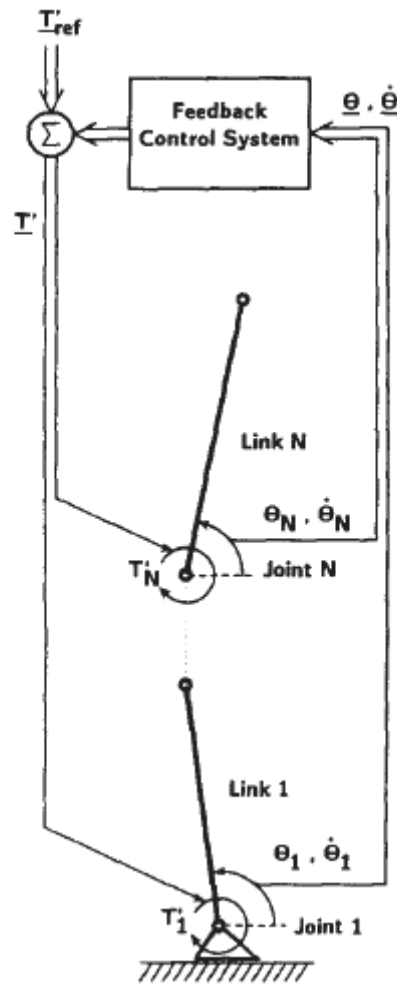


Figure 6: Barin multilink inverted pendulum model [18].

Riccio et al. researched the effects of dynamic motion and the stability of humans. This research was mostly qualitative and was observed through experimentation [19]. In previous pendulum models the orientation was set by a kinetic variable: the direction of the gravitational force [20]. The definition of balance of a human could be more dynamically defined due to the affect of the inertial effects on the vestibular system. This would provide insight into postural stability models with control systems. In 1993, Riccio et al. performed a series of experiments that submerged subjects in water in order to quantify the effect of these dynamic effects on human balance [21]. The dynamic effects were quantified as a relative tilt to the gravity vector after having undergone dynamic motions. It was found that the dominance of balance over gravity was related to this tilt.

The postural stability models presented up to this point have all been applied in the sagittal plane. In 1993, Iqbal et al. presented a model of dynamic effects occurring in the frontal plane, as seen in Figure 7. This model is a four link model having one link for each leg, one for the pelvis, and a fourth for the torso [22]. Each joint is modelled as a revolute joint such that the model is capable of representing relative motion at the hips as well as the ankles. The model was solved using a combination of perturbation methods and Taylor series expansions. It was used to investigate the control strategies of voluntary tasks as well as the sway motion effect.



Figure 7: *Iqbal et al. frontal postural stability model [22].*

Patton et al., during the period from 1997 through 1999, developed a series of experiments in order to determine the effects of the distance between the centre of mass and the base support on the model [23]. His experiments also investigated the effects of the velocity of the centre of mass and centre of pressure. The desired result from these experiments was a threshold of values which would determine whether a person would fall, or remain standing after a perturbation. The single-link inverted pendulum model was used for this investigation. The centre of mass and centre of pressure locations were known, and using the values obtained from the experiments, the stability thresholds were obtained [24]. Applying these thresholds to the pendulum model was used to determine if a person would be capable of remaining upright after experiencing a given perturbation.

In 1998, Slobounov et al. performed similar experiments to Patton's, but took into account the effect of age on the stability thresholds. This study did not compare the results to a postural stability model, and were only found to be threshold values for other models [25]. Subjects varying in age from 60 through 92 were tested in order to determine age affected the threshold of centre of pressure values within the stance width. It was found that the higher the age the lower the threshold is, which decreases the motion severity that will cause instability.

In 1998, Wu et al. developed a single link inverted pendulum model with two rotational degrees of freedom which allowed for a free moving base [26]. The base attachment point was modelled to be able to move in any direction. The only limitation was that any acceleration must remain constant. This model was designed solely as a mathematical model that could be used for other postural stability applications, such as trunk stability for locomotion [26]. The model was derived using Lagrangian dynamics. In their paper, the model was used to test control methods for the inverted pendulum. By 2000, Wu et al. had introduced a new postural stability model. The model was a planar two link inverted pendulum model [27]. The base of the pendulum was able to move freely. The acceleration of the base must also be constant. This model was designed for other postural stability models and to test different control methods.

Hemami et al., in 2006, modelled a three-link inverted pendulum in the sagittal plane that was attached to a motion platform. The model also included muscle models for the torques applied at the ankle, knees, and hips, as can be seen in Figure 8. Several experiments were conducted with subjects in order to validate the model. The results from the pendulum model were found to be similar to the calculated model results. The model results had smaller magnitudes than the corresponding human experiments.

In 2006, Nawayseh et al. performed experiments on the effect of oscillations on the postural stability of standing persons. A centre of pressure location model was used

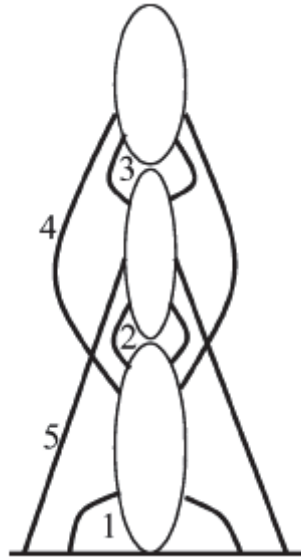


Figure 8: Hemami et al. muscle model for three link pendulum [28].

to determine the stability of a person. The experiments indicated that the higher the frequency of the oscillations the more likely the person was to fall.

Another method for determining the effect of the centre of pressure on stability was introduced by Schmid et al. in 2007. This method used a time to boundary method on four different parameters to analyze their effect on stability [29]. The time to boundary function estimated the time when the centre of pressure trajectory would cross the boundary thresholds, using a parabolic function containing position, velocity, and acceleration of the centre of pressure data. It was found that this method allows for the postural stability to be maintained.

A recent study performed in 2010 by Humphrey et al. used a three link planar inverted pendulum model [30]. The model used a muscle model for joint actuation as well as a vestibular model for feedback control. This model was used in the study of centre of pressure and centre of mass movements.

2.4 Laboratory Experiments and Development of Control Strategies

As one would expect, an extensive course of experimental research has been conducted alongside the development of the aforementioned biomechanical models in order to validate and improve the hypothesized control strategies which run them. Human

experimental trials are critical to generating physically-linked control concepts.

Starting with the earliest models in the 1970s, most modelling involved simulating and controlling two-dimensional inverted pendulums with various numbers of links. Many research projects trace back to a PhD thesis written by Nashner in 1970 [31]. Nashner discussed theories on how to control an unstable human postural stability model. He identified that there should be a difference between quiet standing, which does not include perturbing forces, and situations that require control in the presence of small perturbing forces. He also discussed what kind of state feedback various sensory organs can provide, and the different paths that feedback take through the body.

In practice, there tend to be two different approaches for modelling control of human quiet standing while undergoing small perturbations. One is to measure the positions of the centres of mass and pressure, monitor how they change, and apply a control scheme based on that information. The other approach is to monitor the joint positions and velocities and use feedback control to stabilize the model. Control methods are almost exclusively developed for the latter case since it allows full state feedback control, while the former method appears frequently when analyzing experimental data since using a force plate to measure centres of mass and pressure is simpler and less expensive than tracking body positions.

The simplest control method is to assume full-state feedback is available, such that the control inputs become linear combinations of the positions and velocities of each link. The inverted pendulum's dynamics are linearized about a vertical position which allows input gains to be calculated analytically to ensure stability of the system under small perturbations. Examples of this are available in the work done by Hemami and Golliday, and Geurssen et al., both in 1976 [9, 32].

In 1977, Hemami presented a step by step process of how to derive a model for an inverted pendulum and its control system [10]. He took the method one step farther and instead of designing the controller to maintain a stable upright position, it was instead extended to follow a specific trajectory (specified angles and angular velocities with respect to time). In that same year Hemami and Cvetkovic presented their work to combine the limited range of linear feedback with an extended positional range of on-off nonlinear feedback in order to simulate the human-link motions of bowing and bending [33]. They used Lyapunov stability methods to derive their controllers. They found that the nonlinear feedback was very effective in eliminating overshoots and that the settling time of the body was primarily a function of the torque limits rather than the dynamics of the linearized system. In 1978, Hemami and Jaswa presented a three-link inverted pendulum model with joints at the ankle, knee, and torso [11]. They found that a set of controller gains was not satisfactory, and that they required separate time-varying controller gains that were functions of the trajectory. In the

end, they concluded that it was not clear that such algorithms are utilized by humans in their everyday normal motions. Later in 1978, Hemami et al. presented a thorough methodological paper which includes a ‘vestibular model’, although it simply assumes that the vestibular system provides the central nervous system (CNS) with full state feedback [12]. They considered a two-link model with actuators at the ankle and hip. The torques were assumed to be linear combinations of the body and ankle angles and rates. All combinations of gains are considered, with extra detail on the stable cases which it was determined required at least three of the controller gains to be nonzero.

In 1980, Ishida studied the frequency response of subjects on a force plate undergoing pseudo-random linear disturbances [34]. A transfer function for ankle angle to ankle torque was fitted to the collected data, and a postural controller for a single link inverted pendulum was proposed. Comparing the data from trials in which the subject’s had their eyes open to those in which their eyes were closed, it was concluded that a human’s visual, vestibular, and proprioceptive sensors provide useful feedback in different frequency ranges.

In 1980, Koozekanani et al. derived the governing equations of a three-link inverted pendulum using d’Alembert’s principle, which they claimed was a form better suited for digital computation [14]. They matched the model with experimental data gathered by recording the positions of lights on subjects’ bodies, and were able to obtain rather accurate estimates of the centre of pressure movement from the measurement of body segment angles.

In 1980, Nashner performed experiments which monitored subjects’ muscle EMGs, while varying the orientation of the surrounding visuals, and the platform motions [3]. From his results he concluded that the CNS weights sensory input differently, and varies its outputs differently, depending on the state of a person’s surrounding environment.

In 1983, Hemami and Stokes presented a qualitative discussion on feedback and feed-forward paths in the control of human motion [35]. In 1984, Hemami and Chen presented their work which continued Hemami’s work from 1977, developing the model into a two-link planar biped, and determining its stability using quadratic Lyapunov functions [17].

In 1986, Nashner and Horak coined the terms ‘ankle strategy’ and ‘hip strategy’ [36]. The ankle control strategy is where compensatory torques are exerted about ankle joints, which restore equilibrium by moving the body’s centre of mass forward or backward. The hip control strategy is where compensatory horizontal shear force is exerted against the support surface with little, if any, ankle torque. Their final results conclude that subjects can synthesize a continuum of different postural movements

by combining these two distinct strategies in different magnitudes and temporal relations. These two strategies are frequently referred to in subsequent research papers from a variety of authors.

In 1987, Maki et al. completed a postural control model based on experimental data [37]. Their model indicated that a person was about to lose stability when their centre of pressure moved out of the range of their base of support.

In 1989, Barin successfully matched experimental data to a variety of postural stability models [18]. Single, double, triple, and quadruple inverted pendulum models were developed. An experiment was performed where body positions were measured with a light/camera system. Centre of pressure data were estimated from the body motions. Centres of pressure were also measured with a force plate, and the comparisons of the two values were used to evaluate how well each pendulum model estimated the centre of pressure. Next, experiments were performed where Barin attempted to match control algorithms to each model by exposing each subject to short, quick accelerations, forward and backward. To calculate control gains, the motion analysis equations were solved once to get the torques, followed by an N-dimensional regression analysis to get the control inputs. It was successfully shown that the four-link model along with the linear feedback loop provided accurate representation of human postural control for the given test conditions. Barin did not observe differences in the control gains for eyes open versus eyes closed or for forward versus backward perturbations, but did observe a significant difference between male and female subjects. Further testing indicated that at least one angular velocity feedback was needed to achieve a stable control system. Unstable responses were achieved for cases where angles and rates were only obtained from one segment, or in which one of the torques was assumed to be uncontrolled.

Research continued at a steady pace in the 1990s, including expanding simulated control strategies beyond simple linear methods. In 1990, Horak et al. proved through experimentation that both somatosensory and vestibular sensor information play important roles in the selection of postural movement strategies appropriate for their environmental contexts, as studied earlier by Nashner [38]. Horstmann and Dietz experimented with the effect of removing the influence of gravity on muscles by putting people in water (simulated microgravity) [39]. They wanted to determine whether contact force dependence was related to receptors within the skeletal connections or the joints.

In 1991, He et al. presented their work using an Linear Quadratic Regulator (LQR) for tuning controller gains [40]. They used small perturbation linear control theory and experimented with a variety of inputs, not limited to standard state feedback consisting of the positions of each joint. Muscle structure and behaviour was included in their model such that the state feedback comprised the elongation and rate of

change of elongation of the muscles at each joint. In 1992, Hasan et al. attempted to use a neural network to design a postural stability controller [41]. Their motivation was that most controllers that are designed to stabilize biped models use general linear feedback, and the resulting behaviour is over damped and does not demonstrate the postural sway observed in humans. They used a double inverted pendulum, and their results showed that the learning strategy of the neural network could accurately match the recorded control patterns, and that over time the neural network learned to propagate a sequence of appropriately signed torques such that posture could be maintained for increasing durations.

In 1993, Kuo and Zajac presented a three-link (ankle, knee, hip) model and studied the possible accelerations that it could experience using different muscle exertion combinations [42]. They found that independent control of specific joints was relatively difficult to achieve. They also found that both ankle and hip strategies are effective at accelerating the centre of mass horizontally, but that the hip strategy requires less neural effort for a given magnitude of horizontal acceleration. In 1995, Kuo presented a new complex controller combining a parametrized LQR with a linear quadratic estimator (LQE) which would provide state feedback and estimation [43]. Together these two components formed a linear quadratic Gaussian (LQG) optimal controller. Kuo indicated that while there was no evidence that the CNS operates like an LQR controller, there were plausible arguments that it should behave like one. Another notable statement made by Kuo was that an important consideration in a biological system is that the controller must be stable even with substantial transmission delays.

In 1997, Patton et al. furthered the research on predicting postural instability based on a subject's centre of pressure [23]. Predicted stability limits from their centre of pressure calculations, from an inverted pendulum model, and from experiments correlated very well. Tian and He created a four-link inverted pendulum model which included an additional joint at the toes so that the foot could be treated as a link rather than a point contact [44]. The control system used a LQR to calculate the gains, and also included a time delay. The proposed control system used internal models to compensate for the delay and to prepare for a predictable perturbation.

In 1998, Henry et al. investigated which muscles are used to react to sudden disturbances in both anterior/posterior (A/P) and lateral directions [45]. Results from the study indicated that control of postural stability may be similar for A/P and lateral translations within the restrictions of body geometry. Winter et al. studied and modelled how the CNS controls and maintains an upright standing posture, without any external perturbations [4]. Their model consisted of an inverted pendulum with springs substituted for muscles. Their results suggested that there is no reactive control in quiet standing, and that visual and vestibular inputs have no effect.

In 1999, van der Kooij et al. presented a model of additional complexity [46]. In this case they used a three-link inverted pendulum and a controller based on optimal estimation theory. Similar to the linear quadratic Gaussian controller developed by Kuo, this one includes a predictive component in order to compensate for time delays. Simulated sensory information provided by a variety of sources is combined in an extended Kalman filter in order to estimate the current body position, which is then corrected by the time-delayed sensory information. The model was developed further in 2001 by developing the predictive component into an adaptive estimator model of spatial orientation [47]. This new model weighted the difference between expected and actual sensor signals as a function of environmental conditions.

Corna et al. performed an experiment that involved exposing subjects to oscillating anterior/posterior motions [48]. They observed that when subjects had their eyes open, control of body position was similar to a flexible pendulum, and with eyes closed, the control changed to that of an inverted pendulum.

Also in 1999, He and Wang developed a controller for a four-link inverted pendulum model with joints at ankle, knee, and hip [49]. They observed in previous work that LQR control was effective under small perturbations, but performed poorly for large perturbations, and when the nonlinearities of the model became too significant. To deal with this they developed a fuzzy control system to improve system performance outside of the linear region. They used 28 fuzzy rules, which were derived from experimental findings. LQR was used instead of fuzzy control in the linear region as it helped reduce the complexity of the fuzzy controller. In later work, this model was extended to include six degrees of freedom by the addition of a rotational joint at the toe, and with variables indicating the position (x,y) of the foot [50]. Additional details on the fuzzy logic controller that its input is the centre of mass of the body.

Wu developed an inverted pendulum model that used horizontal and vertical forces applied at the base, instead of a fixed base [51]. The base was modelled this way as an attempt to model the cartilage and ligament behaviour of natural systems. Rather than maintaining an operating point, the control system was designed to track a trajectory while keeping the base point stationary. Lyapunov's stability theory was used to develop a piecewise continuous controller which then had its discontinuous terms replaced with smooth functions in order to eliminate potential chatter in the controller. In 2000, Wu and Swain continued this work in order to expand the model to a double inverted pendulum [27].

In 2000, Ito and Kawasaki developed a new controller based on foot-ground reaction forces [52]. They determined that in order to maintain balance it is necessary that the ground reaction forces be kept positive at both ends of the foot. Mihelj et al. studied the use of the ankle strategy with experiment subjects [53]. They observed that when the ankle strategy is sufficient to maintain balance, a mostly linear relationship

between ankle torque and ankle angle was observed, resulting in a constant stiffness.

In 2001, an experiment was performed by Bothner and Jensen to determine whether continuous external perturbations could have a stabilizing effect on postural stability rather than simply a destabilizing effect that the CNS would have to compensate for [5]. Within their small sample group they did observe this effect, and concluded that continuous disturbances must be accounted for in this way in balance research. Another experiment, performed by Matjacic et al., measured muscle behaviour for reactions to displacements separately in only the A/P plane and then both in the A/P and lateral plane [54]. Displacements were small enough that only the ankle strategy was required to maintain balance, and the reactions in combined directions were the same as the ones in the A/P direction only. Their results indicated that for moderate strength perturbations, the CNS decouples the control space into two orthogonal directions. In other work Micheau et al. developed and validated a postural stability control system for an inverted pendulum with time delays and lambda control [55].

In 2003, Iqbal et al. presented their work on a four segment planar rigid body model with joints at the ankle, knee, and hip [56]. In their model the length of the stationary foot segment was used to define the base of support in the A/P direction. They used passive stiffness feedforward control, and active feedback control. The feedback control contained linear combinations of position, velocity, and a third nonlinear term that was intended to represent physiological restraints on the joint range of motion. Another interesting aspect of this model was that the initial conditions of the experiment started with the knee at a 45 degree angle, which is well beyond the linear control range of upright stance. Roy and Iqbal presented another model involving an inverted pendulum, PID controller, second-order muscle model, and a first-order Golgi tension organ model [57]. This work was an attempt to model short, medium, and long muscle invariant latencies that the CNS uses to maintain balance. The model included dual position and velocity feedback loops from multiple muscle spindle organs, and a force feedback from a Golgi tension organ.

In 2004, Frazier and Chouikha presented a new nonlinear postural controller [58]. It was an optimal switching state controller which also contained a learning algorithm intended to imitate the CNS, providing an improved controller over a LQG controller. “The mathematical principles of ‘systems with impulse effect’ (SIE) provide a unique ability to incorporate learned strategies of the examined actuators. Using the discovered strategies, a novel control model incorporating a state observer, the extended Kalman filter, and a linear quadratic regulator, to provide postural stability, was assembled” [58].

In 2005, Lydoire and Poignet presented a nonlinear model predictive controller via interval analysis [59]. Their work was successful, but the controller performance was not as good as previous models.

In 2006, Hemami et al. presented experimental verification of the human ankle strategy [28]. They used a four-link inverted pendulum and exposed it and experimental subjects to short forwards and backwards accelerations. They observed that where the ankle strategy is applied, subjects and the model behaved like a single link inverted pendulum. Muscle stiffness control was used in their model to maintain upright stance under no external perturbations. Jiang and Kimura developed a model for study of frontal plane sway [60]. They developed a novel model which takes into account the shape of the femur and pelvis for their centre of pressure calculations. They use a double inverted pendulum for their dynamics and develop a PID controller analytically with parametrization that lets them easily match it to experimental data. The controller also includes noise added to the control signal. Scrivens et al. also developed a frontal plane stability model [61]. They specifically tailored it to the frontal profile of a cat and actuated the model at the hips only. They also developed a simplified cat robot to test their control system. In virtual reality research, Virk suggests the possibility of re-weighting redundant control inputs in the CNS in real-time as a method for adaptive control [62].

Bustamante Valles et al. performed experimental validation of centre of pressure calculations in three dimensions [63]. Separate inverted pendulum models were used for each plane. A PID controller was used with time-delayed feedback. Their work was continued in 2008 by correlating their model with data from child patients [64].

In 2007, Pilkar et al. performed experiments with cyclic sway on a motion platform involving human subjects, and showed the presence of multiple frequencies in human sway response [65]. An inverted pendulum model was used, with the sum of torques at the ankle comprising of weight due to gravity, muscle forces, and a sway pattern generator. The PID controller gains were calculated as functions of the pendulum angle.

In 2009, Finley et al. performed an experiment in a slightly different way than past experiments [66]. They used real-time monitoring of muscle torques and angles to help subjects limit their ankle torques and angles to specific values. The experiment studied feedforward co-contraction and stretch reflex amplitude. They found that co-contraction magnitude scales with external torques and that reflex amplitude becomes attenuated. Xinjilefu and Michalska experimented with a new stochastic control method for controlling a double spatial inverted pendulum [67]. The method achieves control by minimization of the system Lagrangian. Unfortunately, the method fails in upright equilibrium, sometimes the approach does not find a control solution, and it is not yet implementable online.

In 2010, Hemami et al. proposed a new triple inverted pendulum model [30]. It incorporates three muscle pairs rather than simply using torque generators. “The model here allows for a sudden translational disturbance of the support surface, variation of

physical parameters, tuning of muscular inputs, prevention of hyperextension at the hip and knee joints, and addition of a vestibular term to the balance strategy” [30]. Also in 2010, Langlois presented the development of a spatial inverted pendulum postural stability model [68]. It implemented feedback control as linear combinations of the states, but also divided the feedback into separate stiffness, damping, and active control terms. Sovol et al. developed an automated method for calculating model coefficients from experimental data [69]. Their model included an inverted pendulum for each plane, PID controllers, and time delayed feedback.

Finally, in 2011, Davidson et al. used a neural search algorithm to calculate model parameters from data [70]. They used a 2D inverted pendulum with a PD controller, a time delay on state feedback, and stiffness and damping at the ankle joint.

2.5 Motion Induced Interruptions

Biomechanical postural stability models were initially developed with the goal of understanding the human sense of balance; however, more recently they have been identified as a potential tool in quantifying the effects of motion environments on human performance. For example, crew members working in a motion environment are required to perform a variety of physically and mentally demanding tasks such as walking, weapons loading, and lifting [71]. If the ability of the crew to complete these tasks is in any way impaired, the overall efficiency of the crew member decreases resulting in potentially increased costs and decreased effectiveness. Also, this may cause the crew member to become impaired to the point of endangering themselves. A means to quantify the performance degradation caused by the crew members adjusting balance was introduced by Baitis and Applebee in 1984 [72]. The performance of a crew member is said to be reduced if the person has a ‘motion induced interruption’ (MII) which is defined as an incident in which they must take a step, grab a hold, or stop what they are doing in order to maintain balance [73]. MII analysis requires knowledge of both the motion of the environment as well as its affects on subjects. Biomechanical models provide a means by which the human response can be predicted for a given set of motions in order to provide operational and design guidance.

Biomechanical models are used to observe the effects of the motion environment on the postural response. However, these models were not designed in such a way as to observe the possibilities of MIIs. Several different postural models have been developed for the specific purpose of determining the MII events.

The Graham rigid body model was first introduced in the early 1990s [74]. The model is based on a rigid block having humanoid mass, inertia, and support base properties. An MII is said to occur if the block has either a sliding event, or a tipping event. The occurrence of these events is identified by exceeding thresholds based on the

properties of the block. A sliding event is said to occur if the lateral forces exceed the opposing frictional capacity. The frictional capacity is calculated by a summation of the forces normal to the flat surface multiplied by the frictional coefficient of the surface. The lateral forces are found by a summation of the forces parallel to the flat surface. Initial tests conducted through observation of an unoccupied chair during ship motion indicated relatively good agreement between predicted slides for the chair and the actual slides observed. This is to be expected since the chair is simply a rigid body which has no dynamic characteristics to be accounted for [74]. A tipping event is said to occur if the moment about one of the model's feet falls to zero, and can be seen in Figure 9. This tipping model is used to predict when a person will be required to take a step or grab a support to maintain balance. These two thresholds are used to model when a person is most likely to take action in order to retain balance. These thresholds can be used in simple models such as the block on a deck, or include unsteady wind loading, or even be used in simple articulated models which define the person not as a simple block but as an inverted pendulum.

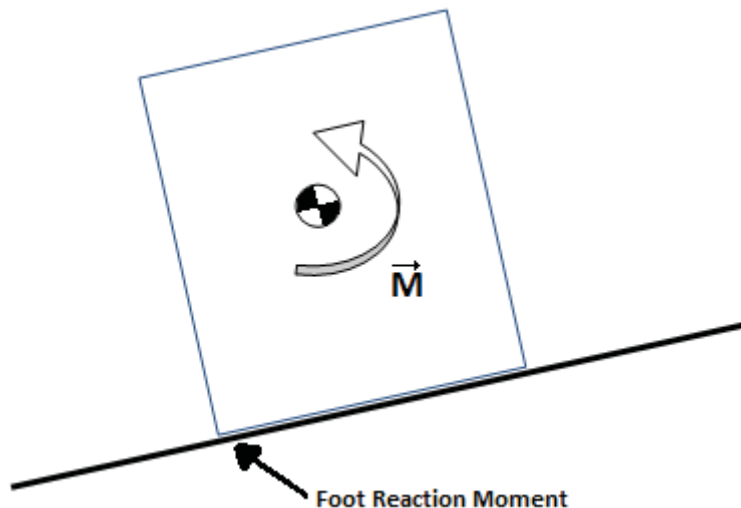


Figure 9: Moments on the Graham MII Model.

A research initiative established by the ABCD Working Group on Human Performance at Sea to explore human factors within the shipboard environment has resulted in an extensive set of experiments to investigate the performance characteristics of Graham's model. During the early 1990s, a large data set on human performance in the shipboard environment was produced at the National Biodynamics Laboratory (NBDL) in New Orleans. The experiments subjected 15 participants to two levels of ship motion severity using a large ship motion simulator platform. The subjects were required to complete a number of tasks during the motion profiles. Human postural response data from the tasks consisting of standing facing port and standing facing

aft were used by Lewis and Griffin to check the validity of the rigid body model and to investigate the potential application of more complex models to MII prediction, including parametric methods [75]. From these experiments it was proposed that Graham's model could be tuned to more accurately predict MIIs by empirically choosing tipping and sliding thresholds to match experimental MII occurrences. A similar adjustment process was recommended for the parametric models. Initially for the parametric model, MIIs were defined as points at which the centre of pressure exceeded the base of support limits. In practice the usable base of support region was found to be smaller than the theoretical maximum value. Based on this, it was suggested to adjust MII model thresholds accordingly.

A second series of experiments based on the initial NBDL investigations was conducted by the Defence Research Agency in the United Kingdom using a large motion simulator [76, 77, 78]. The ability of the simulator to provide motion cues in five degrees of freedom rather than the three used at the NBDL provided the opportunity to generate an improved set of postural response data relating to frontal plane MIIs. During the experiment subjects were required to complete several different tasks such as walking, weapon loading, and standing while being subjected to the NBDL motion profiles. As suggested by the NBDL experiments, empirical MII thresholds were determined for the rigid body MII model. In addition to the standing tasks, empirical model thresholds were determined for all of the experiment tasks despite the fact the model does not physically represent them. The tuned model was found to provide good predictions of MII occurrences in all cases although it under-predicted at high MII rates. A statistical model of MII occurrences was also investigated using the experimental data.

Experiments performed in 1993 by McIlroy and Maki investigated the psychological effect of allowing participants to either step to maintain balance, or not allowing them to do so [79]. The experiments conducted applied a perturbation in a single direction and the subject was either told they could or could not step. The results of the experiments determined that if a subject was allowed to step that the occurrences of stepping incidences increase in comparison to not being allowed to step. This indicates that there is a psychological effect involved when considering MII occurrences. In 1997, Maki and McIlroy investigated the likelihood of a person maintaining postural stability by using fixed stance recovery methods versus non-fixed stance methods [80]. The fixed stance methods include bending the knees or hips, applying a moment at the ankles, and similar methods. Non-fixed stance methods include grasping an external support or taking a step. The results of the experiment showed that the onset of non-fixed stance recovery methods occur well before the centre of mass has reached the stability limits. This implies that a person is likely to step well before the stability limits require it.

A method of articulated postural modelling was investigated by Mckee and Langlois

using a two-plane articulated model [81]. The model is defined by using a single degree of freedom inverted pendulum in the sagittal plane and a four bar linkage in the frontal plane, as illustrated in Figure 10. This model also used a controller for the ankle joint moments which were tuned based on experimental data recorded at the Naval Biodynamics Laboratory [82]. It was observed that the biodynamic model was predicting a slightly lower number of MII events than observed while the Graham model over predicted the number of MII events. This introduced the possibility of articulated models being a viable alternative for predicting MII events [81].

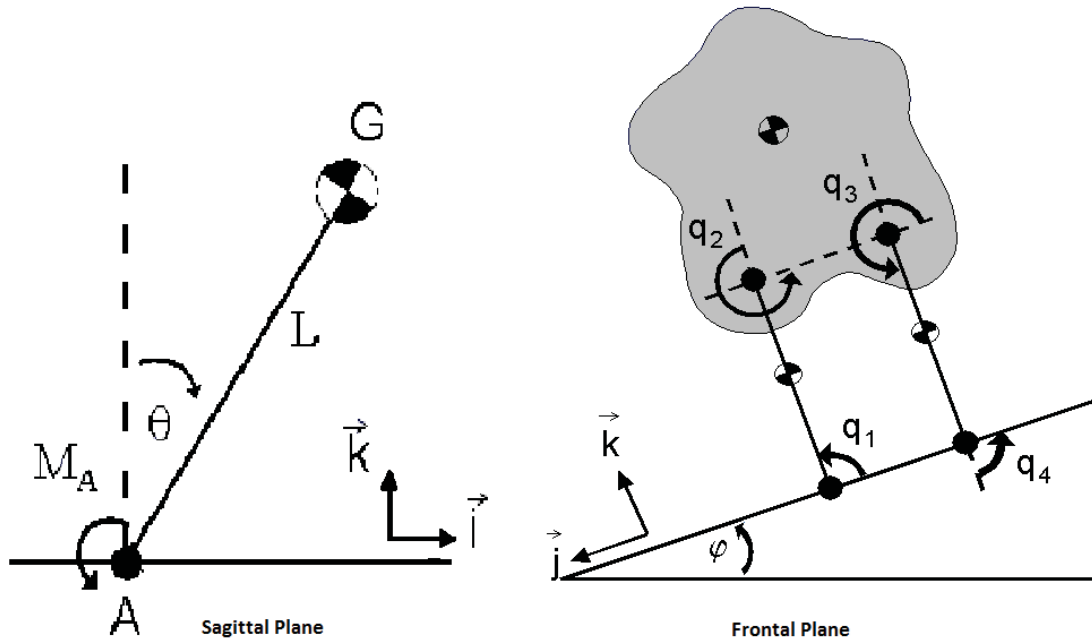


Figure 10: Frontal and sagittal plane models for articulated postural model [81]

An expanded inverted pendulum for modelling postural stability in a shipboard application was introduced by Langlois in 2010 [68]. The pendulum model was a three-dimensional model as opposed to classical models, some of which were limited to two dimensions. This model was also designed with the intention of predicting MII events. The model is derived by separating the translational and rotational components. The translational components are solved in order to find the forces acting at the base of the pendulum. The rotational components are solved using Euler's equation to determine the ankle yaw moment and inverted pendulum relative angular motions. For this solution, a controller is necessary to actively compute ankle moments to stabilize the inverted pendulum. The controller is tuned with applicable damping in order to maintain a vertical stance with respect to the gravity vector while predicting MII rate and times of occurrence based on available experimental data. MII detection in this

model is based on the two criteria defined in Graham's model. The sliding case is defined by a sliding threshold which is a function of the friction force and the vertical and lateral forces. A tipping case is defined by a tipping threshold which is a function of the moment and the forces acting on the body. The model was verified using a controller tuned to motion platform and available sea trial MII data. The model was verified for a single articulated segment and two revolute degrees of freedom.

Duncan et al. conducted a series of experiments on MII occurrences at sea [83, 84]. The experiments that were performed in 2009 used 11 participants to investigate the effect of thoracolumbar kinematics and foot centre of pressure on postural stability. The experiments required the subjects to perform two different tasks in different sea conditions aboard the Quest research vessel. The tasks comprised a neutral standing task and a standing task with feet shoulder width apart holding a stationary 10 kg load. The data collected for this experiment were the thoracolumbar kinematics, the centre of pressure velocity, and video data of MII occurrences. It was found from these experiments that during MIIs, the sudden postural adaptations resulted in significant increases in mean and peak thoracolumbar velocities. This showed that in order to maintain balance a combination of body and foot movements are needed. It also showed that the direction in which the subject was standing also affected the number of MII occurrences.

Experiments performed by Hasoon et al. in 2008 were designed to investigate the response of the subject as if they were an inverted pendulum [85]. The experiment was designed such that the subject was attached to a flat board in order limit the motions to the sagittal plane. The only control of balance strategy that the subjects could use based on the apparatus was the ankle strategy. The subject was then perturbed from the aft by varying degrees and whether the subject had to take a step in response to the perturbations was noted. The results from the experiment were compared to a postural pendulum model developed by Hof et al. [86]. The analysis of the data provided approximation curves of the centre of mass acceleration versus the severity of the perturbation.

2.6 Discussion

One purpose of this review was to determine the suitability of using an inverted pendulum model in the study of shipboard postural stability.

In general:

- Most of the postural stability models reviewed have either been used to match experimental data to a model, or to design a control system that maintains balance under perturbations. All of these models use one- to four-link inverted pendulums since their joints can be correlated to major joints in the human

stance. At minimum, every model that does not simply use centre of pressure or Graham's model for MII identification, incorporates a single-link inverted pendulum.

- Most of the experimental studies in postural stability use translational platform motions. It is rare to encounter studies that not only include pitch, roll, and heave motions, but that use them in combination as they would be encountered at sea. A practical reason for this is that designing a control system that is required to deal with a large assortment of disturbances is considerably more complicated. Additionally, only a handful of nonlinear spatial models have been developed. These are required when incorporating combinations of support surface angular displacements into a model.

Common points from postural stability models:

- Inverted pendulums are a common physical model. The number of links used reflects the complexity of the motion that is to be investigated, such as hip or knee motions. For simplicity of the mathematics, pendulum models with more than one link are commonly limited to the sagittal plane.
- There are very few models that address postural stability in the frontal plane. These models are few since experiments are usually more interested in finding the magnitude of the ankle strategy, or measurement of forward and backward tipping displacements.
- Several experiments have been performed that investigate the motions of the body centre of pressure by measuring forces at subjects' feet. A somewhat empirical model has been used in order to compare the centre of pressure motions with the stability of the model, where stability in this sense means that the model is still controllable or still standing up. These centre of pressure models are therefore dependent on the centre of pressure motions and need a separate model to determine their values.
- Postural stability models with inverted pendulums with more than one link can include interface forces at the connections. For some models the connection between the links is assumed to be a rigid single axis revolute joint, while others have been developed in order to see the effects of joint motion on the stability of the model.
- Several models include muscle models that calculate joint torques that reflect how human muscles operate. These models are mostly suited to investigating the magnitudes of the forces required in the muscle for the task which is a more specific topic than simply postural stability.

- The number of links used in the inverted pendulum model is related to what is being investigated. For studying the differences in the hip and ankle strategies, a single inverted pendulum is used for the ankle strategy and a double inverted pendulum is used for the hip strategy. A three link pendulum is used in cases where the knee flexion is also of interest. Four link inverted pendulums are used to model the motion of the head, which can have an influence on sensory vestibular models.

The following points summarize the common control components of postural stability control systems, and advances that have been added to them in order to more accurately reflect how human balance control actually works.

- It is a very common practice to linearize the model around the desired stability point. This allows control gains to be derived and tuned analytically to ensure stability. It is universally agreed that outside of a small operating range, linear control is not sufficient. In the last decade various nonlinear control methods have been attempted, with varying results.
- Time-delayed feedback is commonly incorporated in order to model time delays in the human central nervous system. Some models incorporate multiple feedback paths with distinct separate time delays.
- Some models use spring/damper elements to stabilize standing models at their equilibrium point so that under very minor perturbations the system does not require active control.
- State estimation is integrated into some models (eg., Kalman filters). It has proven to be useful for dealing with time delays, or fusion of multiple feedback signals.

Laboratory research studies of postural stability during support surface perturbation or in a motion environment have been ongoing for over four decades. Advances in experimental techniques and computational technology have allowed the simple single link models initially presented to develop into multi-link depictions of the human skeleton with simulated sensor organs and extensive muscle actuation systems. Although these models have been developed with the goal of understanding human postural control strategies and physiology, they also present the opportunity for greater understanding of the risks and effects associated with working and living in motion environments.

This literature review has shown that human postural stability has been and continues to be an active area of research fuelled by issues in various fields ranging from fundamental understanding of balance and human control mechanisms, to practical matters such as shipboard MII prediction. While the literature provides general guidance on modelling options, unique features of the shipboard motion environment and

particular role of the intended models necessitate the use of a specifically tailored approach to simultaneously meet basic requirements while remaining computationally and practically relevant.

2.7 Conclusion

Laboratory research studies of postural stability support surface perturbation or in a motion environment have been ongoing for over four decades. Advances in experimental techniques and computational technology have allowed the simple single-link models initially presented to develop into multi-link depictions of the human skeleton with simulated sensory organs and extensive muscle actuation systems. Although these models have been developed with the goal of understanding human postural control strategies and physiology, they also present the opportunity for application to understanding the risks and effects associated with working and living in motion environments. To date, actual application of the laboratory work has been limited to quantifying the effects of ship deck motion on crew performance. Models used in this field have progressed from a simple passive rigid block, to parametric models, and finally to an actively controlled multi-segment biomechanical representation of the human body. Although there are many unresolved issues within our understanding of the human postural control system, there currently exists a large and well established base of postural stability research which could be readily applied to investigations of motion environments beyond the ship deck.

3 Development of Motion Induced Interruption (MII) Models

Two postural stability models are developed and used in this project. The first is a single-segment inverted pendulum that has been generalized from a previously-developed model to allow for arbitrary placement on a ship, and externally-applied loads. The second model involved generalizing the Graham shipboard postural stability model to three dimensions, adding an externally-applied load, supporting arbitrary placement, and allowing arbitrary deck interface geometry. Both models are developed in this section.

3.1 Inverted Pendulum

Figure 11 provides a schematic representation of a single-segment spatial inverted pendulum postural stability model. Point A corresponds to the location of the interface between the ship and the inverted pendulum and point B corresponds to the centre of mass of the rigid articulated segment. Articulation of the rigid segment is tracked using the two generalized coordinates θ_i and θ_j corresponding to sequential roll and pitch motions of the articulated segment relative to the ship deck. Interface forces and moments are tracked by F_x , F_y , F_z and M_x , M_y , M_z , respectively. An externally-applied load acts at point C.

Four right-handed coordinate systems, labelled in rectangular boxes in Figure 11, are used in the model derivation and numerical solution. Each of the four coordinate systems is defined as follows:

- IN** The inertial coordinate system is a coordinate system that is either fixed or moving at constant velocity and is the coordinate system with respect to which ship motion is specified. It is defined by the $\mathbf{X} \cdot \mathbf{Y} \cdot \mathbf{Z}$ unit vector triad where the \mathbf{X} and \mathbf{Y} axes lie in a horizontal plane and \mathbf{Z} is directed positive up.
- SH** The ship coordinate system is fixed to the ship and located at the interface between the inverted pendulum model and the deck. It is defined by the $\mathbf{I} \cdot \mathbf{J} \cdot \mathbf{K}$ unit vector triad where the \mathbf{I} and \mathbf{J} axes correspond to the longitudinal and lateral directions, respectively, and \mathbf{K} is directed positive up in the ship's vertical direction.
- MO** The model coordinate system is collocated with the ship frame (SH) but is rotated by an angle β about the \mathbf{K} axis where the positive direction for β is consistent with the right hand rule. It is defined by the $\mathbf{x} \cdot \mathbf{y} \cdot \mathbf{z}$ triad.
- LO** The local coordinate system is collocated with the SH and MO coordinate systems but is attached to the articulated segment. The orientation of this co-

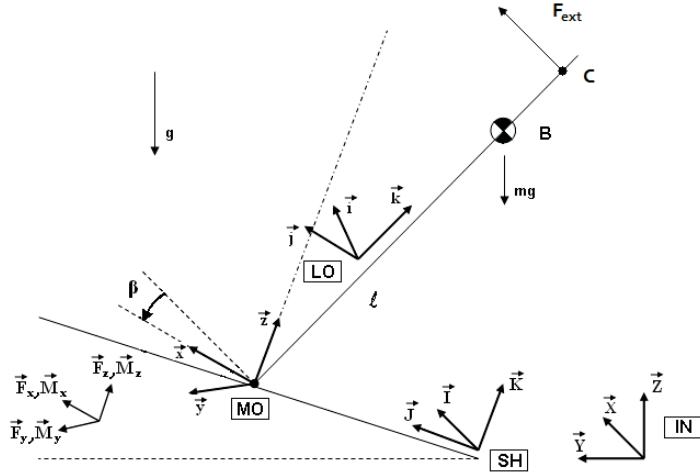


Figure 11: Schematic illustration of a single-link spatial inverted pendulum.

ordinate system relative to the MO system is tracked using the two rotational generalized coordinates associated with the articulation joint. It is defined by the $\mathbf{i} \cdot \mathbf{j} \cdot \mathbf{k}$ triad.

Using the above coordinate systems, the dynamics of the inverted pendulum model are derived, using the Newton-Euler formulation, in a manner completely analogous to the much simple planar presentation provided in [87].

3.1.1 Translation

Translational kinematics of the centre of mass of the inverted pendulum are considered first. The position vector of point B, expressed in the inertial coordinate system, \mathbf{r}_B^{IN} is given by:

$$\mathbf{r}_B^{IN} = \mathbf{r}_A^{IN} + \mathbf{r}_{B/A}^{IN} \quad (1)$$

$$= \mathbf{r}_A^{IN} + [T_{SHIN}] [T_{MOSH}] [T_{LOMO}] \mathbf{r}_{B/A}^{LO} \quad (2)$$

where $[T_{ij}]$ refers to the spatial rotational transformation matrix from coordinate system i to coordinate system j . Applying the product rule for differentiation and recognizing that $[T_{MOSH}]$ and $\mathbf{r}_{B/A}^{LO}$ are constant such that their subsequent time derivatives are zero, the expression for the velocity of point B may be obtained by differentiating Equation 2 resulting in:

$$\begin{aligned} \mathbf{v}_B^{IN} &= \mathbf{v}_A^{IN} + [\dot{T}_{SHIN}] [T_{MOSH}] [T_{LOMO}] \mathbf{r}_{B/A}^{LO} \\ &\quad + [T_{SHIN}] [T_{MOSH}] [\dot{T}_{LOMO}] \mathbf{r}_{B/A}^{LO} \end{aligned} \quad (3)$$

Similarly, differentiation of Equation 3 results in the equation for the acceleration of point B:

$$\begin{aligned}\mathbf{a}_B^{IN} &= \mathbf{a}_A^{IN} + [\ddot{T}_{SHIN}] [T_{MOSH}] [T_{LOMO}] \mathbf{r}_{B/A}^{LO} \\ &\quad + 2 [\dot{T}_{SHIN}] [T_{MOSH}] [\dot{T}_{LOMO}] \mathbf{r}_{B/A}^{LO} \\ &\quad + [T_{SHIN}] [T_{MOSH}] [\ddot{T}_{LOMO}] \mathbf{r}_{B/A}^{LO}\end{aligned}\quad (4)$$

It should be noted that $[\ddot{T}_{LOMO}]$ contains the second time derivatives of the generalized coordinates associated with the articulation joint ($\ddot{\theta}_i$ and $\ddot{\theta}_j$).

The translational dynamics are obtained by applying Newton's law in the inertial frame. Since interaction forces are more conveniently expressed in the model coordinate system ($\mathbf{i} \cdot \mathbf{j} \cdot \mathbf{k}$), appropriate rotational transformations are performed as follows:

$$\sum \mathbf{F}^{IN} = m \mathbf{a}^{IN} \quad (5)$$

$$\sum \mathbf{F}^{IN} = \begin{Bmatrix} F_x \\ F_y \\ F_z \end{Bmatrix}^{IN} + \begin{Bmatrix} 0 \\ 0 \\ -mg \end{Bmatrix}^{IN} + \begin{Bmatrix} F_{ext,x} \\ F_{ext,y} \\ F_{ext,z} \end{Bmatrix}^{IN} \quad (6)$$

$$= [T_{SHIN}] [T_{MOSH}] \begin{Bmatrix} F_x \\ F_y \\ F_z \end{Bmatrix}^{MO} + \begin{Bmatrix} 0 \\ 0 \\ -mg \end{Bmatrix}^{IN} + \begin{Bmatrix} F_{extx} \\ F_{exty} \\ F_{extz} \end{Bmatrix}^{IN} \quad (7)$$

where m is the pendulum segment mass and g is the acceleration due to gravity. The vector $\{ F_x \ F_y \ F_z \}^{MO^T}$ contains the three unknown interaction force components, and vector \mathbf{F}_{ext}^{IN} contains the externally-applied force acting at point C.

The general form of the rotational transformation matrix from local to global coordinates using the XYZ Euler angle convention (Bryant angles [88]) is given by:

$$[T] = \begin{bmatrix} \cos\theta_j \cos\theta_k & -\cos\theta_j \sin\theta_k & \sin\theta_j \\ \cos\theta_i \sin\theta_k + \sin\theta_i \sin\theta_j \cos\theta_k & \cos\theta_i \cos\theta_k - \sin\theta_i \sin\theta_j \sin\theta_k & -\sin\theta_i \cos\theta_j \\ \sin\theta_i \sin\theta_k - \cos\theta_i \sin\theta_j \cos\theta_k & \sin\theta_i \cos\theta_k + \cos\theta_i \sin\theta_j \sin\theta_k & \cos\theta_i \cos\theta_j \end{bmatrix} \quad (8)$$

In the case of $[T_{LOMO}]$ this transformation matrix is simplified noting that $\theta_k = 0$ such that:

$$[T_{LOMO}] = \begin{bmatrix} c\theta_j & 0 & s\theta_j \\ s\theta_i s\theta_j & c\theta_i & -s\theta_i c\theta_j \\ -c\theta_i s\theta_j & s\theta_i & c\theta_i c\theta_j \end{bmatrix} \quad (9)$$

where the letters c and s represent the cosine and sine functions respectively. To keep the derivation compact, it is beneficial to recognize that for the case of an inverted pendulum where the centre of mass lies along the axis of the segment, the relative position vector is simply:

$$\mathbf{r}_{B/A}^{LO} = \{ 0 \quad 0 \quad l_{AB} \}^T \quad (10)$$

While this simplification is convenient, computationally efficient, and reasonable in many cases, it is strictly not required. In fact, the final implementation of the model allows for general placement of the centre of mass.

Using the above key elements Equations 2 through 4 are evaluated resulting in:

$$[T_{LOMO}] \mathbf{r}_{B/A}^{LO} = l_{AB} \begin{Bmatrix} s\theta_j \\ -s\theta_i c\theta_j \\ c\theta_i c\theta_j \end{Bmatrix} = \{C\} \quad (11)$$

$$[\dot{T}_{LOMO}] \mathbf{r}_{B/A}^{LO} = l_{AB} \begin{Bmatrix} \dot{\theta}_j c\theta_j \\ -\dot{\theta}_i c\theta_i c\theta_j + \dot{\theta}_j s\theta_i s\theta_j \\ -\dot{\theta}_i s\theta_i c\theta_j - \dot{\theta}_j c\theta_i s\theta_j \end{Bmatrix} = \{D\} \quad (12)$$

and

$$[\ddot{T}_{LOMO}] \mathbf{r}_{B/A}^{LO} = l_{AB} \begin{Bmatrix} \ddot{\theta}_j c\theta_j - \dot{\theta}_j^2 s\theta_j \\ -\ddot{\theta}_i c\theta_i c\theta_j + \dot{\theta}_i^2 s\theta_i c\theta_j + \dot{\theta}_i \dot{\theta}_j c\theta_i s\theta_j \\ + \ddot{\theta}_j s\theta_i s\theta_j + \dot{\theta}_i \dot{\theta}_j c\theta_i s\theta_j + \dot{\theta}_j^2 s\theta_i c\theta_j \\ -\ddot{\theta}_i s\theta_i c\theta_j - \dot{\theta}_i^2 c\theta_i c\theta_j + \dot{\theta}_i \dot{\theta}_j s\theta_i s\theta_j \\ -\ddot{\theta}_j c\theta_i s\theta_j + \dot{\theta}_i \dot{\theta}_j s\theta_i s\theta_j - \dot{\theta}_j^2 c\theta_i c\theta_j \end{Bmatrix} \quad (13)$$

The following is obtained by rearranging Equation 13 to isolate the unknown relative angular accelerations through the articulation joint:

$$[\ddot{T}_{LOMO}] \mathbf{r}_{B/A}^{LO} = [A] \begin{Bmatrix} \ddot{\theta}_i \\ \ddot{\theta}_j \end{Bmatrix} + \{B\} \quad (14)$$

where

$$[A] = l_{AB} \begin{bmatrix} 0 & c\theta_j \\ -c\theta_i c\theta_j & s\theta_i s\theta_j \\ -s\theta_i c\theta_j & -c\theta_i s\theta_j \end{bmatrix} \quad (15)$$

and

$$\{B\} = l_{AB} \begin{Bmatrix} -\dot{\theta}_j^2 s\theta_j \\ \left(\dot{\theta}_i^2 + \dot{\theta}_j^2\right) s\theta_i c\theta_j + 2\dot{\theta}_i \dot{\theta}_j c\theta_i s\theta_j \\ -\left(\dot{\theta}_i^2 + \dot{\theta}_j^2\right) c\theta_i c\theta_j + 2\dot{\theta}_i \dot{\theta}_j s\theta_i s\theta_j \end{Bmatrix} \quad (16)$$

The above equations have defined the matrix $[A]$ and vectors $\{B\}$, $\{C\}$, and $\{D\}$ corresponding to the non-offset centre of mass configuration. As stated previously, a straightforward expansion of these allows for offset centres of mass. Developing these would simply require that the first two columns of the $[T_{LOMO}]$ transformation matrix be retained. For subsequent reference, the corresponding general expressions are labelled $[A^*]$, $\{B^*\}$, $\{C^*\}$, and $\{D^*\}$.

Using these newly defined terms, and grouping the unknowns on the left-hand side, results in the final expression of Newton's law governing translational motion of the inverted pendulum:

$$\begin{aligned} & -m [T_{SHIN}] [T_{MOSH}] [A] \begin{Bmatrix} \ddot{\theta}_i \\ \ddot{\theta}_j \end{Bmatrix} \\ & + [T_{SHIN}] [T_{MOSH}] \{F^{MO}\} \{F_{ext}^{IN}\} = m [\{a_A^{IN}\} \\ & + [\ddot{T}_{SHIN}] [T_{MOSH}] \{C\} + 2 [\dot{T}_{SHIN}] [T_{MOSH}] \{D\} \\ & + [T_{SHIN}] [T_{MOSH}] \{B\} + \{g\}] \end{aligned} \quad (17)$$

where,

$$\{F\} = \begin{Bmatrix} F_x \\ F_y \\ F_z \end{Bmatrix}^{MO} \quad (18)$$

and

$$\{g\} = \begin{Bmatrix} 0 \\ 0 \\ g \end{Bmatrix} \quad (19)$$

Matrix $[T_{SHIN}]$ is the local to global XYZ Euler angle rotational transformation matrix (of the form of Equation 8) that depends on ship orientation angles.

Matrix $[T_{MOSH}]$ is the local to global XYZ Euler angle rotational transformation matrix (of the form of Equation 8) that rotates the model frame into the ship frame by the angle β . Due to the co-planarity of the ship and model frames, and the single rotation about the z axis, the resulting transformation matrix has the simple form:

$$[T_{MOSH}] = \begin{bmatrix} c\beta & -s\beta & 0 \\ s\beta & c\beta & 0 \\ 0 & 0 & 1 \end{bmatrix} \quad (20)$$

Matrix $\left[\dot{T}_{SHIN}\right]$ has the same form as matrix $\left[\dot{T}_{LOMO}\right]$, but with entries reflecting ship motion relative to the inertial coordinate system. Similarly, matrix $\left[\ddot{T}_{SHIN}\right]$ is the second time derivative of $\left[T_{SHIN}\right]$, and has similar form to $\left[\ddot{T}_{LOMO}\right]$ (which is never actually required in its full form), but with parameters based on the ship motion. Individual entries in matrices $\left[\dot{T}_{SHIN}\right]$ and $\left[\ddot{T}_{SHIN}\right]$ are provided in Appendix A.

3.1.2 Rotation

The general dynamic moment balance equation (generalized form of Euler's equation) is used to formulate rotational equations of motion. It states:

$$\sum \mathbf{M}_B^{LO} = [I^{LO}] \{\alpha^{LO}\} + [\tilde{\omega}]^{LO} [I^{LO}] \{\omega^{LO}\} \quad (21)$$

where $[I]$ is the mass moment of inertia matrix of the articulated segment about its centre of mass, $\{\alpha\}$ is the angular acceleration vector of the segment, and $[\tilde{\omega}]^{LO}$ is a skew-symmetric matrix of the segment angular velocity defined as:

$$[\tilde{\omega}]^{LO} = \begin{bmatrix} 0 & -\omega_k & \omega_j \\ \omega_k & 0 & -\omega_i \\ -\omega_j & \omega_i & 0 \end{bmatrix} \quad (22)$$

The sum of the applied moments \mathbf{M}_B comprises the directly applied ankle moments \mathbf{M}_A , the moments caused by the interface forces at point B , and moments caused by the externally-applied force such that:

$$\mathbf{M}_A^{LO} = [T_{MOLO}] \{M^{MO}\} + [\tilde{r}_{A/B}^{LO}] [T_{MOLO}] \{F^{MO}\} + \tilde{r}_{C/B}^{LO} [T_{MOLO}] [T_{INMO}] \{F_{ext}^{IN}\} \quad (23)$$

The angular velocity of the segment, in general, recognizing that $\omega_{MO/SH}^{LO}$ is always zero, is given by:

$$\{\omega^{LO}\} = \{\omega_{SH}^{LO}\} + \{\omega_{MO/SH}^{LO}\} + \{\omega_{LO/MO}^{LO}\} \quad (24)$$

but simplifies to

$$\{\omega^{LO}\} = \{\omega_{SH}^{LO}\} + \{\omega_{LO/SH}^{LO}\} \quad (25)$$

The angular velocities in the local frame are related to the appropriate Euler angles and time derivatives of Euler angles (for both: $\{\omega_{SH}^{LO}\}$ and $\{\omega_{LO/SH}^{LO}\}$) such that

$$\begin{Bmatrix} \omega_i \\ \omega_j \\ \omega_k \end{Bmatrix} = \begin{Bmatrix} \dot{\theta}_i c\theta_j c\theta_k + \dot{\theta}_j s\theta_k \\ -\dot{\theta}_i c\theta_j s\theta_k + \dot{\theta}_j c\theta_k \\ \dot{\theta}_i s\theta_j + \dot{\theta}_k \end{Bmatrix} \quad (26)$$

Differentiating Equation 25 with respect to time results in a similar expression for the angular acceleration of the inverted pendulum expressed in the local coordinate system recognizing that $\alpha_{MO/SH}^{LO}$ is always zero:

$$\{\alpha^{LO}\} = \{\alpha_{SH}^{LO}\} + \{\alpha_{MO/SH}^{LO}\} \quad (27)$$

The expression for the angular acceleration in the local frame is obtained by directly differentiating Equation 25 with respect to time resulting in:

$$\begin{Bmatrix} \alpha_i \\ \alpha_j \\ \alpha_k \end{Bmatrix} = \begin{Bmatrix} \ddot{\theta}_i c\theta_j c\theta_k - \dot{\theta}_i \dot{\theta}_j s\theta_j c\theta_k - \dot{\theta}_i \dot{\theta}_k c\theta_j s\theta_k \\ \quad + \ddot{\theta}_j s\theta_k + \dot{\theta}_j \dot{\theta}_k c\theta_k \\ -\ddot{\theta}_i c\theta_j s\theta_k + \dot{\theta}_i \dot{\theta}_j s\theta_j s\theta_k + \dot{\theta}_i \dot{\theta}_k c\theta_j \\ \quad c\theta_k + \ddot{\theta}_j c\theta_k - \dot{\theta}_j s\theta_k \\ \ddot{\theta}_i s\theta_j + \dot{\theta}_i \dot{\theta}_j c\theta_j + \ddot{\theta}_k \end{Bmatrix} \quad (28)$$

Separating out the unknown second time derivatives of the Euler angles and noting that $\ddot{\theta}_k = \dot{\theta}_k = 0$ allows the angular acceleration of the local frame relative to the ship frame to be expressed compactly as:

$$\{\alpha_{LO/SH}^{LO}\} = [E] \begin{Bmatrix} \ddot{\theta}_i \\ \ddot{\theta}_j \end{Bmatrix} + \{G\} \quad (29)$$

where

$$[G] = \begin{Bmatrix} \dot{\theta}_i \dot{\theta}_j s\theta_j \\ 0 \\ \dot{\theta}_i \dot{\theta}_j c\theta_j \end{Bmatrix} \quad (30)$$

Reinserting this into Equation 28 results in:

$$\{\alpha^{LO}\} = \{\alpha_{SH}^{LO}\} + [E] \begin{Bmatrix} \ddot{\theta}_i \\ \ddot{\theta}_j \end{Bmatrix} + \{G\} \quad (31)$$

Combining terms results in the complete general moment balance equation:

$$\begin{aligned} & [T_{MOLO}] \{M^{MO}\} + [\tilde{r}_{A/B}^{LO}] [T_{MOLO}] \{F^{MO}\} + [\tilde{r}_{C/B}] [T_{MOLO}] [T_{INMO}] \{F_{ext}^{IN}\} \\ & = [I^{LO}] \{\alpha_{SH}^{LO}\} + [I^{LO}] [E] \begin{Bmatrix} \ddot{\theta}_i \\ \ddot{\theta}_j \end{Bmatrix} \\ & + [I^{LO}] \{G\} + [\tilde{\omega}^{LO}] [I^{LO}] \{\omega^{LO}\} \end{aligned} \quad (32)$$

Recognizing that the first term on the left-hand side can be partitioned such that:

$$[T_{MOLO}] \{M^{MO}\} = [H] \left\{ \begin{matrix} M_x \\ M_y \end{matrix} \right\}^{MO} + [L] \{M_z^{MO}\} \quad (33)$$

allows the complete set of angular equations of motion to be written as:

$$\begin{aligned} & [L] \{M_z^{MO}\} + [\tilde{r}_{A/B}^{LO}] [T_{MOLO}] \{F^{MO}\} \\ & - [I^{LO}] [E] \left\{ \begin{matrix} \ddot{\theta}_i \\ \ddot{\theta}_j \end{matrix} \right\}^{MO} = [I^{LO}] [T_{MOLO}] [T_{SHMO}] \{\alpha_{SH}^{SH}\} \\ & + [I^{LO}] \{G\} + [\tilde{\omega}^{LO}] [I^{LO}] \{\omega^{LO}\} - [H] \left\{ \begin{matrix} M_x \\ M_y \end{matrix} \right\}^{MO} \\ & - [\tilde{r}_{C/B}] [T_{MOLO}] [T_{INMO}] \{F_{ext}^{IN}\} \end{aligned} \quad (34)$$

3.1.3 Combined Dynamic Equations

The translational and rotational equations are now combined into the final set of six equations that govern the motion of the three-dimensional single-segment shipboard inverted pendulum:

$$\begin{aligned} & \begin{bmatrix} -m [T_{SHIN}] [T_{MOSH}] [A] & - [I^{LO}] [E] \\ [T_{SHIN}] [T_{MOSH}] & [\tilde{r}_{A/B}^{LO}] [T_{MOLO}] \\ 0 & [L] \end{bmatrix}^T \begin{Bmatrix} \ddot{\theta}_i \\ \ddot{\theta}_j \\ F_x \\ F_y \\ F_z \\ M_z \end{Bmatrix} \\ & = \left\{ \begin{aligned} & m \left[\{a_A^{IN}\} + [\ddot{T}_{SHIN}] [T_{MOSH}] \{C\} \right. \\ & + 2 [\dot{T}_{SHIN}] [T_{MOSH}] \{D\} + [T_{SHIN}] [T_{MOSH}] \{B\} \\ & \left. + \{g\} \right] \\ & [I^{LO}] [T_{MOLO}] [T_{SHMO}] \{\alpha_{SH}^{SH}\} + [I^{LO}] \{G\} \\ & + [\tilde{\omega}^{LO}] [I^{LO}] \{\omega^{LO}\} - [H] \left\{ \begin{matrix} M_x \\ M_y \end{matrix} \right\}^{MO} - [\tilde{r}_{C/B}^{LO}] \{F_{ext}^{LO}\} \end{aligned} \right\} \end{aligned} \quad (35)$$

Solving this matrix equation results in the four unknown components of the interface force, and the moment. The relative angular accelerations of the articulated segment can be successively numerically integrated to track the segment orientation. The interface moment components, M_x and M_y , are prescribed by the ankle moment controller (described subsequently).

3.1.4 Ankle Moments

Ankle moments are prescribed by, in general, a combination of passive and active inputs to restore the articulated segment from perturbations that have arisen from ship motion or other external sources. The applied ankle moment, \mathbf{M}_A , acts about the x and y axes in the model frame (MO) such that:

$$\mathbf{M}_A = \begin{Bmatrix} M_{Ax} \\ M_{Ay} \end{Bmatrix} \quad (36)$$

where M_{Ax} and M_{Ay} are comprised of passive stiffness ($T_{stiffness}$), passive damping ($T_{damping}$), and actively-controlled contributions ($T_{control}$) such that:

$$M_{Ax,y} = -(T_{x,y\ stiffness} + T_{x,y\ damping} + T_{x,y\ control}) \quad (37)$$

where

$$T_{x\ stiffness} = k_{\tau x} \theta_{rel\ x} \quad (38)$$

$$T_{x\ damping} = c_{\tau x} \dot{\theta}_{rel\ x} \quad (39)$$

$$T_{x\ control} = A_{k\ x} \theta_{tot\ x} + A_{c\ x} \dot{\theta}_{tot\ x} \quad (40)$$

$$T_{y\ stiffness} = k_{\tau y} \theta_{rel\ y} \quad (41)$$

$$T_{y\ damping} = c_{\tau y} \dot{\theta}_{rel\ y} \quad (42)$$

$$T_{y\ control} = A_{k\ y} \theta_{tot\ y} + A_{c\ y} \dot{\theta}_{tot\ y} \quad (43)$$

The coefficients k_i , c_i , and A_i can be scheduled as appropriate depending on the state of the articulation to reproduce the desired responses.

The independent relative angles $\theta_{rel\ x,y}$ and angular velocities $\dot{\theta}_{rel\ x,y}$ are measured relative to the ship deck, taking applicable transformations into account. The total angles and angular rates $\theta_{tot\ x,y}$ and $\dot{\theta}_{tot\ x,y}$ are measured relative to the absolute vertical reference in the inertial frame (IN).

Joint range and torque limits are also applied to bound joint kinematics and actuation to realistic values and ensure that MII events related to these physical limits are not ignored.

3.1.5 Implementation

The articulated postural stability model has been implemented in the executable computer program PSM3D. Effectively, PSM3D implements the generalized form of Equation 35 (to include capability for offset centres of mass) to solve for the second time derivatives of the Euler angles defining the orientation of the articulated segment relative to the ship deck as well as the four unknown interface force and moment components. Using suitable initial conditions for the relative orientation and rate of rotation of the articulated segment relative to the deck, and using the evaluated second time derivatives of the Euler angles, the transient-dynamic solution is propagated forward in time using a numerical integration scheme. At each time step, the four MII parameters defined by Equations 56 through 59 are evaluated.

The file structure associated with the core PSM3D program (PSM3D.exe) is illustrated in Figure 12. PSM3D requires two input files. The first, PSM3D.inp, contains information describing the run, parameters of the dynamic model, and numerical integration parameters including initial conditions. A sample PSM3D.inp file is provided in Appendix C Figure C.2. The second input file, labelled motion.inp, in Figure 12, contains motion of the ship deck at the model interface location comprising the position and orientation of the ship deck as well as first and second derivatives as a function of time. Input deck motion is interpolated by PSM3D such that the numerical integration time step is not tied to the sampling frequency of the prescribed deck motion. PSM3D optionally generates screen output and an output file called PSM3D.out containing tabulated data comprising the model state, all components of the interface force and moment, and the four derived MII parameters as a function of time. Additional optional output files specific to various forms of analysis are anticipated as the development of PSM3D continues.

A suite of related pre- and post-processing programs has also been developed for filtering data, facilitating model tuning, determining MII rates, and animating results.

3.2 Three-dimensional Graham Model

The original planar Graham formulation used the conceptual model of a block positioned on the deck of a ship. The corresponding three-dimensional model uses the same basic conceptual design. The three-dimensional block, with height h , length l , and width w , is placed in a virtual motion environment. The model is then solved for the interface forces at the attachment point to the deck. A schematic representation of the model is shown in Figure 13.

The diagram also shows the coordinate systems used in its derivation. These coordinate systems are similar to those found in the Langlois inverted pendulum derivation

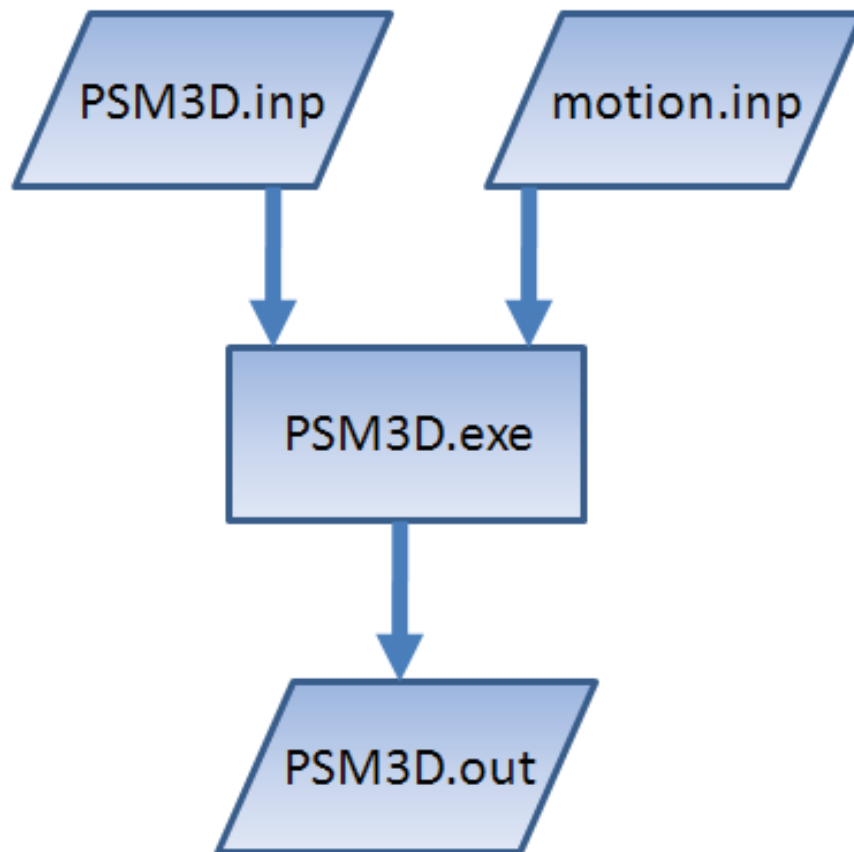


Figure 12: Schematic illustration of PSM3D file structure.

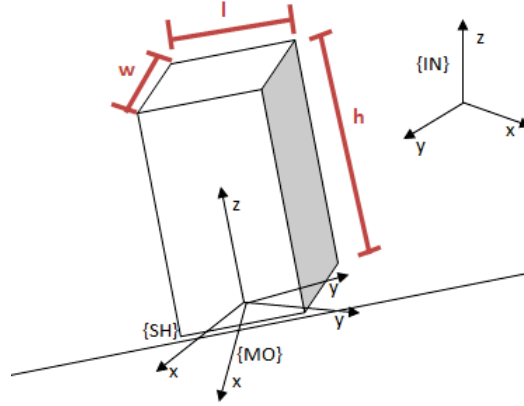


Figure 13: Coordinate systems used in the derivation of three-dimensional Graham shipboard postural stability model.

(Section 3.1 and [68]). The inertial frame (designated IN) is defined outside of the motion environment. The ship coordinate system (designated SH) is attached to the ship at the point of attachment of the Graham model and is aligned with the inertial frame in the absence of ship motion. Finally, a model coordinate system (designated MO) is attached to the block and located at the interface between the block and the ship deck.

3.2.1 Kinematics

Defining the point of attachment of the model to the motion environment as point a , the position of the centre of gravity of the block (designated cg) can be written as:

$$\mathbf{r}_{CG}^{IN} = \mathbf{r}_A^{IN} + \mathbf{r}_{CG/A}^{IN} \quad (44)$$

where the superscript is the coordinate system in which the vector is defined and the subscript indicates the point(s) to which the vector applies. Defining two rotational transformation matrices from the inertial coordinate system to the ship frame, and then from the ship frame to the model frame, the equation can be written as:

$$\mathbf{r}_{CG}^{IN} = \mathbf{r}_A^{IN} + [T_{SHIN}] [T_{MOSH}] \mathbf{r}_{CG/A}^{MO} \quad (45)$$

where for a rotation matrix R the subscript denotes the coordinate system rotated from and the superscript denotes the coordinate system rotated to. The rotation matrix from the inertial to ship frame is computed using the Euler angles which depend on the ship state at a given time step. The rotation matrix from the ship to

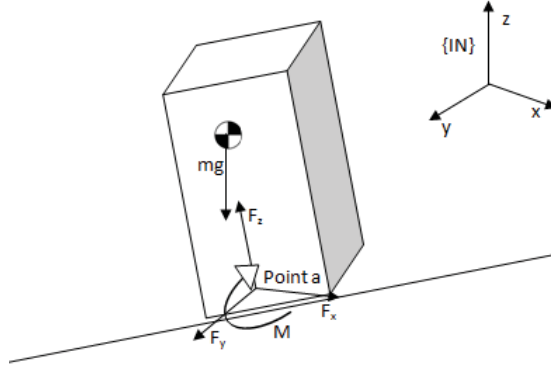


Figure 14: Forces acting on the three-dimensional Graham model.

model frame is defined as a single rotation about the z axis in the ship frame:

$$\mathbf{T}_{MOSH} = \begin{bmatrix} \cos \beta & -\sin \beta & 0 \\ \sin \beta & \cos \beta & 0 \\ 0 & 0 & 1 \end{bmatrix} \quad (46)$$

where β is the constant angle between the ship and model frames.

Taking the derivative of the position vector, noting that the angle between the model and ship frames is constant, and that the height of the centre of gravity above point A in the model frame is constant, the velocity of the centre of gravity in the inertial frame can be written as:

$$\mathbf{v}_{CG}^{IN} = \mathbf{v}_A^{IN} + \left[\dot{T}_{SHIN} \right] [\mathbf{T}_{MOSH}] \mathbf{r}_{CG/A}^{MO} \quad (47)$$

Taking the time derivative of the velocity expression results in the acceleration expression:

$$\mathbf{a}_{CG}^{IN} = \mathbf{a}_A^{IN} + \left[\ddot{T}_{SHIN} \right] [\mathbf{T}_{MOSH}] \mathbf{r}_{CG/A}^{MO} \quad (48)$$

Now that the acceleration of the body is known, the dynamic equations can be developed and solved in order to find the interface forces and moments at the attachment point a .

3.2.2 Dynamics

The block model does not have any directly-applied external disturbance forces acting on it, and therefore the only forces acting on the body are the gravitational forces, inertial forces from the motion of the body, and reaction forces at the attachment point. If the attachment point is assumed to be a rigid singular point of attachment,

the reaction forces and moments will be acting at that point. Figure 14 provides a diagram of the forces acting on the body.

Newton's law relates the forces acting on the block in the inertial frame to the acceleration of the centre of mass of the block such that:

$$\sum \mathbf{F}^{IN} = m\mathbf{a}_{CG}^{IN} \quad (49)$$

where m is the mass of the block. An expression of the acceleration of the centre of gravity was determined from the kinematic derivation and given in Equation 48. The applied forces, comprising the gravitational and reaction forces at the attachment point, are:

$$\sum \mathbf{F}^{IN} = \begin{Bmatrix} 0 \\ 0 \\ -mg \end{Bmatrix}^{IN} + \begin{Bmatrix} F_x \\ F_y \\ F_z \end{Bmatrix}^{IN} \quad (50)$$

where g is the gravitational constant and F_x , F_y , and F_z are the components of the reaction force. It is convenient for subsequent sliding and tipping index evaluation for the reaction forces to be expressed in the model frame; so the force summation then becomes:

$$\sum \mathbf{F}^{IN} = \begin{Bmatrix} 0 \\ 0 \\ -mg \end{Bmatrix}^{IN} + [T_{SHIN}] [T_{MOSH}] \begin{Bmatrix} F_x \\ F_y \\ F_z \end{Bmatrix}^{MO} + [T_{MOLO}] [T_{INMO}] \{F_{ext}^{IN}\} \quad (51)$$

Substituting Equations 48 and 51 into Equation 49, and rearranging the resulting equation such that the unknowns are on the left-hand side, the translational dynamic equation then becomes:

$$\begin{aligned} [T_{SHIN}] [T_{MOSH}] \begin{Bmatrix} F_x \\ F_y \\ F_z \end{Bmatrix}^{MO} &= \begin{Bmatrix} 0 \\ 0 \\ mg \end{Bmatrix}^{IN} - [T_{MOLO}] [T_{INMO}] \{F_{ext}^{IN}\} \\ &+ \mathbf{a}_A^{IN} + atb\ddot{T}_{SHIN} [T_{MOSH}] \mathbf{r}_{CG/A}^{MO} \end{aligned} \quad (52)$$

where all the variables on the right-hand side are known from the ship motion and the position of the block on the ship deck.

The generalized Euler equation for moments about the centre of gravity in the inertial frame is:

$$\sum \mathbf{M}_{CG}^{MO} = I_{CG} \boldsymbol{\alpha} + \boldsymbol{\omega} \times [I_{CG}] \boldsymbol{\omega} \quad (53)$$

where $\boldsymbol{\alpha}$ is the angular acceleration of the block, $\boldsymbol{\omega}$ is the angular velocity of the block, and I_{cg} is the mass moment of inertia of the block. Since the block is not moving

relative to the ship deck, the angular velocity and acceleration are those of the ship which are considered to be known functions of time. In practice, the ship motion may be obtained from sea trial or model test data, or alternatively simulated.

The moments acting on the block are the reaction moments at the attachment point, the moments caused by the deck reaction forces about the centre of gravity, and the moments caused by the externally-applied force about the centre of gravity. Moments about the centre of gravity are expressed as:

$$\sum \mathbf{M}_{CG}^{MO} = \begin{Bmatrix} M_x \\ M_y \\ M_z \end{Bmatrix}^{MO} + \mathbf{r}_{A/CG}^{MO} \times \begin{Bmatrix} F_x \\ F_y \\ F_z \end{Bmatrix}^{MO} + \mathbf{r}_{C/CG}^{MO} \times \{F_{ext}^{MO}\} \quad (54)$$

where M_x , M_y , and M_z are the reaction moments at the attachment point. Equation 54 is substituted into Equation 53, and the resulting equation is rearranged to isolate the reaction moments:

$$\begin{Bmatrix} M_x \\ M_y \\ M_z \end{Bmatrix}^{MO} = I_{CG}\boldsymbol{\alpha} + \boldsymbol{\omega} \times [I_{CG}]\boldsymbol{\omega} - \mathbf{r}_{A/CG}^{MO} \times \begin{Bmatrix} F_x \\ F_y \\ F_z \end{Bmatrix}^{MO} - \mathbf{r}_{C/CG}^{MO} \times \{F_{ext}^{MO}\} \quad (55)$$

To obtain the reaction forces and moments, Equation 52 is first solved for the reaction forces; then Equation 55 is solved for the reaction moments.

3.2.3 Implementation

The three-dimensional Graham model has been implemented and compiled into an executable program called GRM3D. The implementation is similar to the implementation of the inverted pendulum model, PSM3D [68]. This was chosen so that the simulation environments of the two models would be similar and analysis of the results would be simpler due to the consistency of the format. The executable solves the dynamics equations (Equations 52 and 55). After solving for the forces and moments, the postural stability indices are then calculated using Equations 56, 57, 58, and 59 or, alternatively, using the approach presented in Section 3.4.2.

The file structure is also similar to that of PSM3D. There are two input files required for a simulation run. One input file provides the motion data in six degrees of freedom as well as the corresponding first and second time derivatives. The second input file provides the model constants, including the geometrical and inertial properties. The simulation results are output to a file with the reaction forces and moments in all three directions as well as the four MII indices as functions of time.

3.3 Computational Validation

The formulation of the GRM3D postural stability model can be thought of as a special case of the more general articulated inverted pendulum postural stability model with all articulation degrees of freedom constrained. Therefore, comparing GRM3D with a model such as PSM3D with its two articulation joints locked provides a computational means of partially validating GRM3D. The PSM3D model has been previously validated [68]. To avoid reformulating the PSM3D model, the final set of governing dynamic equations, that conventionally are solved to obtain the three components of the interface force (F_x , F_y , and F_z), the interface moment (M_z), and the relative angular accelerations about each of the two orthogonal axes forming the articulation joint ($\ddot{\theta}_x$ and $\ddot{\theta}_y$), were reformulated for the constrained case by moving the now known $\ddot{\theta}_x$ and $\ddot{\theta}_y$ to the right hand side of the equation and relocating the previously known ankle moments (M_x and M_y) to the left hand side. With the articulation locked, θ_x and θ_y , as well as their time derivatives are always zero. As a result, with the reformulation of the final equations, the PSM3D model could be used to solve for the six force and moment components evaluated by the GRM3D model. Further, in making this change, the PSM3D model no longer required numerical integration but rather, in principle, became a simple function evaluation. Numerical integration of the model was retained to minimize the extent of recoding the PSM3D model required to include the option for locking the articulation joint.

For the computational validation, simulation conditions were set up using the physical parameters listed in Table 1 corresponding to those originally proposed by Graham [74], and typical ship motion representative of a frigate operating on an oblique heading, at moderate speed, in sea state four conditions [89]. Using the same initial conditions, both the GRM3D and PSM3D models were run for a 60 second duration. The simulation results for each force component direction obtained from both models are presented in Figures 15 through 20. As can be seen from the simulation results, relatively close agreement is found between the full dynamic solution provided by PSM3D and the quasi-static solution obtained from GRM3D. Of interest is the fact that identical results are obtained for the yaw moment (M_z). Differences between the models are currently attributed to the method used for constraining the articulation joint in the PSM3D model.

Table 1: Simulation parameters used with GRM3D and PSM3D.

Parameter	Value
m	78 kg
I_{xx}	47.2 kg m ²
I_{yy}	47.2 kg m ²
I_{zz}	1 kg m ²
$\mathbf{r}_{CG/A}^{MO}$	$\{0.0 \ 0.0 \ 0.9\}^T$ m
g	9.81 m/sec ²

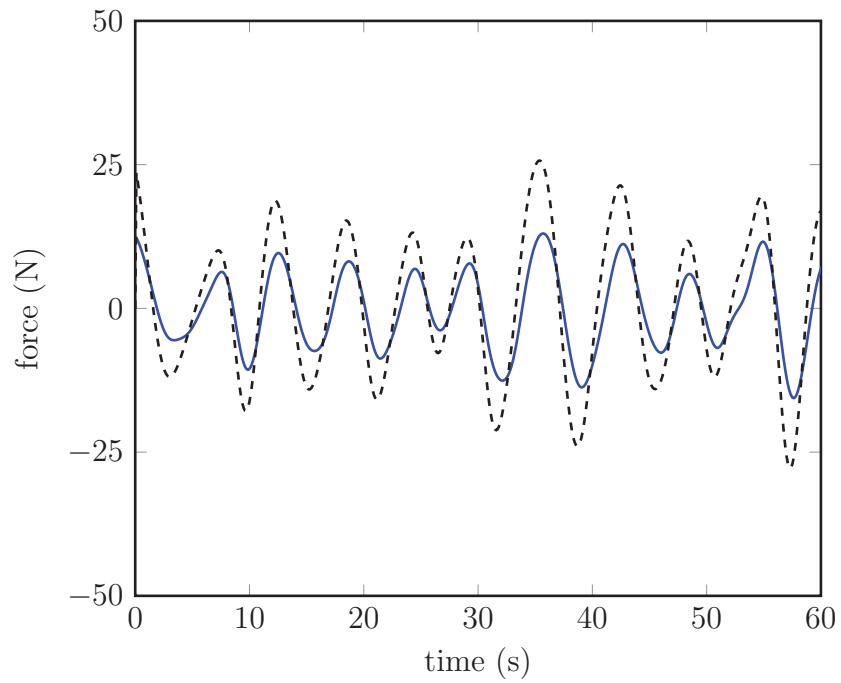


Figure 15: Longitudinal force (F_x) for typical ship motion computed using GRM3D (dashed) and PSM3D (solid).

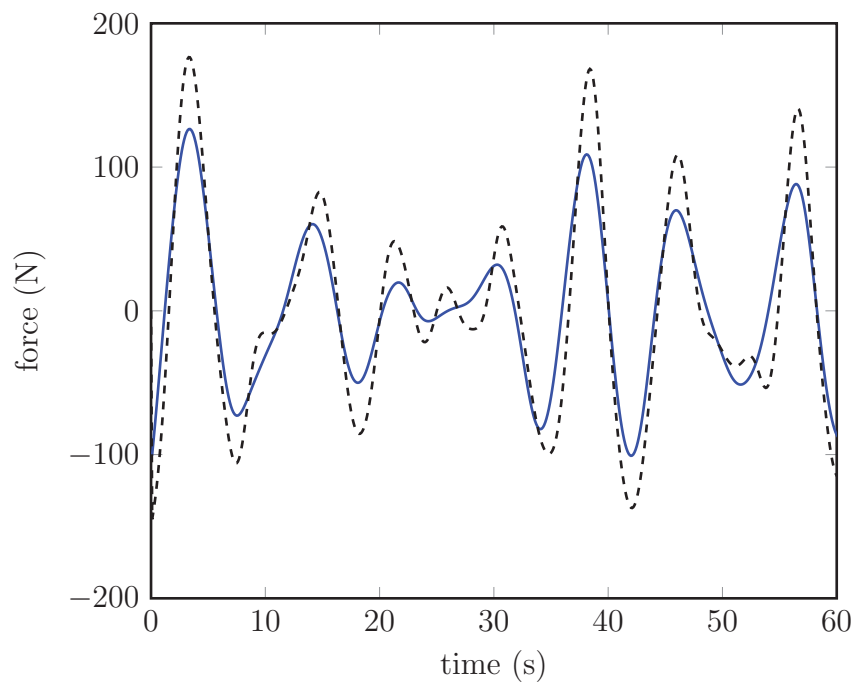


Figure 16: Lateral force (F_y) for typical ship motion computed using GRM3D (dashed) and PSM3D (solid).

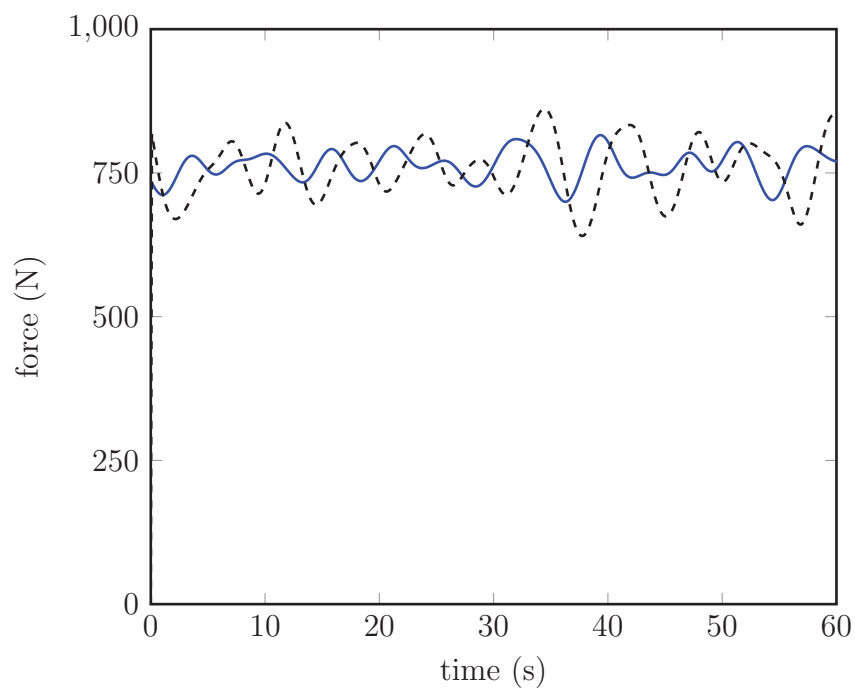


Figure 17: Vertical force (F_z) for typical ship motion computed using GRM3D (dashed) and PSM3D (solid).

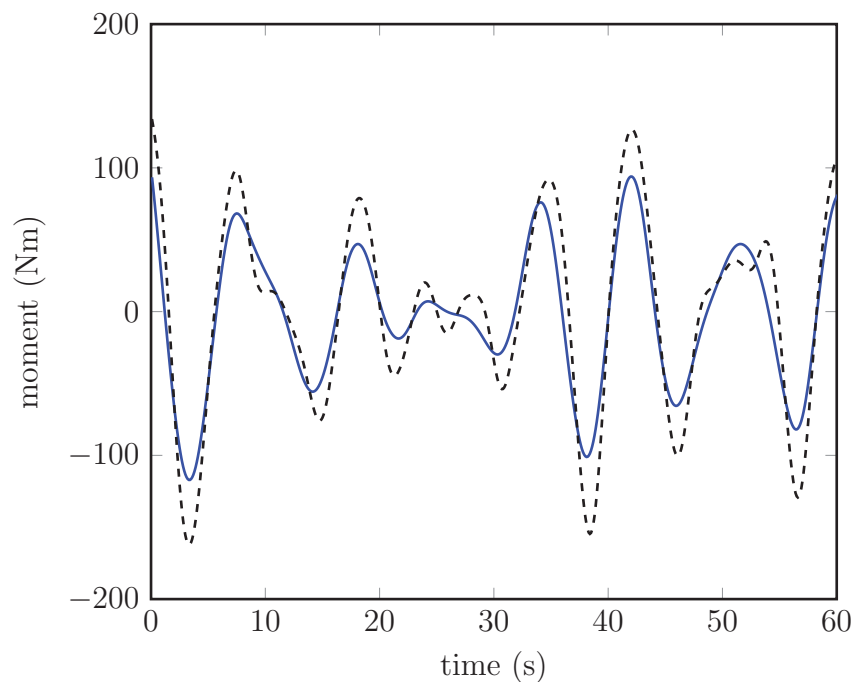


Figure 18: Longitudinal moment (M_x) for typical ship motion computed using GRAM3D (dashed) and PSM3D (solid).

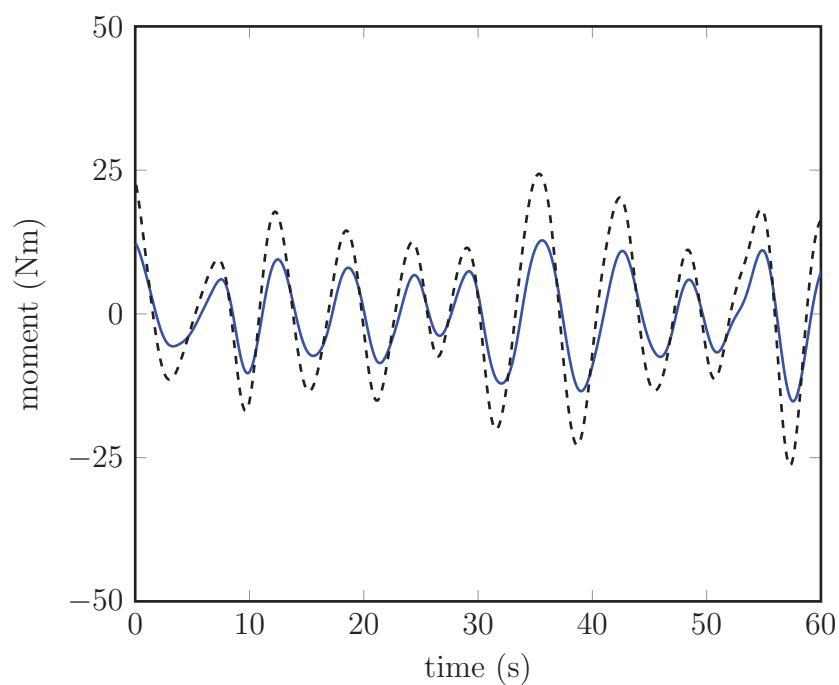


Figure 19: Lateral moment (M_y) for typical ship motion computed using GRAM3D (dashed) and PSM3D (solid).

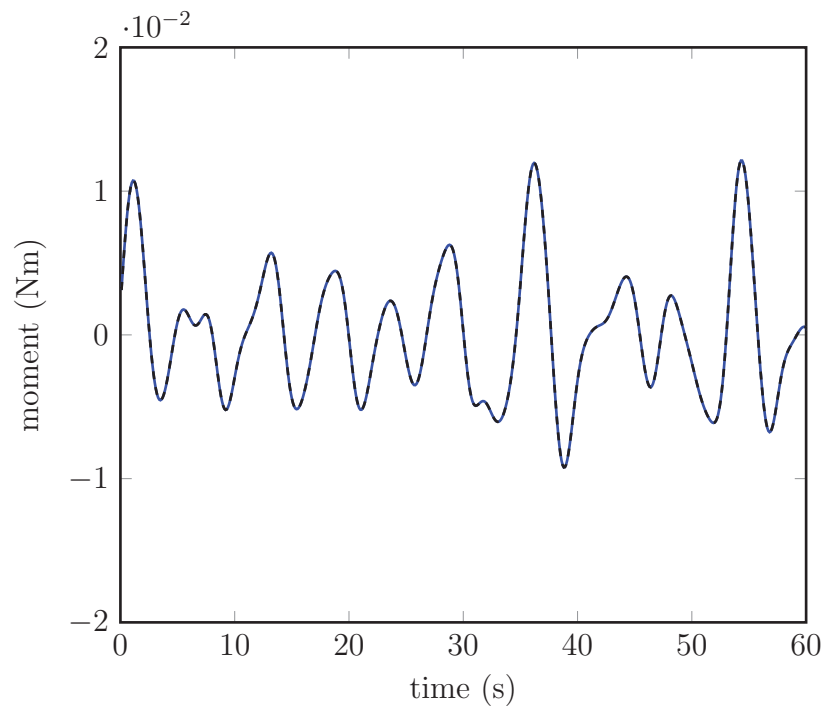


Figure 20: Vertical moment (M_z) for typical ship motion computed using GRM3D (dashed) and PSM3D (solid).

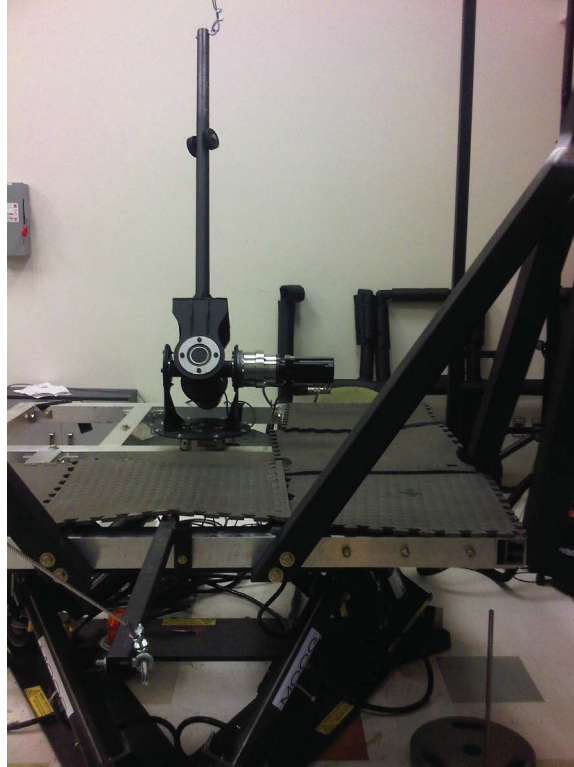


Figure 21: *Experimental apparatus.*

3.3.1 Experimental Validation

Experimental validation of the GRM3D model was accomplished using the apparatus shown in Figure 21. It consists of a Moog 6DOF2000E electric Stewart platform motion base onto which a purpose-built inverted pendulum was mounted. Similar to the PSM3D model, the inverted pendulum is capable of two degrees of articulation near its base with coincident rotational axes. However, it is also possible to effectively lock the articulation either passively with a mechanical locking brace across the articulation joint or actively with appropriate commands to the high-update-rate articulation controller. Both approaches have been confirmed to produce the same results. Instrumentation consists of an ATI model Theta six-axis load cell mounted at the interface between the inverted pendulum and the motion base. The parameters representing the as-built inverted pendulum (without optional mass plates) are provided in Table 2.

To obtain the validation results, the motion base was commanded to reproduce the translational and rotational motion profiles plotted in Figures 22 and 23, respectively. These motions, as with the computational validation case, are representative of typical frigate motions, but have been scaled so as not to exceed the kinematic capabilities of the motion base. The scaling involved significant attenuation of translational motions

and minor attenuation of angular motions. Motion washout was purposefully not used.

The experiment was run for 20 seconds of simulated ship motion. The total time of 20 seconds included a linear motion ramp-up period (0 through 2 seconds) that is not shown in the presented force and moment plots followed by 18 seconds (2 through 20 seconds) of dynamic response data. Load cell results were low-pass filtered using a two-pass fourth-order Butterworth filter having a cut-off frequency of 0.5 Hz. Following the experimental run, the GRM3D simulation model was run for the same conditions. Results comparing the measured and simulated interface force data for each of the six force and moment components are presented in Figures 24 through 29. The measured and simulated results closely agree for F_x , F_y , F_z , and M_x . The shapes of the force profiles agree less well for M_y and M_z but it is recognized that the magnitudes of the moments are very small in these component directions such that measurement error may be a significant factor.

As a demonstration of the utility of sliding and tipping indices, the simulation results were used to evaluate the sliding index (left-hand side of Equation 56) and the tipping index about the x axis (left-hand side of Equation 57). The results are plotted in Figure 30. Since in all cases the sliding and tipping indices are below typical values of deck coefficient of friction and stance width, respectively, motion induced interruptions (MIIs) are not indicated for the motion profile used for experimental validation of the three-dimensional Graham model.

3.4 MII Detection

3.4.1 Standard Indices

Four parameters are defined for use in identifying MII events corresponding to the four theoretically-possible modes of MII onset associated with the inverted pendulum/ship deck model: sliding, tipping in the frontal plane, tipping in the sagittal plane, and

Table 2: *Simulation parameters used with GRM3D and PSM3D.*

Parameter	Value
m	62.58 kg
I_{xx}	$1.93 \times 10^3 \text{ kg m}^2$
I_{yy}	$1.91 \times 10^3 \text{ kg m}^2$
I_{zz}	$6.87 \times 10^2 \text{ kg m}^2$
$\mathbf{r}_{CG/A}^{MO}$	$\{0.058 \quad -0.048 \quad 0.338\}^T \text{ m}$
g	9.81 m/sec^2

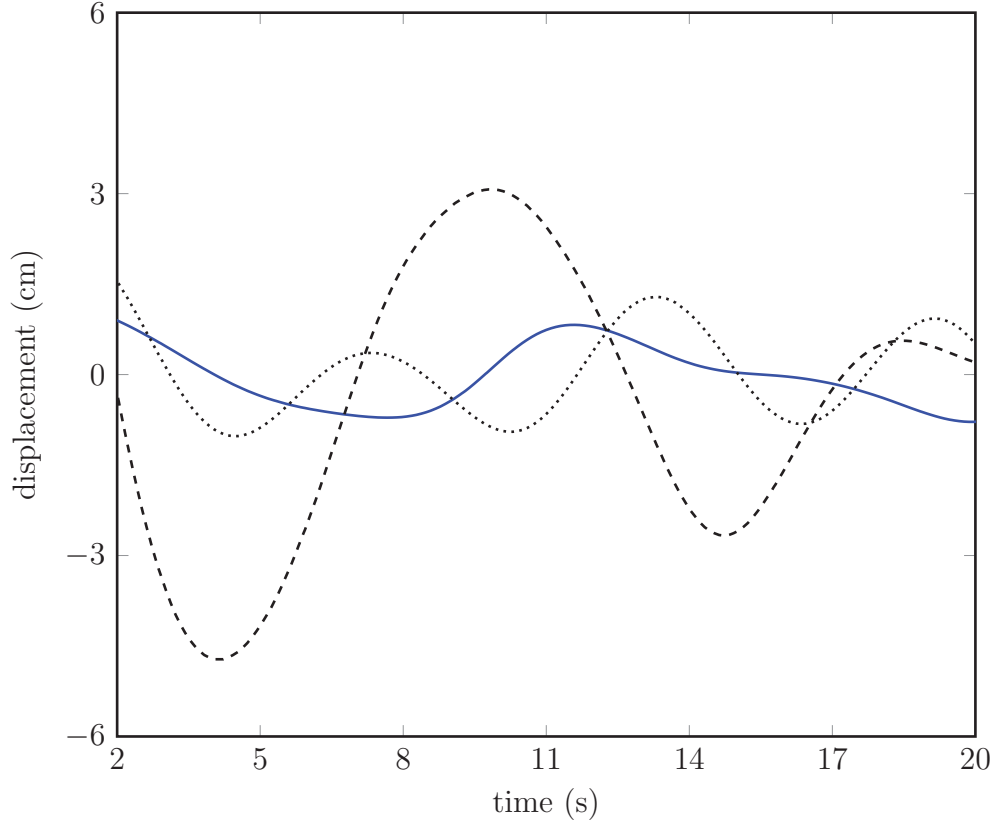


Figure 22: Representative surge (solid), sway (dashed), and heave (dotted) ship motions scaled to remain within motion platform workspace.

yawing. It is recognized that yaw instability is not likely in shipboard applications; but it is retained for completeness. These parameters are defined in a general form such that they quantify the severity of the respective conditions without presupposing particular threshold values.

In the case of sliding, the relevant parameter, called the sliding index (P_{slide}) is given by:

$$P_{slide} = \frac{\sqrt{F_x^2 + F_y^2}}{|F_z|} \quad (56)$$

Sliding is expected when the value of P_{slide} exceeds the prevailing coefficient of friction μ at the interface between the inverted pendulum and the deck.

In the case of tipping in the frontal plane, the relevant parameter, called the frontal plane tipping index ($P_{frontal\ tip}$) is given by:

$$P_{frontal\ tip} = \frac{|M_x|}{|F_z|} \quad (57)$$

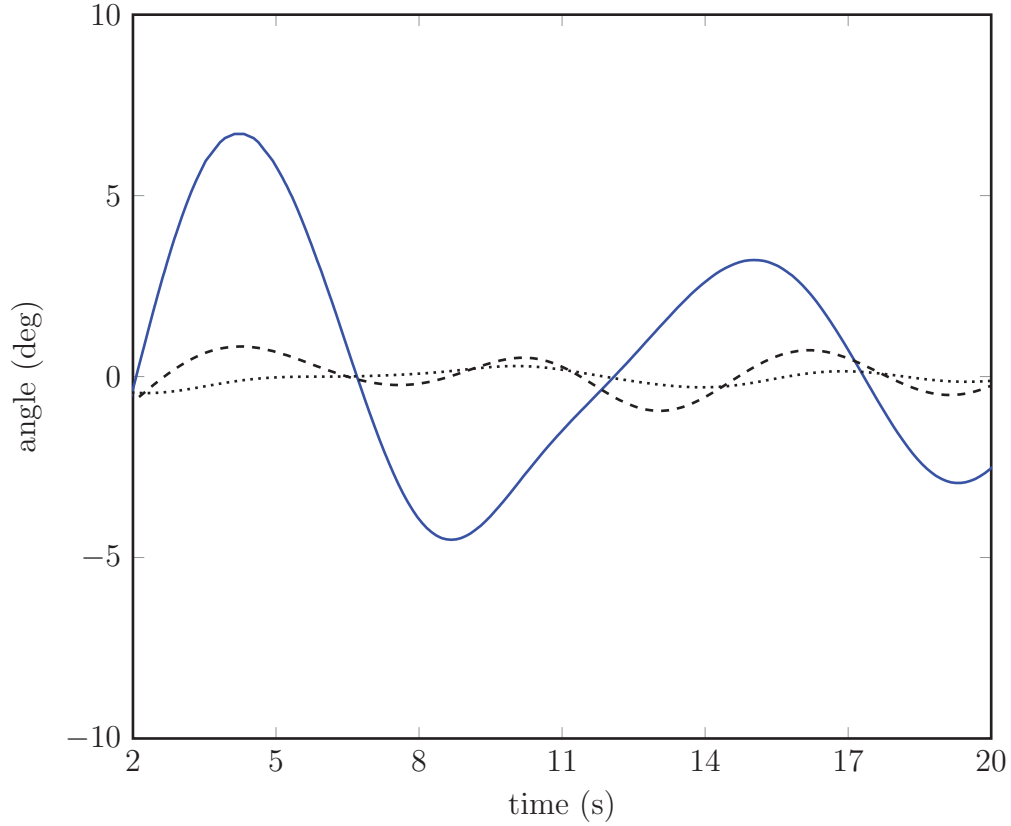


Figure 23: Representative roll (solid), pitch (dashed), and yaw (dotted) ship motions scaled to remain within motion platform workspace.

Tipping is expected when the value of $P_{frontal\ tip}$ exceeds a threshold related to the effective stance width.

In the case of tipping in the sagittal plane, the relevant parameter, called the sagittal plane tipping index ($P_{sagittal\ tip}$) is given by:

$$P_{sagittal\ tip} = \frac{|M_y|}{|F_z|} \quad (58)$$

Tipping is expected when the value of $P_{sagittal\ tip}$ exceeds a threshold related to the effective stance length.

In the case of yawing, the relevant parameter, called the yawing index (P_{yaw}) is given by:

$$P_{yaw} = \frac{|M_z|}{|F_z|} \quad (59)$$

Yawing is expected when the value of P_{yaw} exceeds a threshold corresponding to the effective stance diameter.

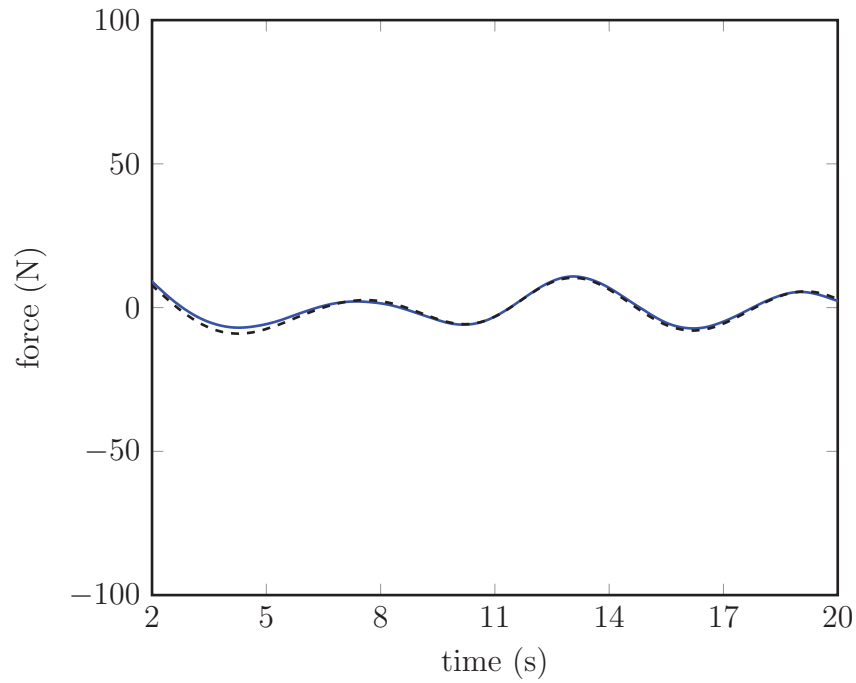


Figure 24: Longitudinal force (F_x) for typical ship motion measured experimentally (solid) and simulated using GRM3D (dashed).

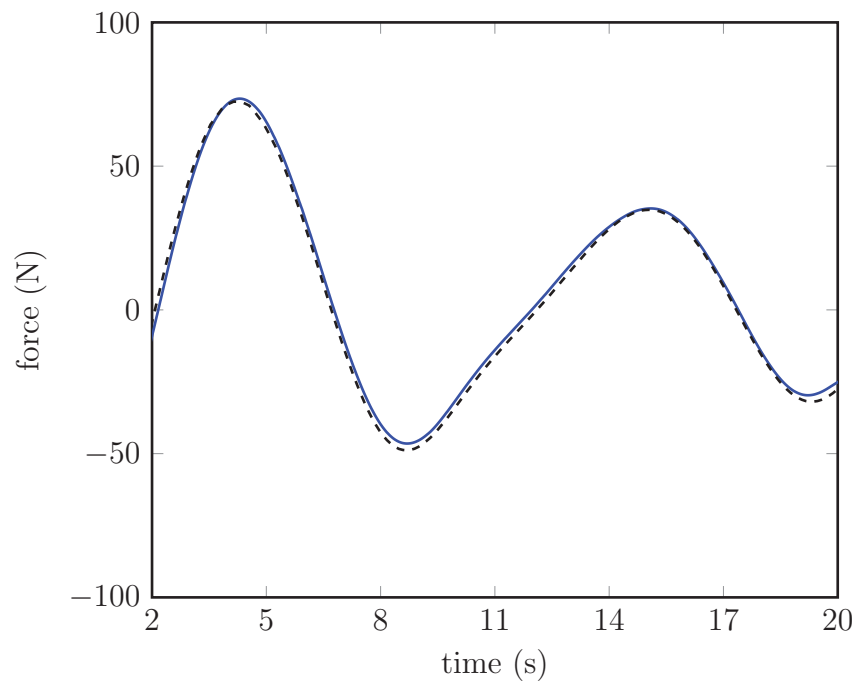


Figure 25: Lateral force (F_y) for typical ship motion measured experimentally (solid) and simulated using GRM3D (dashed).

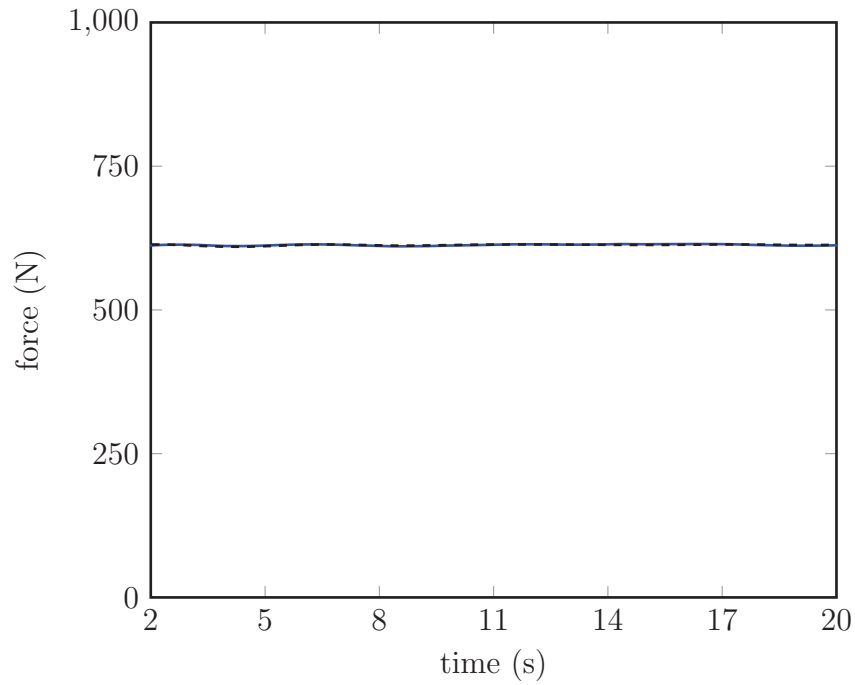


Figure 26: Vertical force (F_z) for typical ship motion measured experimentally (solid) and simulated using GRM3D (dashed).

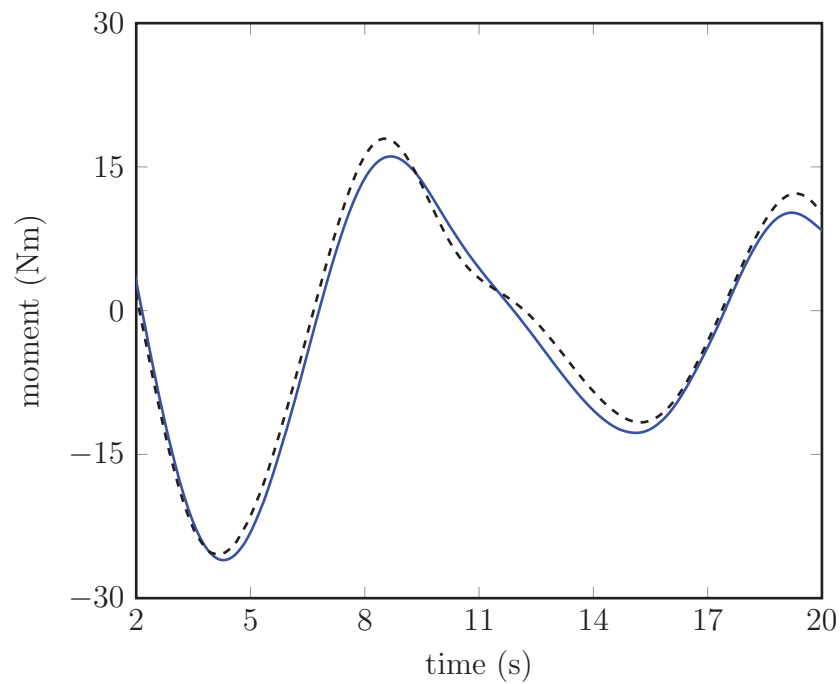


Figure 27: Longitudinal moment (M_x) for typical ship motion measured experimentally (solid) and simulated using GRM3D (dashed).

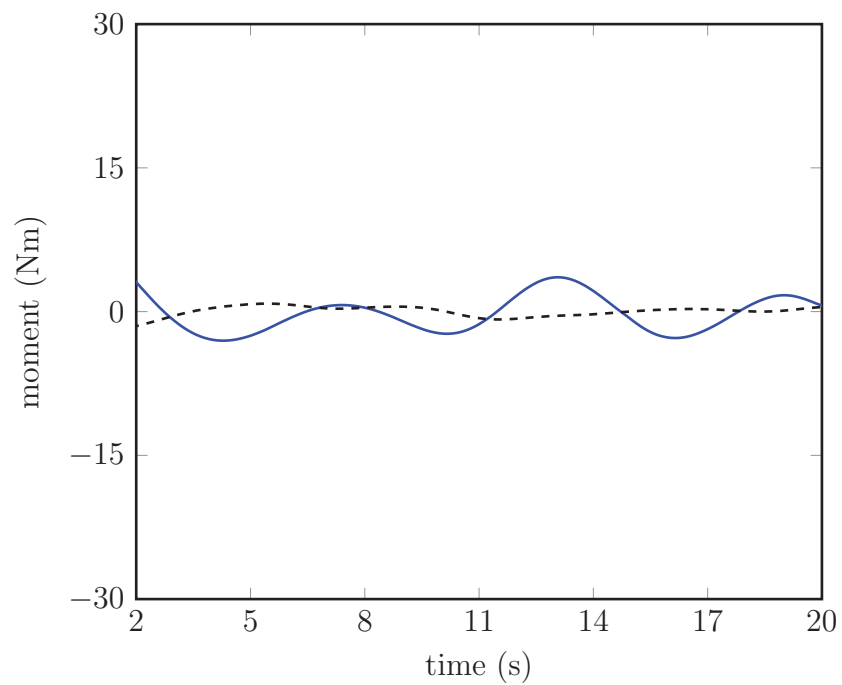


Figure 28: Lateral moment (M_y) for typical ship motion measured experimentally (solid) and simulated using GRM3D (dashed).

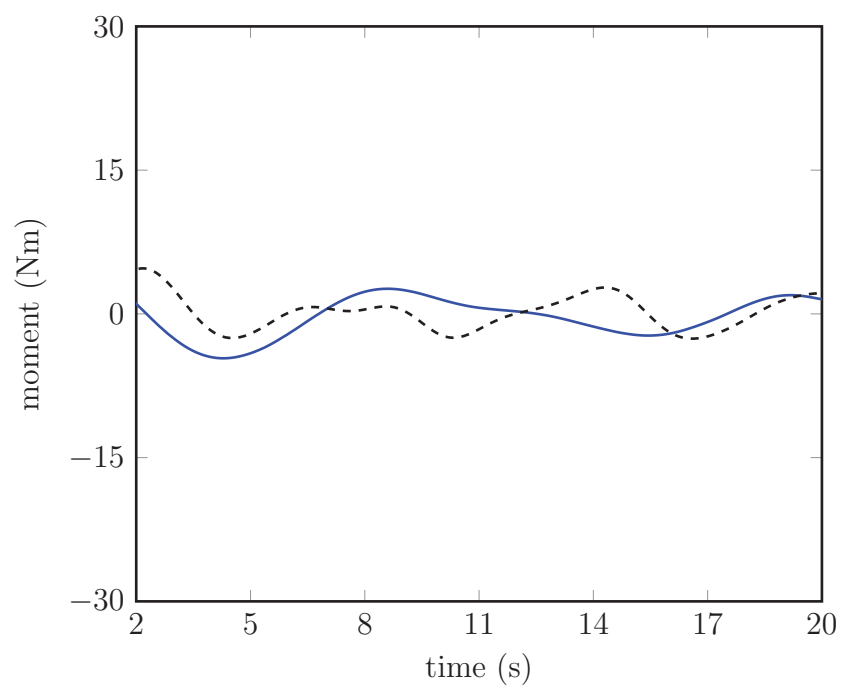


Figure 29: Vertical moment (M_z) for typical ship motion measured experimentally (solid) and simulated using GRM3D (dashed).

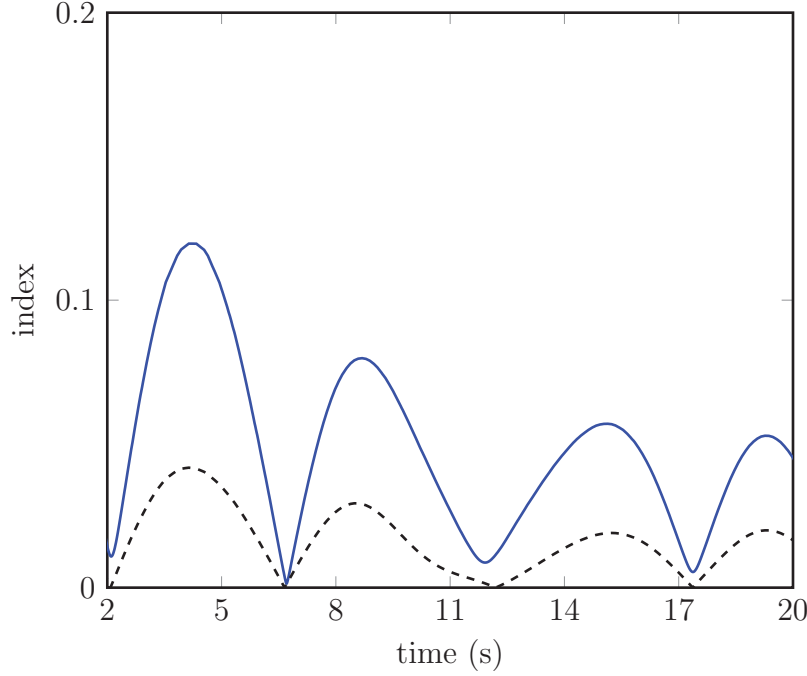


Figure 30: Sliding (solid) and tipping (dashed) indices based on GRM3D simulation results.

Combined with the joint articulation angles, and the full set of interface forces and moments, the MII indices provide the means for estimating likely onsets of MII events.

3.4.2 Modified Indices for a Generic Footprint

The block's only means of resisting any applied moment about the x and y directions is through the location of the normal force. If the normal force needs to be applied outside the bounds of the footprint, the model is said to tip over. In order to generalize the tipping index, the block width is assumed to be not constant, and the required distance of the normal force is calculated based on this assumption.

Assuming the block model is now no longer attached at a singular point below the centre of mass, the normal force intersects the deck at an x and y coordinate appropriate for countering the tipping moments in the x and y directions. The corresponding distances required to counter the x and y moments are:

$$r_y = \frac{M_x}{F_z} \quad (60)$$

$$r_x = \frac{M_y}{F_z} \quad (61)$$

where r_x is the distance in the x direction of the normal force F_z from the centre of mass and r_y is the distance in the y direction of the normal force from the centre of mass; all expressed in the ship coordinate frame. The geometry is illustrated schematically in Figure 31.

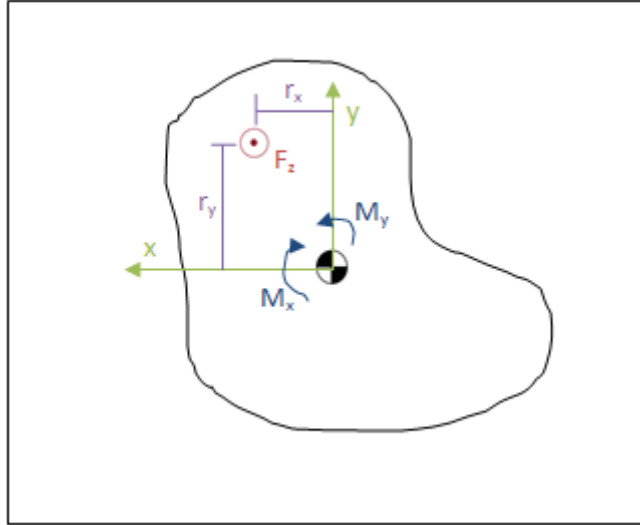


Figure 31: Normal force location to counteract the tipping moments on the block model with a generic footprint

The calculated distances r_x and r_y define the location of the normal force on the ship deck relative to the centre of mass. In order to determine a tipping incident, the next requirement is to determine whether the x and y location of the normal force is contained within the footprint.

It is assumed that the footprint of the Graham model is defined by n points that, when connected in sequence, define a closed polygon. Each vertex of the polygon is required to be defined using Cartesian coordinates relative to the centre of mass. The location of the normal force must be either inside or outside the footprint polygon, as shown in Figure 32. An algorithm to find whether the normal force is within the polygon requires the angle between the point (r_x, r_y) of the normal force and the n th and $n+1$ th vertex points, also shown in Figure 32. Summing all the angles calculated between the vertices results in 360 degrees if the normal force is within the footprint, and 0 degrees if the normal force is outside. These values can be used as thresholds for determining tipping events.

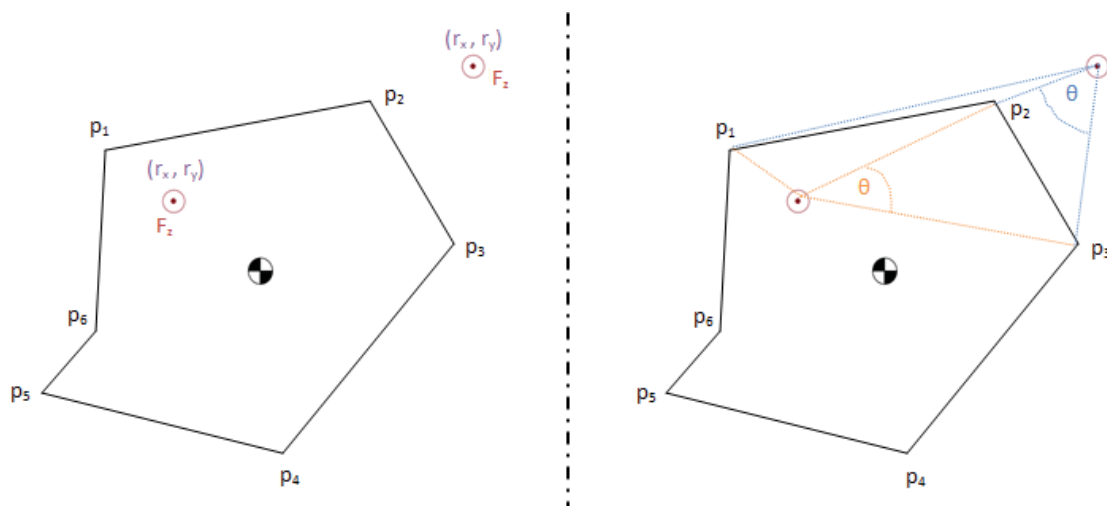


Figure 32: Determining the location of the normal force by the angle between the vertex points on the polygon footprint.

4 Development of Unsteady Shipboard Load Models

4.1 Pendulating Load

The governing dynamics for a three-dimensional shipboard pendulating load are identical to those presented in Equation 35. However, in the case of a pendulating load, the ankle torques (M_x and M_y) do not apply and are simply set to zero, and the attachment point coordinates do not necessarily coincide with the deck. The joint displacement limits as well as the stiffness and damping parameters for the joints can be used to model the actual physical characteristics of the pendulating dynamic system. The resulting mathematical model is called PND3D.

4.2 Cart Load Model Derivation

The second load model used for the investigation of the effect of external shipboard loads is a cart model. The model was defined as a two-mass system. One mass can translate freely, but not rotate, and the second mass can rotate about the first mass, but not translate. The following sections provide the mathematical derivation of the model using Newton's and Euler's equations.

4.3 Model Definition and Coordinate Systems

The two-mass cart system is illustrated schematically in Figure 33. One mass, defined as m_1 , is attached to the deck of the ship, and is placed initially with the centre of mass aligned over point A , as defined in the previous models. This mass has one degree of freedom allowing it to translate in the x direction in the model coordinate frame. The second mass, defined as m_2 is attached to m_1 at a known point R in the model coordinate frame. The vector defining the location of this attachment point, $\{p_{R/B}\}$, is defined with respect to the centre of mass of m_1 . The second mass also only has one degree of freedom. It is only able to rotate about its attachment point to m_1 . The external force is applied to the cart model at an attachment point on m_2 , where the location is defined by a vector with respect to the centre of mass of m_2 .

The coordinate systems used for the derivation can also be seen in Figure 33. The inertial frame and ship frame are the same as defined in the previous model. The model frame [MO] is attached to the ship deck at point A and the x direction is in the same direction as the cart translation direction. Initially the cart is placed such that the centre of mass is above point A . The next coordinate system is called the top coordinate system, [TO]. This coordinate system is attached to m_1 at the point of rotation for m_2 relative to m_1 . Initially the coordinate systems are aligned

such that the x and y directions of the coordinate systems coincide. The rotational transformation from the top coordinate system to the model frame is a rotation about the z axis. This rotation angle is the angle between m_1 and m_2 , and is not a constant value.

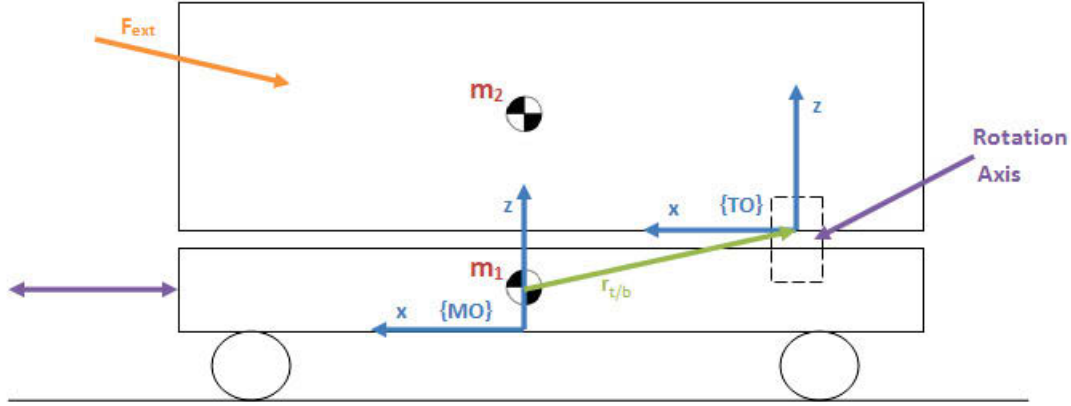


Figure 33: Coordinate systems used in the derivation of in-plane cart load model.

4.4 Kinematics for Two Body Cart

4.4.1 Translating Mass

The position of the centre of mass of mass m_1 , point B , in the inertial frame is defined relative to point A as:

$$\{p\}_B^{IN} = \{p\}_A^{IN} + \{p\}_{B/A}^{IN} \quad (62)$$

Since m_1 is only allowed to translate in the x direction in the model frame, it is advantageous to define the position of the centre of mass with respect to point A in the model frame. This can be done using two rotation matrices, one from the inertial frame to the ship frame, and a second from the ship frame to the model frame knowing that the rotation from the ship frame to the model frame is constant:

$$\{p\}_B^{IN} = \{p\}_A^{IN} + [T_{SHIN}] [T_{MOSH}] \{p\}_{B/A}^{MO} \quad (63)$$

To solve for the velocity at point B , the derivative of the position vector is found to be:

$$\{v\}_B^{IN} = \{v\}_A^{IN} + [\dot{T}_{SHIN}] [T_{MOSH}] \{p\}_{B/A}^{MO} + [T_{SHIN}] [T_{MOSH}] \{v\}_{B/A}^{MO} \quad (64)$$

The derivative of the rotation matrix from the inertial frame to the ship frame can be found using the known ship motions. Note that the velocity of point B with respect

to point A is not constant, but the direction of the vector is known. Taking the derivative of the velocity vector will solve for the acceleration of point B :

$$\begin{aligned} \{a\}_B^{IN} &= \{a\}_A^{IN} + [\ddot{T}_{SHIN}] [T_{MOSH}] \{p\}_{B/A}^{MO} \\ &+ 2 [\dot{T}_{SHIN}] [T_{MOSH}] \{v\}_{B/A}^{MO} + [T_{SHIN}] [T_{MOSH}] \{a\}_{B/A}^{MO} \end{aligned} \quad (65)$$

This is an expression of the acceleration of point B in terms of known quantities. Next the kinematics for the rotating mass m_2 will be derived.

4.4.2 Rotating Mass

The point of attachment for m_2 is defined as point R . So, defining the centre of mass location as point T , the position vector can be written as:

$$\{p\}_T^{IN} = \{p\}_R^{IN} + [T_{SHIN}] [T_{MOSH}] [T_{TOMO}] \{p\}_{T/R}^{TO} \quad (66)$$

Note that the relative position vector has been expressed in the top coordinate frame because it is a known vector in the top coordinate frame. The rotation from the model frame to the top frame is not constant and therefore the derivative of the rotation matrix must be found. The velocity of point T can be found by taking the derivative of the position vector such that:

$$\begin{aligned} \{v\}_T^{IN} &= \{v\}_R^{IN} + [\dot{T}_{SHIN}] [T_{MOSH}] [T_{TOMO}] \{p\}_{T/R}^{TO} \\ &+ [T_{SHIN}] [T_{MOSH}] [\dot{T}_{TOMO}] \{p\}_{T/R}^{TO} \end{aligned} \quad (67)$$

Taking the derivative of the velocity vector will result in the acceleration vector such that:

$$\begin{aligned} \{a\}_T^{IN} &= \{a\}_R^{IN} + [\ddot{T}_{SHIN}] [T_{MOSH}] [T_{TOMO}] \{p\}_{T/R}^{TO} \\ &+ 2 [\dot{T}_{SHIN}] [T_{MOSH}] [\dot{T}_{TOMO}] \{p\}_{T/R}^{TO} + [T_{SHIN}] [T_{MOSH}] [\ddot{T}_{TOMO}] \{p\}_{T/R}^{TO} \end{aligned} \quad (68)$$

As can be seen from Equation 68, the acceleration of point R must be known. This point is on the interface between m_1 and m_2 ; thus, the acceleration is the same at that point on each body. The acceleration of point R can be found similarly to the acceleration of point B on the translating mass. The acceleration of point R in the inertial frame is given by:

$$\begin{aligned} \{a\}_R^{IN} &= \{a\}_A^{IN} + [\ddot{T}_{SHIN}] [T_{MOSH}] \{p\}_{R/A}^{MO} + 2 [\dot{T}_{SHIN}] [T_{MOSH}] \{v\}_{R/A}^{MO} \\ &+ [T_{SHIN}] [T_{MOSH}] \{a\}_{R/A}^{MO} \end{aligned} \quad (69)$$

where the vectors for point R have been expressed in the model frame. This form of the acceleration is not desirable because requires solving for the relative acceleration of point R in the model frame as well. This can be simplified by considering the direction of the acceleration of m_1 in the model frame. Since the body is only allowed to translate in one direction and there is no rotation in the model frame, that means that at any point on the body the velocity and acceleration vectors are the same. This means the equation can be written as:

$$\begin{aligned}\{a\}_R^{IN} = \{a\}_A^{IN} + [\ddot{T}_{SHIN}] [T_{MOSH}] \{p\}_{R/A}^{MO} + 2 [\dot{T}_{SHIN}] [T_{MOSH}] \{v\}_{B/A}^{MO} \\ + [T_{SHIN}] [T_{MOSH}] \{a\}_{B/A}^{MO}\end{aligned}\quad (70)$$

This still requires simplification because the position of point R with respect to point A is not known. This can be defined as a sum of point B with respect to point A and point R with respect to point B such that:

$$\begin{aligned}\{a\}_R^{IN} = \{a\}_A^{IN} + [\ddot{T}_{SHIN}] [T_{MOSH}] (\{p\}_{B/A}^{MO} + \{p\}_{R/B}^{MO}) + \\ 2 [\dot{T}_{SHIN}] [T_{MOSH}] \{v\}_{B/A}^{MO} + [T_{SHIN}] [T_{MOSH}] \{a\}_{B/A}^{MO}\end{aligned}\quad (71)$$

Expanding the equation results in:

$$\begin{aligned}\{a\}_R^{IN} = \{a\}_A^{IN} + [\ddot{T}_{SHIN}] [T_{MOSH}] \{p\}_{B/A}^{MO} + 2 [\dot{T}_{SHIN}] [T_{MOSH}] \{v\}_{B/A}^{MO} + \\ [T_{SHIN}] [T_{MOSH}] \{a\}_{B/A}^{MO} + [\ddot{T}_{SHIN}] [T_{MOSH}] \{p\}_{R/B}^{MO}\end{aligned}\quad (72)$$

which is equal to:

$$\{a\}_R^{IN} = \{a\}_B^{IN} + [\ddot{T}_{SHIN}] [T_{MOSH}] \{p\}_{R/B}^{MO}\quad (73)$$

This method can be verified by solving for the acceleration of point R using another point of reference. The position of point R could also be written as:

$$\{p\}_R^{IN} = \{p\}_B^{IN} + [T_{SHIN}] [T_{MOSH}] \{p\}_{R/B}^{MO}\quad (74)$$

Knowing that the distance between points B and R is constant, because they are on the same body, taking the derivative twice of the position vector will result in the acceleration vector,

$$\{a\}_R^{IN} = \{a\}_B^{IN} + [\ddot{T}_{SHIN}] [T_{MOSH}] \{p\}_{R/B}^{MO}\quad (75)$$

This is the same result as from the previous formulation.

The rotation matrix from the model frame to the top frame is defined by the rotation of m_2 with respect to m_1 . The corresponding rotation angle is not known and must

be solved from the equations, so it is required to rearrange the equation to include this angle. The rotation between the model and top frames is a single rotation about the z axis which is written as:

$$[T_{TOMO}] = \begin{bmatrix} \sin \theta & \cos \theta & 0 \\ \cos \theta & -\sin \theta & 0 \\ 0 & 0 & 0 \end{bmatrix} \quad (76)$$

The first and second derivatives of the rotation matrix are required and can be written as:

$$[\dot{T}_{TOMO}] = \begin{bmatrix} \dot{\theta} \cos \theta & -\dot{\theta} \sin \theta & 0 \\ -\dot{\theta} \sin \theta & -\dot{\theta} \cos \theta & 0 \\ 0 & 0 & 0 \end{bmatrix} \quad (77)$$

and

$$[\ddot{T}_{TOMO}] = \begin{bmatrix} \ddot{\theta} \cos \theta - \dot{\theta}^2 \sin \theta & -\ddot{\theta} \sin \theta - \dot{\theta}^2 \cos \theta & 0 \\ -\ddot{\theta} \sin \theta - \dot{\theta}^2 \cos \theta & -\ddot{\theta} \cos \theta + \dot{\theta}^2 \sin \theta & 0 \\ 0 & 0 & 0 \end{bmatrix} \quad (78)$$

The angular acceleration, which is one of the variables to be solved, is embedded in $[\ddot{T}_{TOMO}]$ and can be factored out of the matrix as:

$$[\ddot{T}_{TOMO}] = \ddot{\theta} \begin{bmatrix} \cos \theta & -\sin \theta & 0 \\ -\sin \theta & -\cos \theta & 0 \\ 0 & 0 & 0 \end{bmatrix} + \begin{bmatrix} -\dot{\theta}^2 \sin \theta & -\dot{\theta}^2 \cos \theta & 0 \\ -\dot{\theta}^2 \cos \theta & \dot{\theta}^2 \sin \theta & 0 \\ 0 & 0 & 0 \end{bmatrix} \quad (79)$$

4.5 Dynamics for Two Body Cart

The dynamic formulation for the cart model uses the Newton Euler equations. Using these equations for the two bodies of the cart will result in a twelve equation second order system. The translating mass m_1 is free to move in the x direction and therefore does not have a resisting force in that direction. This means that the acceleration in the x direction in the model frame is an unknown to be solved. Similarly, the rotating mass m_2 is free to rotate about the z axis in the model frame and therefore does not have a resistive moment in that direction. This introduces the angular acceleration as an unknown. The applied and reaction forces can be seen in the free body diagram in Figure 34.

4.5.1 Linear Dynamics of the Translating Mass

Starting from Newton's equation for m_1 , the sum of the forces at B is related to the acceleration at that point such that:

$$\sum \{F\}_B^{IN} = m_1 \{a\}_B^{IN} \quad (80)$$

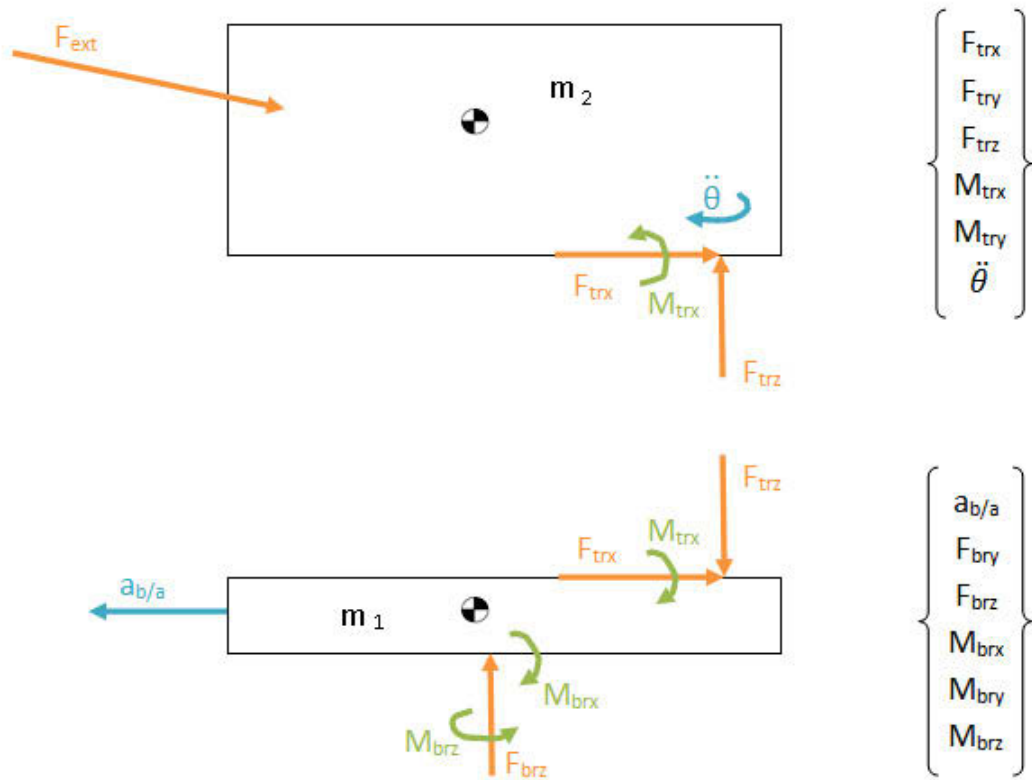


Figure 34: Free body diagram of the two cart masses (m_1 and m_2) with the state variables.

From the free body diagram of m_1 it can be seen that the only external forces acting on it are the reaction forces from the ship deck and from m_2 :

$$\sum \{F\}_B^{IN} = \{F\}_{BR}^{IN} - \{F\}_{TR}^{IN} - m_1 \{g\}^{IN} \quad (81)$$

Substituting Equation 81 into Equation 80 results in:

$$\{F\}_{BR}^{IN} - \{F\}_{TR}^{IN} - m_1 \{g\}^{IN} = m_1 \{a\}_B^{IN} \quad (82)$$

From the kinematic equations, the acceleration of point B is solved in the inertial frame, substituting the solution for the acceleration thereby resulting in:

$$\begin{aligned} \{F\}_{BR}^{IN} - \{F\}_{TR}^{IN} = m_1 [\{a\}_A^{IN} + [\ddot{T}_{SHIN}] [T_{MOSH}] \{p\}_{B/A}^{MO} \\ + 2 [\dot{T}_{SHIN}] [T_{MOSH}] \{v\}_{B/A}^{MO} \\ + [T_{SHIN}] [T_{MOSH}] \{a\}_{B/A}^{MO}] + m_1 \{g\}^{IN} \end{aligned} \quad (83)$$

Placing the unknowns on the left hand side results in:

$$\begin{aligned} \{F\}_{BR}^{IN} - \{F\}_{TR}^{IN} - m_1 [T_{SHIN}] [T_{MOSH}] \{a\}_{B/A}^{MO} = \\ m_1 [\{a\}_A^{IN} + [\ddot{T}_{SHIN}] [T_{MOSH}] \{p\}_{B/A}^{MO} + 2 [\dot{T}_{SHIN}] [T_{MOSH}] \{v\}_{B/A}^{MO} + m_1 \{g\}^{IN} \end{aligned} \quad (84)$$

It is required to solve for the reaction forces in the model frame because F_{BRz}^{MO} is known to be zero. This will then allow for the system to be solved using the twelve available equations:

$$\begin{aligned} [T_{SHIN}] [T_{MOSH}] \{F\}_{BR}^{MO} - [T_{SHIN}] [T_{MOSH}] \{F\}_{TR}^{MO} - m_1 [T_{SHIN}] [T_{MOSH}] \{a\}_{B/A}^{MO} = \\ m_1 [\{a\}_A^{IN} + [\ddot{T}_{SHIN}] [T_{MOSH}] \{p\}_{B/A}^{MO} + 2 [\dot{T}_{SHIN}] [T_{MOSH}] \{v\}_{B/A}^{MO} + m_1 \{g\}^{IN} \end{aligned} \quad (85)$$

where

$$\{a\}_{B/A}^{MO} = \begin{bmatrix} a_{B/A}^{MO} \\ 0 \\ 0 \end{bmatrix} \quad (86)$$

and

$$\{F\}_{BR}^{MO} = \begin{bmatrix} 0 \\ F_{BRy}^{MO} \\ F_{BRz}^{MO} \end{bmatrix} \quad (87)$$

Writting Equation 85 in terms of the state variables results in:

$$\begin{aligned}
& \begin{bmatrix} [T_{SHIN}] [T_{MOSH}] & - [T_{SHIN}] [T_{MOSH}] \end{bmatrix} \begin{Bmatrix} -m_1 a_{B/A}^{MO} \\ F_{Bz}^{MO} \\ F_{By}^{MO} \\ F_{Tx}^{MO} \\ F_{Ty}^{MO} \\ F_{Tz}^{MO} \end{Bmatrix} \\
& = m_1 [\{a\}_A^{IN} + [\ddot{T}_{SHIN}] [T_{MOSH}] \{p\}_{B/A}^{MO} + 2 [\dot{T}_{SHIN}] [T_{MOSH}] \{v\}_{B/A}^{MO}] + m_1 \{g\}^{IN} \quad (88)
\end{aligned}$$

4.5.2 Angular Dynamics of the Translating Mass

This derivation begins with Euler's moment equation in the model coordinate frame with the moments taken about the centre of mass of m_1 :

$$\sum \{M\}_B^{MO} = [I_{BCG}] \{\alpha\}_B^{MO} + \{\omega\}_B^{MO} \times [I_{BCG}] \{\omega\}_B^{MO} \quad (89)$$

where ω_B^{MO} and α_B^{MO} are the rotational velocity and acceleration of the model coordinate frame. These are known from the ship motions. The external moments being applied on m_1 are

$$\sum \{M\}_B^{MO} = \{M\}_{BR}^{MO} - \{M\}_{TR}^{MO} + \{r\}_{BT}^{MO} \times \{F\}_{TR}^{MO} + \{r\}_{B/A}^{MO} \times \{F\}_{BR}^{MO} \quad (90)$$

Substituting Equation 89 into Equation 90 and moving all the unknowns to the left hand side will result in:

$$\begin{aligned}
\{M\}_{BR} - \{M\}_{TR} + \{r\}_{BT}^{MO} \times \{F\}_{TR} + \{r\}_{B/A}^{MO} \times \{F\}_{BR} = \\
[I_B] \{\alpha\}_A + \{\omega\}_A \times [I_B] \{\omega\}_A \quad (91)
\end{aligned}$$

In order to represent Equation 91 in terms of the state variables, the cross products can be expanded to:

$$\begin{aligned}
\{M\}_{BR} - \{M\}_{TR} + \begin{bmatrix} r_{BTy}^{MO} F_{TRz}^{MO} - r_{BTz}^{MO} F_{TRy}^{MO} \\ r_{BTz}^{MO} F_{TRx}^{MO} - r_{BTx}^{MO} F_{TRz}^{MO} \\ r_{BTx}^{MO} F_{TRy}^{MO} - r_{BTy}^{MO} F_{TRx}^{MO} \end{bmatrix} + \begin{bmatrix} r_{B/Ay}^{MO} F_{BRz}^{MO} - r_{B/Az}^{MO} F_{BRy}^{MO} \\ r_{B/Az}^{MO} F_{BRx}^{MO} - r_{B/Ax}^{MO} F_{BRz}^{MO} \\ r_{B/Ax}^{MO} F_{BRy}^{MO} - r_{B/Ay}^{MO} F_{BRx}^{MO} \end{bmatrix} \\
= [I_{BCG}] \{\alpha\}_A^{MO} + \{\omega\}_A^{MO} \times [I_{BCG}] \{\omega\}_A^{MO} \quad (92)
\end{aligned}$$

Remembering that F_{BRz}^{MO} and M_{TRz}^{TO} are equal to zero, writing Equation 92 with expanded vectors produces:

$$\begin{aligned}
\begin{bmatrix} M_{Bx}^{MO} \\ M_{By}^{MO} \\ M_{Bz}^{MO} \end{bmatrix} - [T_{TOMO}] \begin{bmatrix} M_{Tx}^{TO} \\ M_{Ty}^{TO} \\ 0 \end{bmatrix} + \begin{bmatrix} r_{BTy}^{MO} F_{Tz}^{MO} - r_{BTz}^{MO} F_{Ty}^{MO} \\ r_{BTz}^{MO} F_{Tx}^{MO} - r_{BTx}^{MO} F_{Tz}^{MO} \\ r_{BTx}^{MO} F_{Ty}^{MO} - r_{BTy}^{MO} F_{Tx}^{MO} \end{bmatrix} \\
+ \begin{bmatrix} r_{B/Ay}^{MO} F_{Bz}^{MO} - r_{B/Az}^{MO} F_{By}^{MO} \\ r_{B/Az}^{MO} F_{Bx}^{MO} - r_{B/Ax}^{MO} F_{Bz}^{MO} \\ r_{B/Ax}^{MO} F_{By}^{MO} - r_{B/Ay}^{MO} F_{Bx}^{MO} \end{bmatrix} \\
= [I_{BCG}] \{\alpha\}_A^{MO} + \{\omega\}_A^{MO} \times [I_{BCG}] \{\omega\}_A^{MO} \quad (93)
\end{aligned}$$

Writing this in terms of the state variables produces:

$$\begin{aligned}
\begin{bmatrix} -r_{B/Az}^{MO} & r_{B/Ay}^{MO} & 1 & 0 & 0 & 0 & -r_{B/Tz}^{MO} & r_{B/Ty}^{MO} \\ 0 & -r_{B/Ax}^{MO} & 0 & 1 & 0 & r_{B/Tz}^{MO} & 0 & -r_{B/Tx}^{MO} \\ r_{B/Ax}^{MO} & 0 & 0 & 0 & 1 & -r_{B/Ty}^{MO} & r_{B/Tx}^{MO} & 0 \end{bmatrix} [T_{TOMO}] \begin{Bmatrix} F_{By}^{MO} \\ F_{Bz}^{MO} \\ M_{Bx}^{MO} \\ M_{By}^{MO} \\ M_{Bz}^{MO} \\ F_{Tx}^{MO} \\ F_{Ty}^{MO} \\ F_{Tz}^{MO} \\ M_{Tx}^{TO} \\ M_{Ty}^{TO} \end{Bmatrix} \\
= [I_{BCG}] \{\alpha\}_A^{MO} + \{\omega\}_A^{MO} \times [I_{BCG}] \{\omega\}_A^{MO} \quad (94)
\end{aligned}$$

4.5.3 Linear Dynamics of the Rotating Mass

Starting from Newton's equation applied to m_2 , the sum of the forces at point T in the inertial frame are:

$$\sum \{F\}^{IN} = m_2 \{a\}_T^{IN} \quad (95)$$

From the free body diagram, Figure 34, it is seen that the only external forces are the reaction forces at point R and the applied external force F_A so that:

$$\sum \{F\}^{IN} = \{F\}_{TR}^{IN} + \{F\}_A^{IN} - m_2 \{g\}^{IN} \quad (96)$$

Substituting Equation 96 into Equation 95 results in:

$$m_2 \{a\}_A^{IN} = \{F\}_{TR}^{IN} + \{F\}_A^{IN} - m_2 \{g\}^{IN} \quad (97)$$

From the kinematic solution, the acceleration of point T was solved in the inertial frame. Substituting the kinematic solution results in:

$$m_2 [\{a\}_R^{IN} + [\ddot{T}_{SHIN}] [T_{MOSH}] [T_{TOMO}] \{p\}_{T/R}^{TO} + 2 [\dot{T}_{SHIN}] [T_{MOSH}] [\dot{T}_{TOMO}] \{p\}_{T/R}^{TO} + [T_{SHIN}] [T_{MOSH}] [\ddot{T}_{TOMO}] \{p\}_{T/R}^{TO}] = \{F\}_{TR}^{IN} + \{F\}_A^{IN} - m_2 \{g\}^{IN} \quad (98)$$

In Equation 98, the second derivative of the rotation matrix from the top frame to the model frame, $[\ddot{T}_{TOMO}]$, is not known. Substituting the expression for $[\ddot{T}_{TOMO}]$ results in:

$$\begin{aligned} m_2 \left[\{a\}_R^{IN} + [\ddot{T}_{SHIN}] [T_{MOSH}] [T_{TOMO}] \{p\}_{T/R}^{TO} \right. \\ \left. + 2 [\dot{T}_{SHIN}] [T_{MOSH}] [\dot{T}_{TOMO}] \{p\}_{T/R}^{TO} \right. \\ \left. + [T_{SHIN}] [T_{MOSH}] \right. \\ \left. \times \left(\ddot{\theta} \begin{bmatrix} \cos \theta & -\sin \theta & 0 \\ -\sin \theta & -\cos \theta & 0 \\ 0 & 0 & 0 \end{bmatrix} + \begin{bmatrix} -\dot{\theta}^2 \sin \theta & -\dot{\theta}^2 \cos \theta & 0 \\ -\dot{\theta}^2 \cos \theta & -\dot{\theta}^2 \sin \theta & 0 \\ 0 & 0 & 0 \end{bmatrix} \right) \{p\}_{T/R}^{TO} \right] \\ = \{F\}_{TR}^{IN} + \{F\}_A^{IN} - m_2 \{g\}^{IN} \quad (99) \end{aligned}$$

Expanding the equation:

$$\begin{aligned} m_2 \left[\{a\}_R^{IN} + [\ddot{T}_{SHIN}] [T_{MOSH}] [T_{TOMO}] \{p\}_{T/R}^{to} \right. \\ \left. + 2 [\dot{T}_{SHIN}] [T_{MOSH}] [\dot{T}_{TOMO}] \{p\}_{T/R}^{TO} \right. \\ \left. + [T_{SHIN}] [T_{MOSH}] \right. \\ \left. \times \left(\ddot{\theta} \begin{bmatrix} p_{T/Rx}^{TO} \cos \theta - p_{T/Ry}^{TO} \sin \theta \\ -p_{T/Rx}^{TO} \sin \theta - p_{T/Ry}^{TO} \cos \theta \\ 0 \end{bmatrix} + \begin{bmatrix} -p_{T/Rx}^{TO} \dot{\theta}^2 \sin \theta - p_{T/Ry}^{TO} \dot{\theta}^2 \cos \theta \\ -p_{T/Rx}^{TO} \dot{\theta}^2 \cos \theta - p_{T/Ry}^{TO} \dot{\theta}^2 \sin \theta \\ 0 \end{bmatrix} \right) \right] \\ = \{F\}_{TR}^{IN} + \{F\}_A^{IN} - m_2 \{g\}^{IN} \quad (100) \end{aligned}$$

Defining:

$$\{A\} = \begin{bmatrix} p_{T/Rx}^{TO} \cos \theta - p_{T/Ry}^{TO} \sin \theta \\ -p_{T/Rx}^{TO} \sin \theta - p_{T/Ry}^{TO} \cos \theta \\ 0 \end{bmatrix}, \{B\} = \begin{bmatrix} -p_{T/Rx}^{TO} \dot{\theta}^2 \sin \theta - p_{T/Ry}^{TO} \dot{\theta}^2 \cos \theta \\ -p_{T/Rx}^{TO} \dot{\theta}^2 \cos \theta - p_{T/Ry}^{TO} \dot{\theta}^2 \sin \theta \\ 0 \end{bmatrix} \quad (101)$$

and rewriting Equation 100 leads to:

$$m_2[\{a\}_R^{IN} + [\ddot{T}_{SHIN}] [T_{MOSH}] [T_{TOMO}] \{p\}_{T/R}^{TO} + 2 [\dot{T}_{SHIN}] [T_{MOSH}] [\dot{T}_{TOMO}] \{p\}_{T/R}^{TO} + [T_{SHIN}] [T_{MOSH}] \{B\} + [T_{SHIN}] [T_{MOSH}] \{A\} \ddot{\theta}] = \{F\}_{TR}^{IN} + \{F\}_A^{IN} - m_2 \{g\}^{IN} \quad (102)$$

Substituting the expression for $\{a\}_R^{IN}$ from Equation 72 results in:

$$m_2[\{a\}_A^{IN} + [\ddot{T}_{SHIN}] [T_{MOSH}] \{p\}_{B/A}^{MO} + 2 [\dot{T}_{SHIN}] [T_{MOSH}] \{v\}_{B/A}^{MO} + [T_{SHIN}] [T_{MOSH}] \{a\}_{B/A}^{MO} + [\ddot{T}_{SHIN}] [T_{MOSH}] \{p\}_{R/B}^{MO} + [\ddot{T}_{SHIN}] [T_{MOSH}] [T_{TOMO}] \{p\}_{T/R}^{TO} + 2 [\dot{T}_{SHIN}] [T_{MOSH}] [\dot{T}_{TOMO}] \{p\}_{T/R}^{TO} + [T_{SHIN}] [T_{MOSH}] \{B\} + [T_{SHIN}] [T_{MOSH}] \{A\} \ddot{\theta}] = \{F\}_{TR}^{IN} + \{F\}_A^{IN} - m_2 \{g\}^{IN} \quad (103)$$

Rearranging so the unknowns are on the left hand side yields:

$$[T_{SHIN}] [T_{MOSH}] \{F\}_{TR}^{MO} - m_2 [T_{SHIN}] [T_{MOSH}] \{a\}_{B/A}^{MO} - m_2 [T_{SHIN}] [T_{MOSH}] \{A\} \ddot{\theta} = m_2[\{a\}_A^{IN} + [\ddot{T}_{SHIN}] [T_{MOSH}] \{p\}_{B/A}^{MO} + 2 [\dot{T}_{SHIN}] [T_{MOSH}] \{v\}_{B/A}^{MO} + [\ddot{T}_{SHIN}] [T_{MOSH}] \{p\}_{R/B}^{MO} + [\ddot{T}_{SHIN}] [T_{MOSH}] [T_{TOMO}] \{p\}_{T/R}^{TO} + 2 [\dot{T}_{SHIN}] [T_{MOSH}] [\dot{T}_{TOMO}] \{p\}_{T/R}^{TO} + [T_{SHIN}] [T_{MOSH}] \{B\}] - \{F\}_A^{IN} + m_2 \{g\}^{IN} \quad (104)$$

Writing Equation 104 in terms of the state variables results in:

$$[-m_2 [T_{SHIN}] [T_{MOSH}] \{A\} \quad [T_{SHIN}] [T_{MOSH}] - m_2 [T_{SHIN}] [T_{MOSH}]] \begin{Bmatrix} \ddot{\theta} \\ F_{Tx}^{MO} \\ F_{Ty}^{MO} \\ F_{Tx}^{MO} \\ a_{B/A}^{MO} \end{Bmatrix} = m_2[\{a\}_A^{IN} + [\ddot{T}_{SHIN}] [T_{MOSH}] \{p\}_{B/A}^{MO} + 2 [\dot{T}_{SHIN}] [T_{MOSH}] \{v\}_{B/A}^{MO} + [\ddot{T}_{SHIN}] [T_{MOSH}] \{p\}_{R/B}^{MO} + [\ddot{T}_{SHIN}] [T_{MOSH}] [T_{TOMO}] \{p\}_{T/R}^{TO} + 2 [\dot{T}_{SHIN}] [T_{MOSH}] [\dot{T}_{TOMO}] \{p\}_{T/R}^{TO} + [T_{SHIN}] [T_{MOSH}] \{B\}] - \{F\}_A^{IN} + m_2 \{g\}^{IN} \quad (105)$$

4.5.4 Angular Dynamics of the Rotating Mass

This portion of the derivation begins with Euler's moment equation in the top coordinate frame with the moments taken about the centre of mass of m_2

$$\sum \{M\}_T^{TO} = [I_{TCG}] \{\alpha\}_T^{TO} + \{\omega\}_T^{TO} \times [I_{TCG}] \{\omega\}_T^{TO} \quad (106)$$

From the free body diagram, Figure 34, the only external moments are the reaction moments (the moments caused by the reaction forces at point R and the applied external force $\{F\}_A$) such that:

$$\sum \{M\}_T^{TO} = \{r\}_{FA}^{TO} \times \{F\}_A^{TO} + \{M\}_{TR}^{TO} + \{r\}_{TR}^{TO} \times \{F\}_{TR}^{TO} \quad (107)$$

The applied moment is known in the inertial frame, and the solution for the reaction forces is in the model frame. Transforming the forces into consistent coordinate frames allows the expression to be written as:

$$\begin{aligned} \sum \{M\}_T^{TO} = \{r\}_{FA}^{TO} \times [T_{INSH}] [T_{SHMO}] [T_{MOTO}] \{F\}_A^{IN} + [T_{MOTO}] \{M\}_{TR}^{MO} \\ + \{r\}_{TR}^{TO} \times [T_{MOTO}] \{F\}_{TR}^{MO} \end{aligned} \quad (108)$$

Substituting Equation 108 into Equation 106 results in:

$$\begin{aligned} \{r\}_{FA}^{TO} \times [T_{INSH}] [T_{SHMO}] [T_{MOTO}] \{F\}_A^{IN} \\ + [T_{MOTO}] \{M\}_{TR}^{MO} + \{r\}_{TR}^{TO} \times [T_{MOTO}] \{F\}_{TR}^{MO} \\ = [I_{TCG}] \{\alpha\}_T^{TO} + \{\omega\}_T^{TO} \times [I_{TCG}] \{\omega\}_T^{TO} \end{aligned} \quad (109)$$

Since rotation of the top coordinate frame is known with respect to the model axes, the total rotation of the top mass and the derivatives can be written as:

$$\{\theta\}_T^{TO} = \{\theta\}_B^{TO} + \{\theta\}_{T/B}^{TO} \quad (110)$$

$$\{\omega\}_T^{TO} = \{\omega\}_B^{TO} + \{\omega\}_{T/B}^{TO} \quad (111)$$

$$\{\alpha\}_T^{TO} = \{\alpha\}_B^{TO} + \{\alpha\}_{T/B}^{TO} \quad (112)$$

where,

$$\{\omega\}_{T/B}^{TO} = \begin{bmatrix} 0 \\ 0 \\ \dot{\theta} \end{bmatrix} \quad \text{and} \quad \{\alpha\}_{T/B}^{TO} = \begin{bmatrix} 0 \\ 0 \\ \ddot{\theta} \end{bmatrix} \quad (113)$$

Substituting these expressions into Equation 109 results in:

$$\begin{aligned} \{r\}_{FA}^{TO} \times [T_{INSH}] [T_{SHMO}] [T_{MOTO}] \{F\}_A^{IN} + [T_{MOTO}] \{M\}_{TR}^{MO} \\ + \{r\}_{TR}^{TO} \times [T_{MOTO}] \{F\}_{TR}^{MO} \\ = [I_{TCG}] (\{\alpha\}_B^{TO} + \ddot{\theta}) + (\{\omega\}_B^{TO} + \dot{\theta}) \times [I_{TCG}] (\{\omega\}_B^{TO} + \dot{\theta}) \end{aligned} \quad (114)$$

Rearranging Equation 114 such that the unknowns are on the left hand side yields:

$$\begin{aligned}
\begin{bmatrix} M_{T_x}^{TO} \\ M_{T_y}^{TO} \\ 0 \end{bmatrix} + \{r\}_{TR}^{TO} \times [T_{MOTO}] \{F\}_{TR}^{MO} - [I_{TCG}] \begin{bmatrix} 0 \\ 0 \\ \ddot{\theta} \end{bmatrix} \\
= (\{\omega\}_B^{TO} + \dot{\theta}) \times [I_{TCG}] (\{\omega\}_B^{TO} + \dot{\theta}) + [I_{TCG}] \{\alpha\}_B^{TO} + \\
\{r\}_{FA}^{TO} \times [T_{INSH}] [T_{SHMO}] [T_{MOTO}] \{F\}_A^{IN} \quad (115)
\end{aligned}$$

The cart dynamic solution is obtained by solving Equations 88, 94, 105, and 115 simultaneously. Combined, twelve equations are available to solve for the twelve unknown state variables. The resulting simulation model is called CRT3D.

4.6 Interface Force

Figure 35 shows schematic representations of a postural model (either the quasi-static model or the dynamic model) interacting with a typical unsteady shipboard load (either a pendulating load or a co-planar (cart-type) load). In both cases, the postural model is attached to the unsteady load by the directed element shown schematically in Figure 36.

The directed element consists of a tension/compression force-producing member that can generate forces that depend upon the relative position and relative velocity between its two attachment points as well as some nonlinear behaviours. As implemented, the directed element has distinct linear stiffness properties in the tension and compression directions; distinct viscous damping properties in the tension and compression directions; as well as options for tension-only, compression-only, and no transmitted force behaviours to represent tensioned lines/cables, unattached push poles, and loss of contact situations, respectively.

This resulting simulation model is called INTFRC.

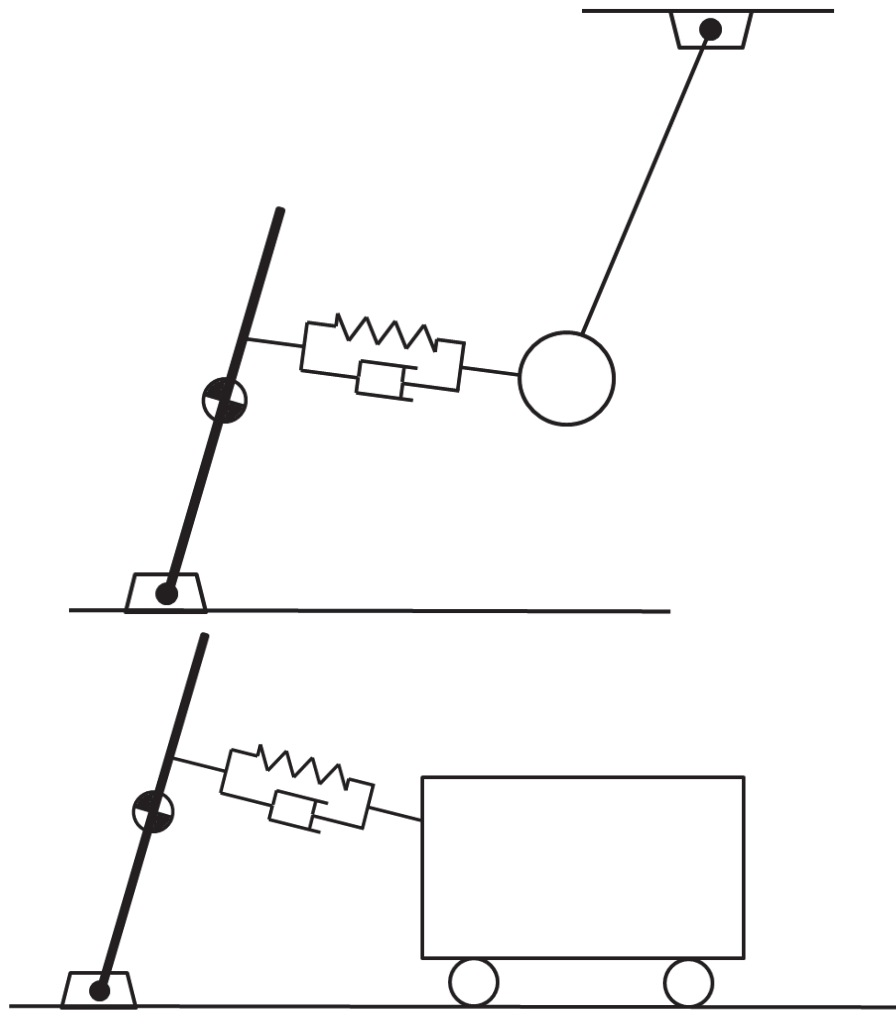


Figure 35: Schematic representation of postural stability models interacting with the pendulating load (left) and cart load (right).

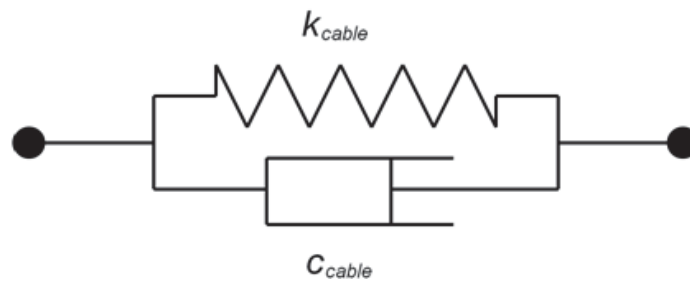


Figure 36: Directed element model.

5 Physical Validation Experiment

5.1 Mechanical Hardware

The mechanical hardware of the validation apparatus is intended to accurately represent the dynamic models of the spatial inverted pendulum, pendulating load, cart load, and coupling models such that physical validation of these dynamic models can be completed. The mechanical hardware apparatus is naturally divided into four primary systems as the spatial inverted pendulum, pendulating load, cart load, and tension/compression link. The design of these four systems is described here. Not included are detailed design parameters of the MOOG six-degree-of-freedom motion platform used to subject the mechanical hardware to simulated ship motion as this is a standard commercial piece of equipment.

5.1.1 Scale Assessment

Given the nature of the dynamic validation to be performed, the determination of scale of the mechanical hardware was driven primarily by assessment of feasibility and cost. As the scale of the hardware increases the cost of components and raw materials does so as well. Likewise, the complexity of the hardware increases with increasing scale. Driving this trend towards increasing scale is the observation that a scale of 1:1 with real-life equivalents of the dynamic models gives the hardware the potential to be used in experiments involving human subjects sometime in the future. The scale of the hardware designed and manufactured can be observed in Figure 37.

The first critical aspect of the hardware that allows 1:1 scale to be achieved is mass. With target weights of up to a 200 lb (890 N) spatial inverted pendulum, and 400 lb (1780 N) dynamic loads, a low-cost source of mass is needed. While dense materials such as sand and water were considered, they would have resulted in increased hardware complexity. Thirty-five pound (157 N) weightlifting plates were used instead, as they provide simple implementation, and acceptable cost at approximately one dollar per pound (4.4 N).

The second critical requirement to achieve 1:1 scale of the hardware is control authority of the spatial inverted pendulum. Since the inverted pendulum is actively controlled, it is identified that to achieve 1:1 scale the control system must be capable of generating 200 ft-lb (271 Nm) of torque at the inverted pendulum's rotation centre, about either axis of rotation. This value is estimated as the typical amount of self-righting torque that a person could generate without altering his or her stance. This amount of torque is feasible with a geared servo-motor system, as will be described later.

With these two critical requirements satisfied, it follows that the mechanical valida-

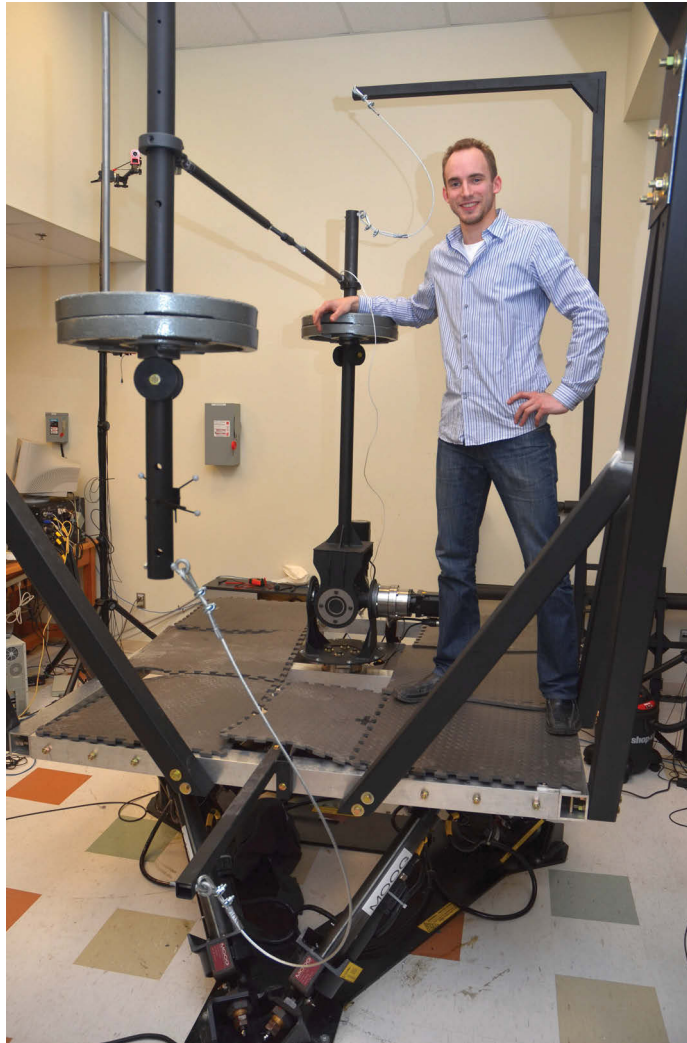


Figure 37: *Experimental set-up for spatial inverted pendulum stability model coupled with pendulating load model.*



Figure 38: *Spatial inverted pendulum model.*

tion hardware is designed at a 1:1 scale. All hardware is designed to be installed on a suitably-sized MOOG six-degree-of-freedom motion platform. Use of readily available components is maximized to keep costs to a minimum, and mild steel is used for custom hardware structures and components due to its high stiffness, moderate strength, good weldability, and low cost.

5.1.2 Actively Controlled Spatial Inverted Pendulum

Figure 38 shows the complete spatial inverted pendulum system. To achieve control torque of up to 200 ft-lb (271 Nm), Kollmorgen AKM-42E electric servo motors are paired with Apex Dynamics AE-120-100 and AER-120-100 gear sets. These gear sets provide a large reduction ratio of 100:1 so that the rated motor output torque of 2.3 ft-lb (3.1 Nm) is sufficient. For anticipated pendulum rotation of 30 degrees per second, approximately 500 RPM motor speed is expected. This operating state is within the AKM-42E motor capability for continuous operation. These drive components are shown in Figures 39, 40, and 41.

The AER-120-100 gearbox, which includes a 90 degree elbow between gear stages, is required so that the drive system attached to the moving portion of the inverted pendulum universal joint does not strike the ground during motion.

The spatial inverted pendulum uses a unique form of control input. Unlike clas-

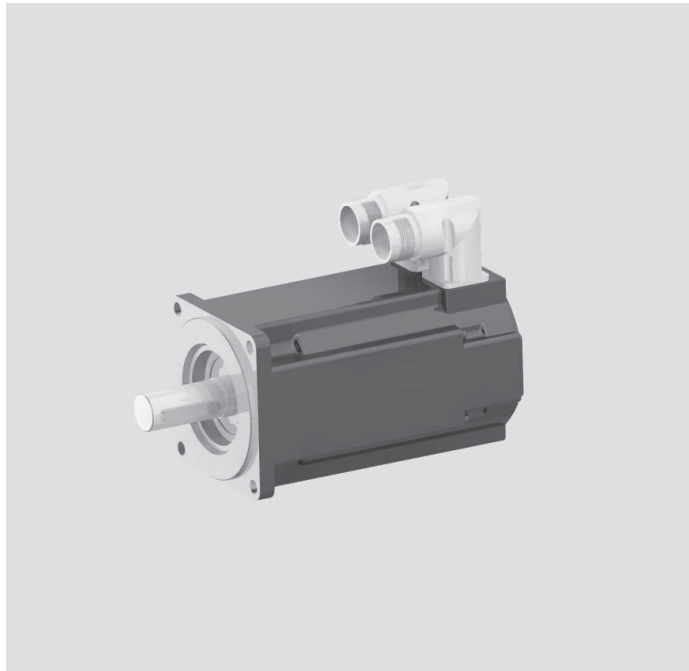


Figure 39: *Inverted pendulum articulation motor.*

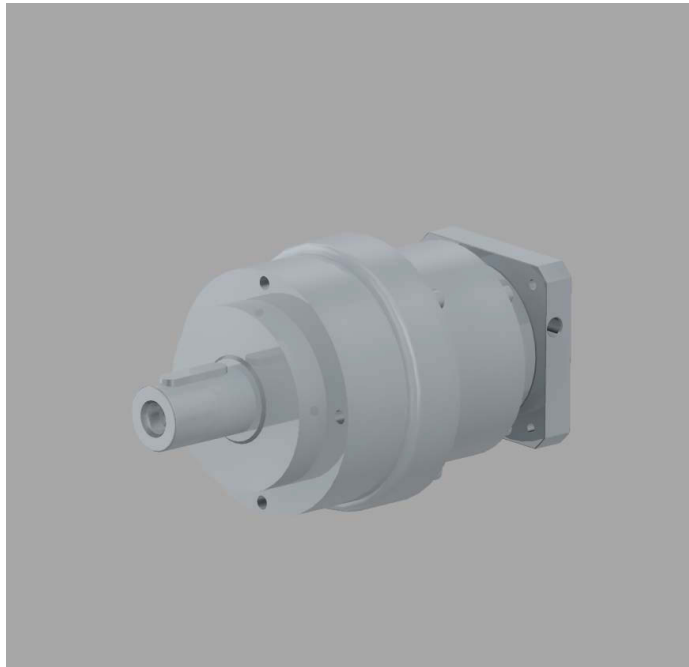


Figure 40: *Inverted pendulum straight gearbox.*



Figure 41: *Inverted pendulum right-angle gearbox.*

sical examples of inverted pendulums, control torque is given to a single rotation centre comprised of two intersecting, perpendicular axes of rotation. This feature is a requirement to accurately recreate the dynamic model of the spatial inverted pendulum with two degrees of rotational freedom. Such torque input is facilitated using a custom-designed universal joint, shown in Figure 42. Two perpendicular rotation pins are machined to interface with the keyed output shafts of the AE-120 and AER-120 gear sets. Torque from the gear sets is then applied to the rotation centre of the inverted pendulum through the two intersecting perpendicular axes of these rotation pins. A custom u-joint was required for this application to accommodate the large diameters of the AE-120 and AER-120 gear set output shafts. Stress analysis corresponding to 200 ft-lb (271 Nm) of input torque is shown in Figure 43.

The u-joint component is completed using four off-the-shelf ball bearings and siding structures comprised of laser-cut mild steel segments. Components are joined using MIG welding techniques. The u-joint is installed on two laser-cut steel discs with hole patterns that allow the inverted pendulum to be rotated in 15 degree increments relative to the base structure on which it is mounted.

The spatial inverted pendulum is completed using 1.5 inch (3.8 cm) schedule 40 steel pipe affixed atop the u-joint to rigidly hold the 35 lb (157 N) mass plates at a desirable distance from the rotation centre. Up to five mass plates can be accommodated at any time.

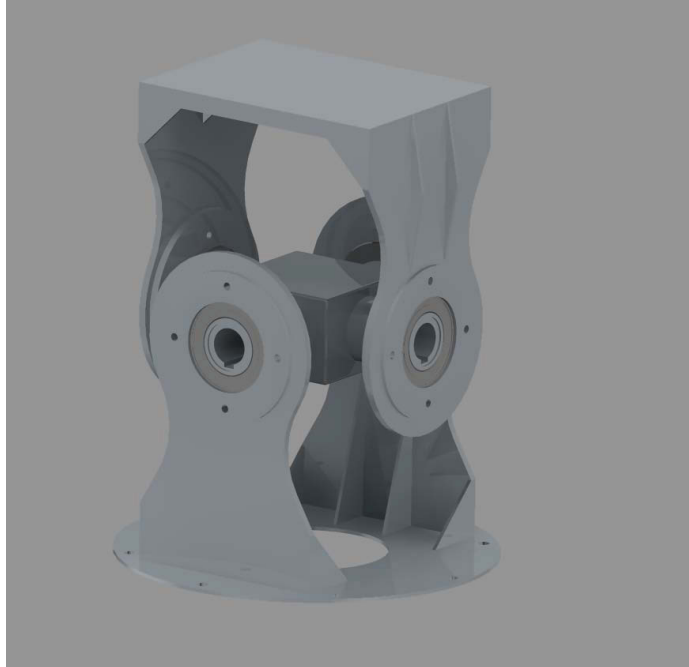


Figure 42: *Inverted pendulum custom-designed universal joint.*

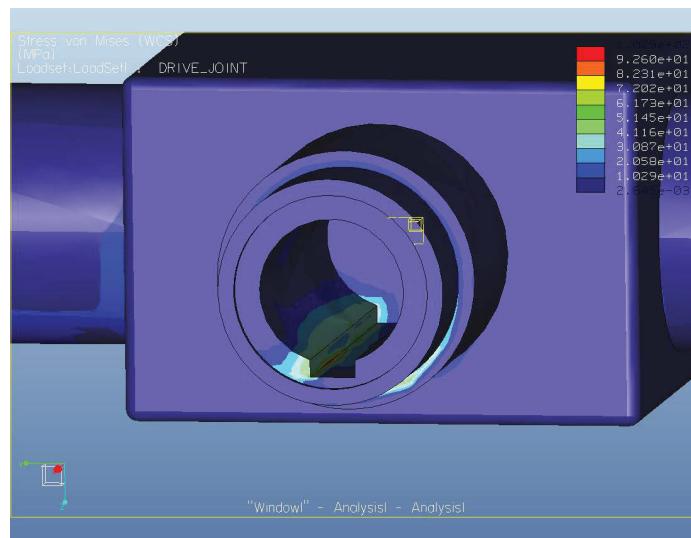


Figure 43: *Stress analysis results for the universal joint.*



Figure 44: Solid model of the pendulating load arrangement.

5.1.3 Pendulating Load

The pendulating load model is illustrated in Figure 44. The pendulating load is comprised of a section of 1.5 inch (3.8 cm) schedule 40 steel pipe hung from a universal joint. The universal joint is held in place 100 inches (2.54 m) above the motion platform by a steel support structure. Since the design static weight of the pendulating load is up to 400 lb (1780 N), a substantial support structure is required. Three-inch (7.6 cm) square steel tube is used to create the space frame structure which is sized for adequate stiffness of the u-joint mount location. Figures 45 and 46 show the results of displacement and stress analyses respectively, when the structure is subjected to a worst-case scenario loading situation arising from 3-G acceleration of the 400 lb (1780 N) pendulating load.

Another critical component in the pendulating load design is the steel pin which connects the universal joint to the support structure. This is the single component which must transfer forces from the pendulum load to its support structure. The stress analysis for this pin is shown in Figure 47. For this worst case scenario loading, an acceptable safety factor of approximately 6 is achieved with respect to typical mechanical properties of mild steel.

Thirty-five pound (156 N) mass plates are hung at discretely adjustable locations along the length of the pendulum shaft, which can accommodate up to eleven plates. The complete pendulating load hardware with one half of the support structure omit-

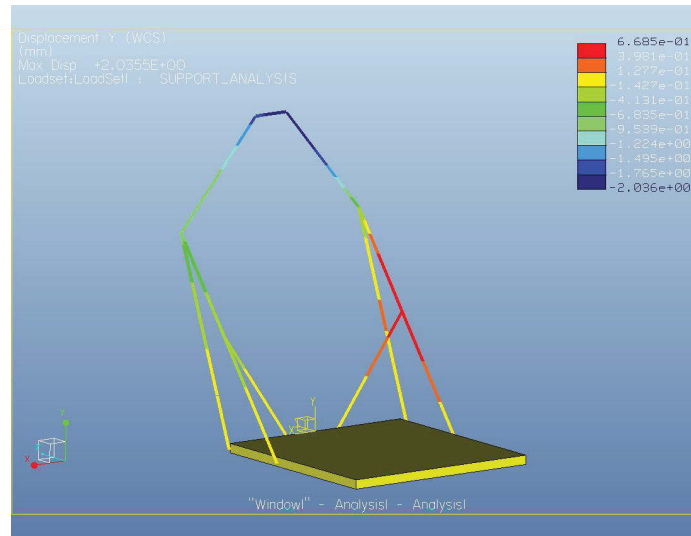


Figure 45: Displacement analysis results for the pendulating load.

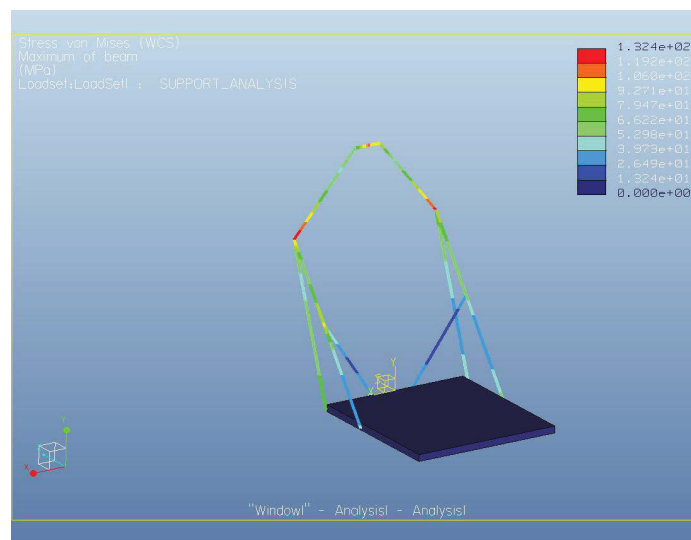


Figure 46: Stress analysis results for the pendulating load.

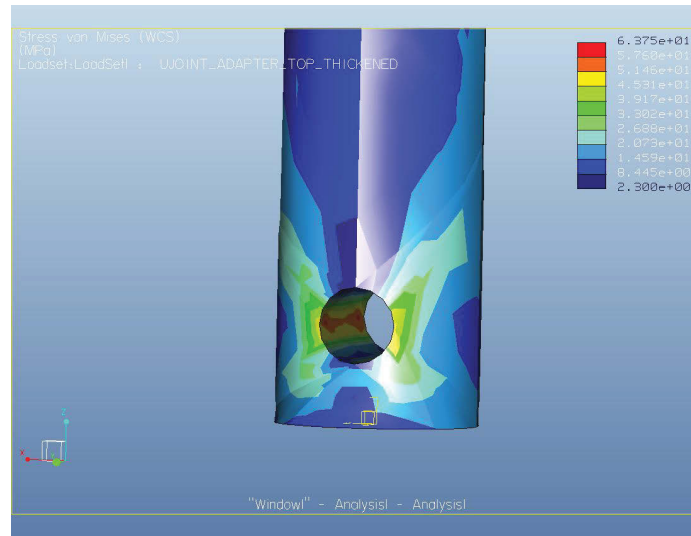


Figure 47: Stress analysis results for the pendulating load securing pin.

ted for clarity is shown in Figure 44.

5.1.4 Cart Load

The cart load hardware consists of two moving components: a translating base and a rotational structure mounted on top of the translating base. The intent of this design is to facilitate reconfiguration of the hardware to accommodate various motion states including single degree of freedom translation, or combined translation and rotation. The translating base, shown in Figure 48, travels within two rail guides comprised of structural steel C-channel and off-the-shelf roller guides. The C-channel is sized to provide adequate stiffness of the support structure.

Translation of the rotational structure relative to the translating base is constrained by ball bearings and shear pins. By installing one shear pin, rotation is allowed about its axis. The shear pin can be installed in any one of three bearing locations to allow reconfigurable rotation centres for the cart load. Rotation is prevented when shear pins are installed in any two of the bearing locations. The rotational structure is supported by four ball transfers that act on a large laser cut steel sheet. This sheet is backed by a steel frame structure designed to cover the expected path of the ball transfers to the greatest extent possible. Displacement analysis of a worst case loading situation is shown in Figure 49, which shows adequate plate stiffness.

A section of 1.5 inch (3.8 cm) schedule 40 steel pipe is mounted at one end of the rotational structure, serving as a location where interface forces can be applied. The rotational structure is also the mounting location for up to eleven 35 lb (156 N) mass plates. Figure 50 shows the assembled cart load hardware.

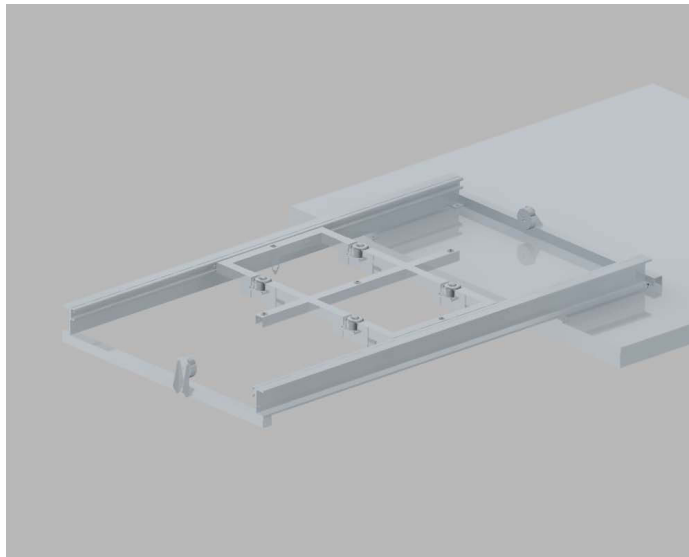


Figure 48: Cart load translating base design.

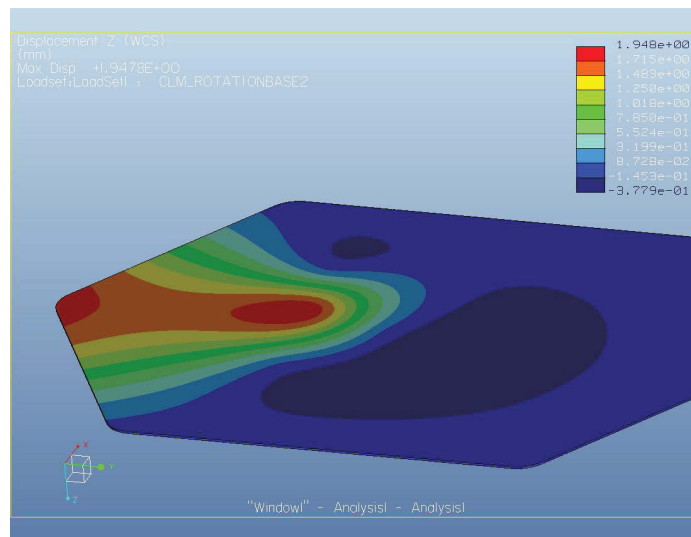


Figure 49: Cart load displacement analysis results.

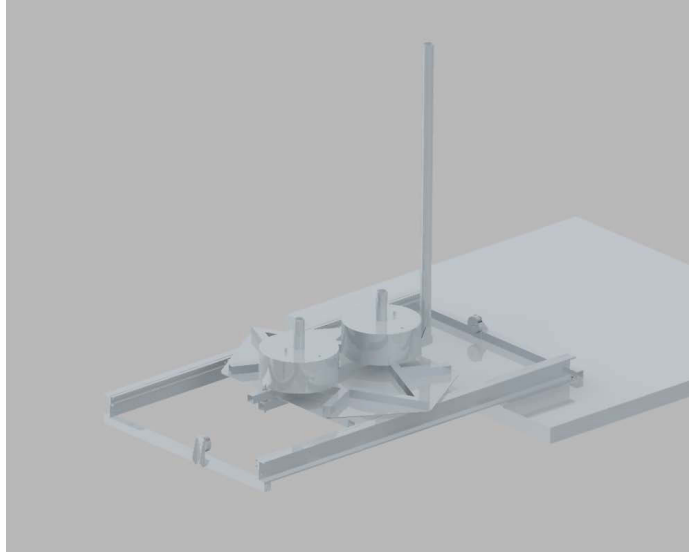


Figure 50: Solid model of the assembled cart load arrangement.

5.1.5 Tension/Compression Link

Interface forces between the actively-controlled spatial inverted pendulum and the dynamic load hardware are transferred via a rigid tension/compression link. The link is made of $\frac{1}{2}$ inch (1.3 cm) schedule 40 steel pipe segments and a combination of right- and left-handed threaded rods for simple length adjustment. The link connects to the inverted pendulum and dynamic load hardware using steel set screw collars which fasten to the 1.5 inch (3.8 cm) steel pipe used in all three primary hardware systems. To allow the necessary degrees of freedom between the inverted pendulum and dynamic load systems, a universal joint connects the steel pipe to one of the set screw collars while a spherical bearing rod-end connects the other. These connections allow sufficient degrees of freedom to obtain a link which is subjected only to tensile or compressive forces. Two versions of the tension compression link are manufactured: one for connecting the inverted pendulum to the pendulating load, and the other for connecting it to the cart load. The designs are identical with the exception of the required lengths of the steel pipe and the threaded rod.

Figures 51 and 52 show how the tension/compression link is implemented to connect the spatial inverted pendulum to the pendulating load and cart load, respectively.

5.1.6 Safety Structures

It is important to limit the allowable travel of the three primary mechanical systems so that design loads are not exceeded and collisions between the dynamic loads and their support structures are not possible. Steel cable is used to limit the angular rotations



Figure 51: Implementation of the tension/compression link with the pendulating load model.

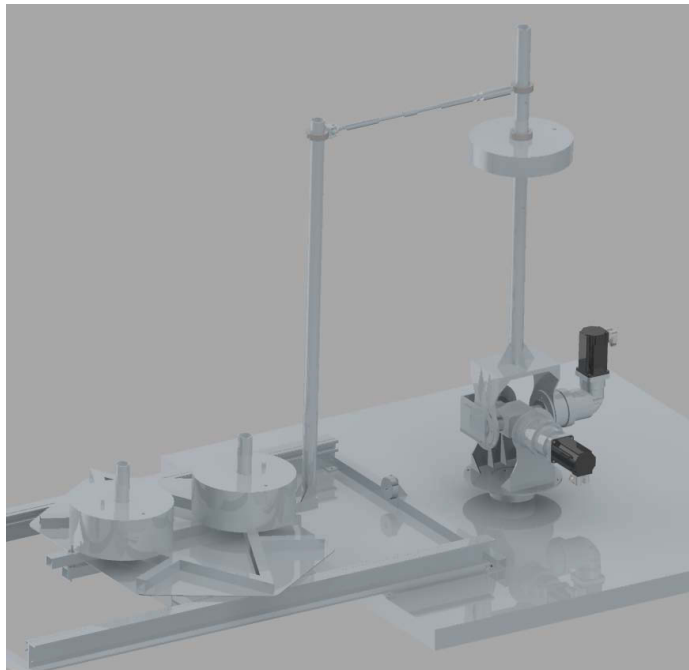


Figure 52: Implementation of the tension/compression link with the cart load model.

of the inverted pendulum and pendulating load such that a pre-defined maximum rotation is allowed in any direction. The steel cable, rated to 840 lb (3740 N), is generously sized. Rotation and displacement of the cart load hardware is limited by strategic placement of galvanized rubber bump-stops. A steel cable tether is also used to provide redundancy in the connection of the rotational cart structure to its translating base.

5.2 Instrumentation

For validation of the dynamic models and active control of the spatial inverted pendulum to be possible, several key displacements, rotations, and interface forces must be measured and recorded from the mechanical hardware while it is subjected to simulated ship motion from the six-degree-of-freedom motion platform. More specifically, the following measurements are required.

5.2.1 Spatial Inverted Pendulum Rotations and Mounting Interface Reactions

Angular rotation of the inverted pendulum is required to track its movement relative to the motion platform and facilitate active control. These measurements are made using quadrature encoders which are integrated within the AKM-42E motors. By applying the gear reduction ratio of 100:1 to the encoder outputs, the angular rotations of the inverted pendulum relative to the motion platform are obtained.

Interface forces between the base of the spatial inverted pendulum and the motion platform are measured using a six-axis load cell to obtain the six force and moment reaction components. For this purpose, the Theta-model six-axis load cell from ATI Industrial Automation, shown in Figure 53, is used as the rigid connection between the inverted pendulum hardware and the motion platform.

5.2.2 Pendulating Load Rotations

The rotation of the pendulating load about its support location is tracked using an optical motion capture system called OptiTrack by NaturalPoint. The system consists of eight infra-red (IR) cameras placed around the pendulating load which track the rigid body motion using a reflective marker setup. Arena software, provided by NaturalPoint, is used to process the data from the IR cameras and create rigid body trajectories for the pendulating load. From this data, the two measures of rotation angle of the pendulating load relative to the stationary cameras are obtained. The camera and rigid body setup used to track the pendulating load motion, as seen through the Arena software, is shown in Figure 54.

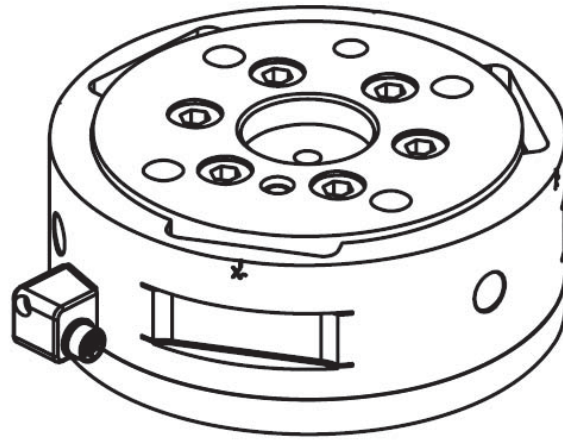


Figure 53: Inverted pendulum base load cell.

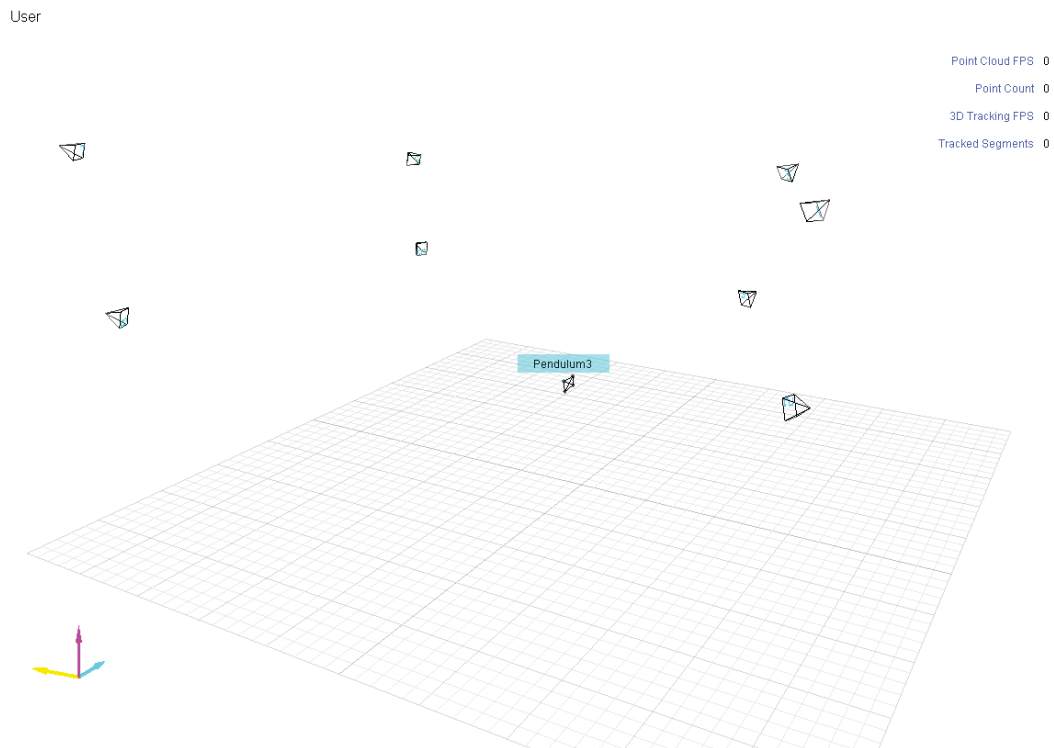


Figure 54: Configuration of OptiTrack system.



Figure 55: *Cart load encoders.*

5.2.3 Cart Load Displacement and Rotation

The displacement and rotation of the cart load is measured using National Instruments 8 mm thru-bore quadrature encoders shown in Figure 55. At 1000 counts per revolution, a rotational precision of 0.36 degrees is obtained. To measure translation of the translating base relative to its support rails, an encoder is fitted with a drive wheel as shown in Figure 56 and is attached to the translating cart base. A flexible cable attached to the cart load support structure wraps around the encoder drive wheel such that translation of the translating cart base causes proportional rotation of the encoder. To measure rotation of the cart load relative to its support structure, an encoder is affixed between the rotational cart structure and the shear pin. These components have been described previously in Section 5.1.4.

5.2.4 Tension/Compression Link Interface Force

The tensile or compressive interface force acting between the spatial inverted pendulum and the dynamic loads is measured using a single-axis tension/compression load cell. The LC-202 load cell from Omega Engineering is used with calibration to 300 lb (1330 N) of tensile or compressive force. This load cell is paired with an Omega Engineering DMD-465 strain amplifier to output an analog 0–10 V signal to the data acquisition equipment. Figures 57 and 58 show the load cell and strain amplifier, respectively.



Figure 56: *Cart load translational encoder interface wheel.*



Figure 57: *Omega Engineering LC-202 load cell.*



Figure 58: Omega Engineering DMD-464 strain amplifier.

5.2.5 Mass Properties

The mass properties of the mechanical validation hardware are needed for meaningful comparison of test results to the outputs from the associated dynamic models. To this end, the total mass and inertia tensors are calculated using the solid modelling software Pro ENGINEER Wildfire Version 5.0. Since all components of the mechanical hardware are accurately represented in this program, assessment of the hardware mass properties is accomplished when appropriate material densities are applied to all components. Simple validation cases of measured weight of the spacial inverted pendulum indicate approximate error of less than one percent using this method. Sample mass property output files from Pro ENGINEER are provided in Annex B.

5.3 Control and Data Acquisition

LabVIEW, created by National Instruments, is a graphical programming language that facilitates software communication with electronic motors and sensors. The software configuration for the spatial inverted pendulum validation experiment is focused around the operation of a few LabVIEW programs, referred to as virtual instruments (VIs). The primary reason for this is because the servo motors used to control the inverted pendulum's two degrees of freedom are most easily programmed in LabVIEW. In order to simplify and coordinate the data gathering process as much as possible, LabVIEW VIs are used for data collection, processing, and recording. Data are transferred between VIs using global variables, which when created can be

accessed by all VIs running in LabVIEW.

A diagram of the control and data acquisition components is shown in Figure 59. The motion platform controller (1), sends position commands to the motion base, and transfers platform positions over a network UDP connection to the UDP Receiver VI (2), which then stores the positions as global variables. This occurs at approximately 60 Hz, which is the update rate of the motion platform. The two-axis servo motor feedforward control VI (3) uses the platform angular positions to calculate what the inverted pendulum position should be in order to remain vertical. It sends position commands to the servo motor hardware feedback control (4), an FPGA controller provided by the manufacturer which runs at 4000 Hz. Current angular positions of the inverted pendulum are measured using motor encoders, and are stored in global variables for recording. The six-axis load cell data receiver and one-axis load cell data receiver VIs (5) gather their respective force data and store them in global variables at approximately 100 Hz. The data logger VI (6) gathers all of the data that are stored in global variables and records them with the current time to a spreadsheet file at 100 Hz. The position of the pendulum is recorded using Optitrack position tracking (7). Four markers fixed to the pendulum allow its angle to be determined in 3D space. The cart encoder receiver (8) receives the positions of the encoders installed on the cart that measure cart translational position and orientation. The encoder values in counts are converted into engineering units and transferred to the data logger VI.

5.4 Experimental Validation of the Graham and Inverted Pendulum Stability Models

The main results from the Graham and inverted pendulum stability models were the reaction forces and moments acting at the base of the model. The test cases are designed to isolate these variables and incrementally increase the degrees of freedom being validated. For the experimentation, the weight added to the apparatus was 70 lbf (31.75 kg). The parameters of the physical model were calculated from the Pro ENGINEER CAD model used to design the hardware. The physical parameters were calculated within the program and are provided in Table 3.

To isolate a translational acceleration, a constant frequency sinusoidal sway motion was used. This motion profile allowed for isolation of a translational degree of freedom, as well as providing a smooth acceleration profile to the model. In order to remain within the motion platform performance limitations, the amplitude of the motion was selected to be 0.1 m with a frequency of 0.5 rad/sec. A second motion profile isolated an angular degree of freedom by using a constant frequency sinusoidal roll motion. The roll motion had an amplitude of 0.1 rad and a frequency of 0.5 rad/sec in order to remain within the platform motion limits. Following the

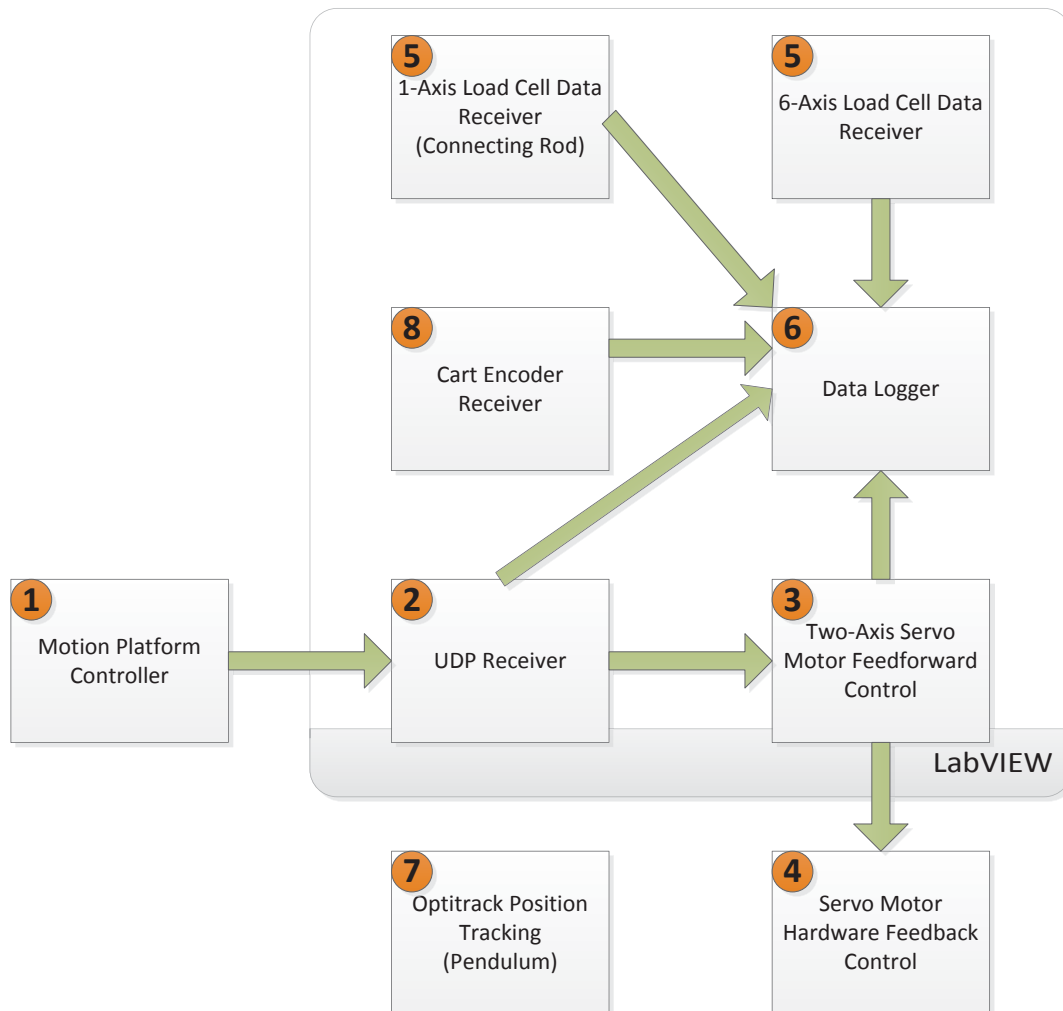


Figure 59: High-level view of control and data acquisition components.

Table 3: Simulation parameters used with GRM3D and PSM3D

Parameter	Value
m	63.7 kg
I_{xx}	78555 kg m ²
I_{yy}	777746 kg m ²
I_{zz}	6060 kg m ²
$\mathbf{r}_{CG/A}^{MO}$	$\{-0.6 \ 0.34 \ 0.75\}^T$ m
g	9.81 m/sec ²

constant frequency sinusoidal motion, a frequency sweep sinusoidal motion was performed. This motion had the advantage of determining the frequency response of the system. The frequency sweep was performed for both a single degree of freedom translational and angular motion in the sway and roll directions respectively. The frequency swept from 0.1 rad/sec through 0.5 rad/sec. The final validation motion profile for the stability models was a six degree of freedom representative ship motion. This general motion case was used to validate the model for all six degrees of freedom to ensure the results were acceptable. The ship motion was generated based on representative frigate and sea state data.

The results from the physical apparatus were the forces and moments at the base measured using the load cell. The load cell was sampling results at 100 Hz and had high frequency noise. The noise was filtered out using a fourth-order two-pass Butterworth filter. Additional post processing of the data was needed in order to line up the experimental coordinate frames with the simulation coordinate frames. The experimental coordinate frames can be seen in Figure 60. In order to compare the two sets of results the experimental results were rotated to the dynamic model frame. First to note is that the motion platform does not have the same coordinate system as the dynamic model. This means that the input motions needed to be rotated to the dynamic coordinate system. That required a simple transformation matrix

$$\begin{bmatrix} T_{\text{DynamicModel}}^{\text{Platform}} \end{bmatrix} = \begin{bmatrix} 1 & 0 & 0 \\ 0 & -1 & 0 \\ 0 & 0 & 1 \end{bmatrix} \quad (116)$$

A similar transformation matrix can be used to rotate the forces from the load cell to the dynamic model coordinate frame. The angle between the dynamic model and the load cell frames was approximately measured as 45 degrees

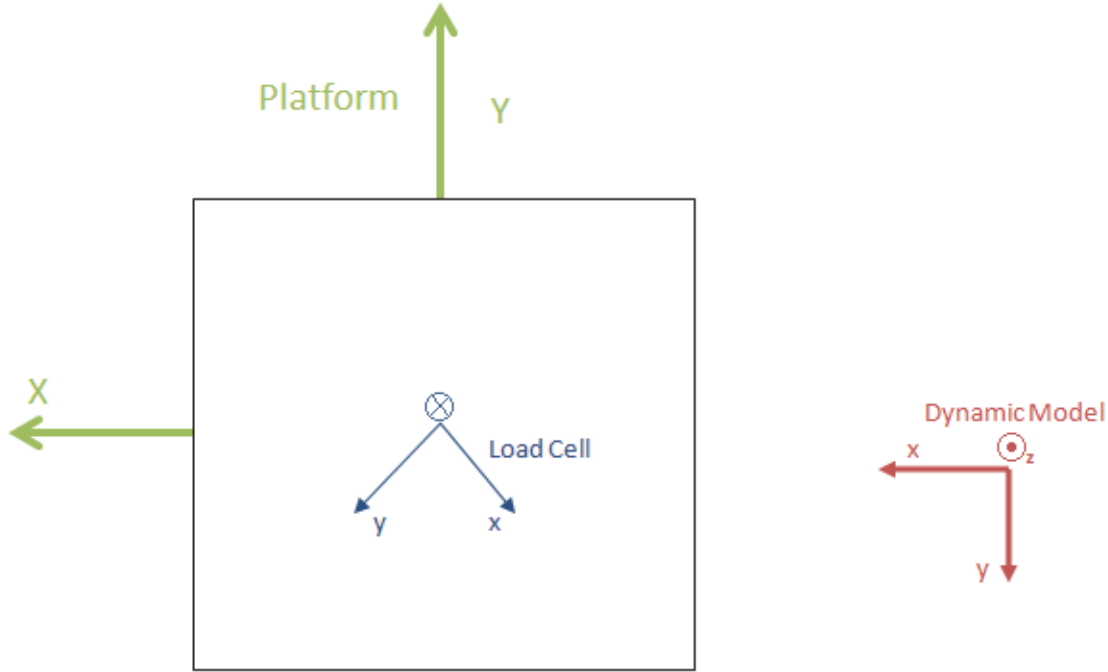


Figure 60: Coordinate systems for the experimental apparatus compared to the dynamic model.

$$\begin{bmatrix} T_{\text{LoadCell}}^{\text{DynamicModel}} \end{bmatrix} = \begin{bmatrix} \sin 45^\circ & \cos 45^\circ & 0 \\ \cos 45^\circ & -\sin 45^\circ & 0 \\ 0 & 0 & -1 \end{bmatrix} \quad (117)$$

Finally, the moments measured from the load cell had to be rotated to the dynamic model frame. Since the moment results from a cross product, the vector cannot be simply rotated from one coordinate frame to the other like a polar vector, so the moment was broken down into the force and position vectors and then rotated. Consider the example seen in Figure 61, it can be seen that a force and a moment experienced is equivalent if it was assumed that the force was being applied at a distance along the axis. From the measurements, the force magnitude was known, and therefore the distance along the axis was calculated.

$$|r_y| = \frac{|M_z|}{|F_x|} \quad (118)$$

The direction of the force vector is known to be along the x axis of the load cell

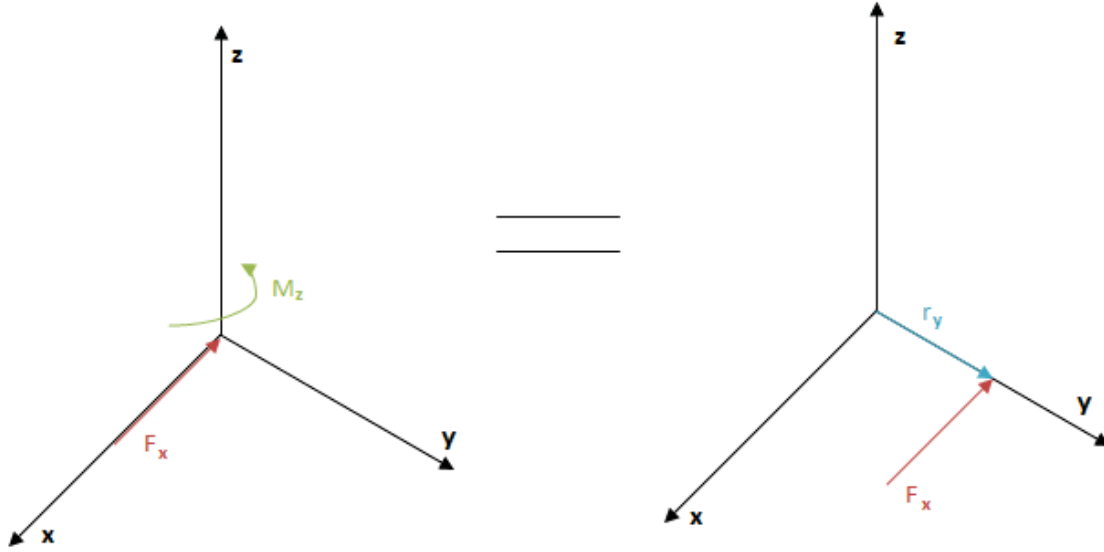


Figure 61: Example of breaking moment into force and position vector components.

coordinate frame. The definition of a moment is the cross product of the position vector with the force vector. Assuming that the load cell coordinate frame is A and the dynamic model coordinate frame is B , the moment about the z axis is

$$\mathbf{M}_z^A = \mathbf{r}_y^A \times \mathbf{F}_x^A \quad (119)$$

For the moment to be expressed in coordinate system B , the position and force vectors must be rotated

$$\mathbf{M}_z^B = R_B^A \mathbf{r}_y^A \times R_B^A \mathbf{F}_x^A \quad (120)$$

Using the expression in Equation 120 and the rotation matrix defined in Equation 117 the moments measured from the load cell were rotated in order to be compared to the result from the simulation.

The results for the Graham model simulation and experimental results for the general ship motion case can be seen in Figures 62 through 67. It can be seen from the graphs that the forces and moments calculated from the simulation are similar to those collected from the experimentation. The results for the inverted pendulum simulation and experimental results for the general ship motion case can be seen in Figures 68 through 70. Also from these results, the correlation between the simulated

results and the experimental results is high thus the inverted pendulum was validated through the experimentation.

5.5 Computational Validation of the Cart Load Model

The cart model is computationally validated by separating the translational and rotational degrees of freedom and validating them separately. The cart model is stabilized by adding a translational directed spring and damper element along the translational axis between the deck and cart; as well as a similar torsional directed element between the lower and upper cart bodies. The resulting stable model is validated by comparing the forced frequency responses of the system to the theoretical responses.

Adding the spring and damper for the translating body added external forces being applied to the body. This required the modification of Equation 81 with the addition of the spring and damper forces resulting in

$$\sum \mathbf{F}_B^{IN} = \mathbf{F}_{BR}^{IN} - \mathbf{F}_{TR}^{IN} - m_1 \mathbf{g}^{IN} + c \mathbf{v}_{B/A}^{MO} + k \mathbf{r}_{B/A}^{MO} \quad (121)$$

This modification is carried through the equations presented previously in Section 4 and the resulting translational governing equation was found.

The physical parameters for validating this model are given in Table 4. These values do not have to be compared to any physical apparatus, thus the values were chosen for ease of use. The simulation was run for three different damping ratios. For each damping ratio the simulation was run for five frequencies. The frequencies were selected to be close to the natural frequency in order to see the increase in amplitude as well as the expected change of phase above the system natural frequency.

A similar method was used in order to validate the rotational degree of freedom of the model. This method stabilized the rotational degree of freedom by adding a torsional spring and damper. This resulted in an added external moment to Equation 106. The simulation was run for three different damping ratios. For each damping ratio the simulation was run for five frequencies. The frequencies were selected to be close to the natural frequency in order to see the increase in amplitude as well as the expected change of phase above the system natural frequency.

The calculated frequencies and amplitudes were compared to the expected results from the solution of an analogous single degree-of-freedom spring damper system. The translational results have been tabulated in Tables 5 through 7. The rotational results have been tabulated in Tables 8 through 10. Comparing the simulation results

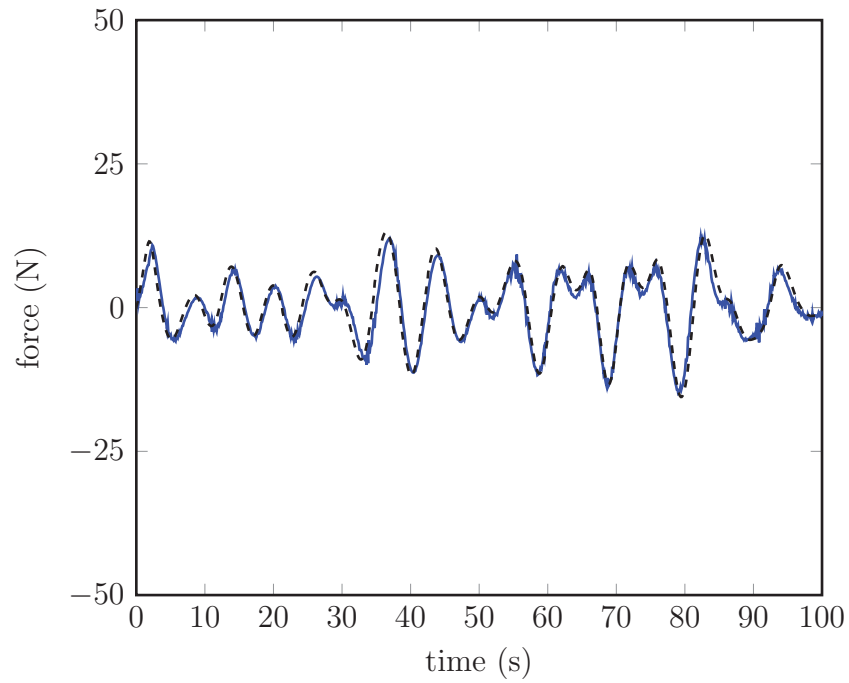


Figure 62: Longitudinal force (F_x) computed using GRM3D (solid) and the load cell results from the experimentation (dashed).

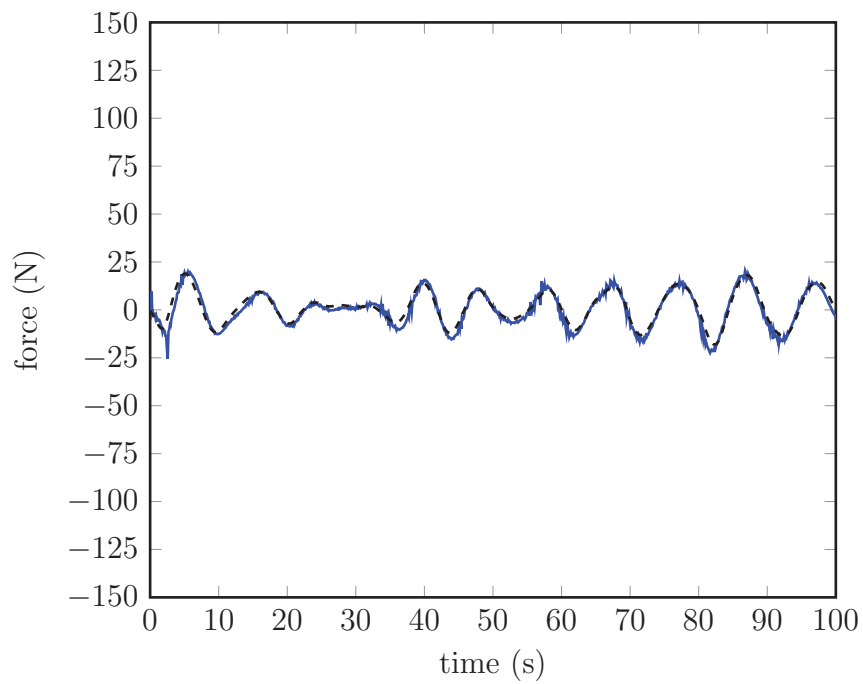


Figure 63: Lateral force (F_y) computed using GRM3D (solid) and the load cell results from the experimentation (dashed).

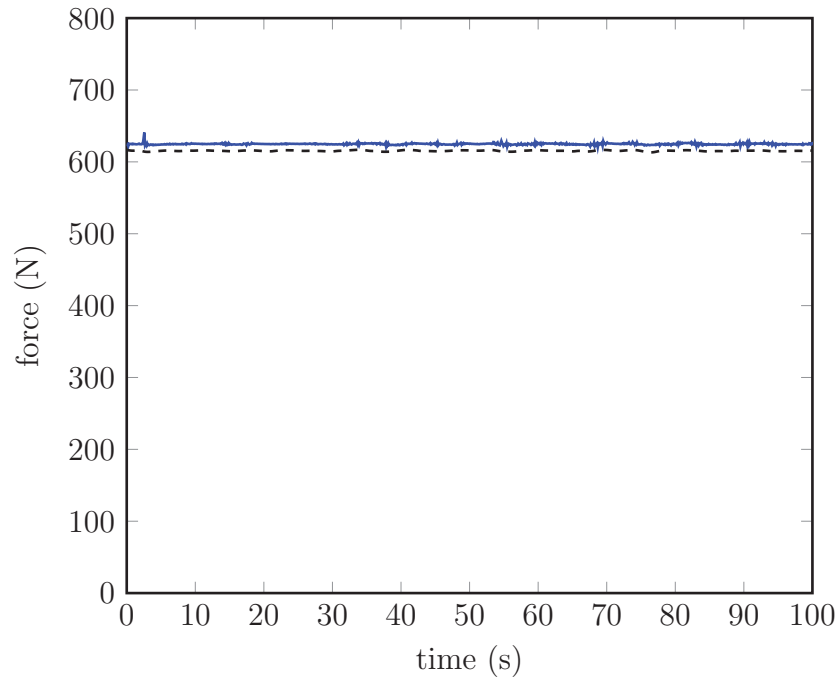


Figure 64: Vertical force (F_z) computed using GRM3D (solid) and the load cell results from the experimentation (dashed).

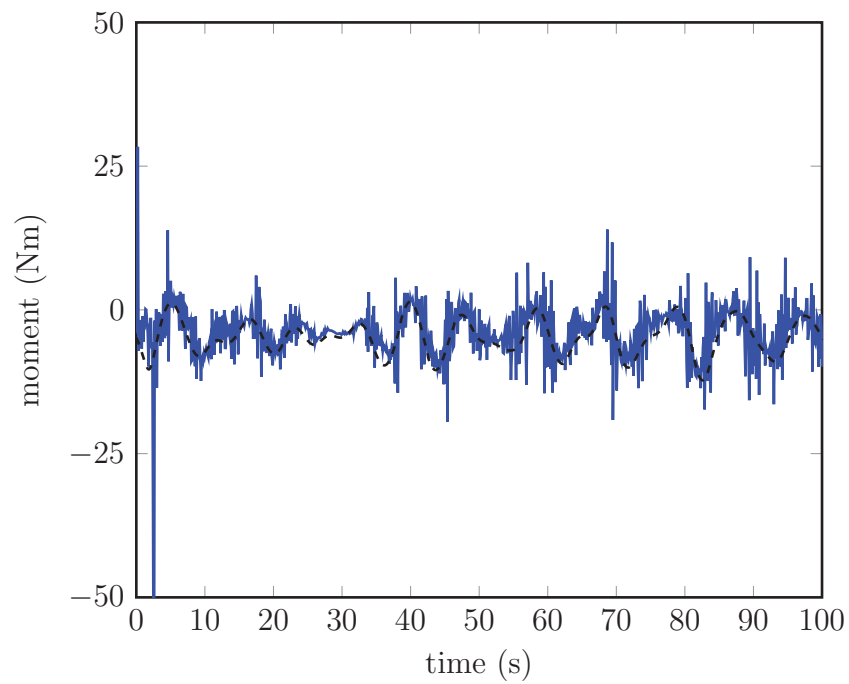


Figure 65: Longitudinal moment (M_x) computed using GRM3D (solid) and the load cell results from the experimentation (dashed).

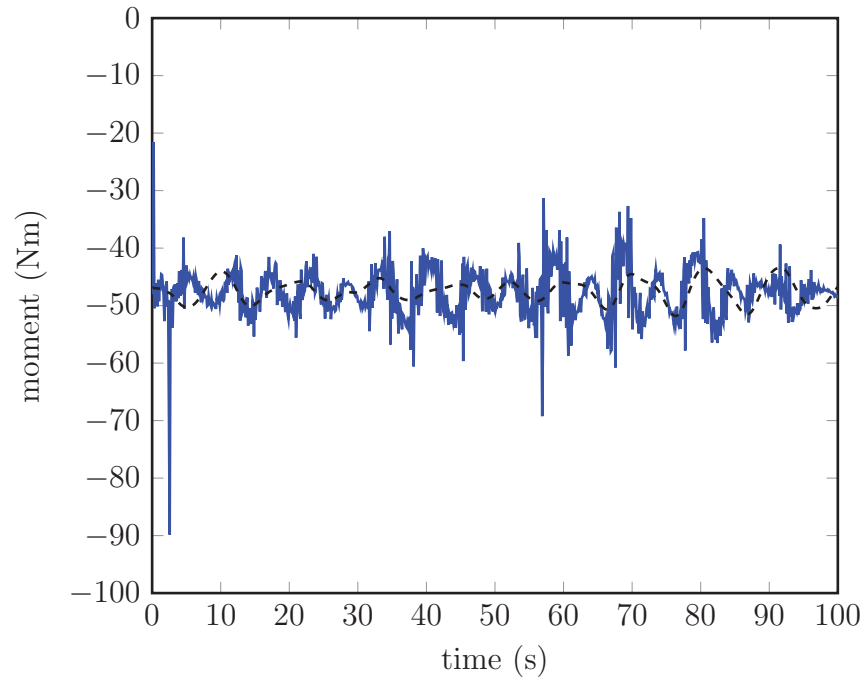


Figure 66: Lateral moment (M_y) computed using GRM3D (solid) and the load cell results from the experimentation (dashed).

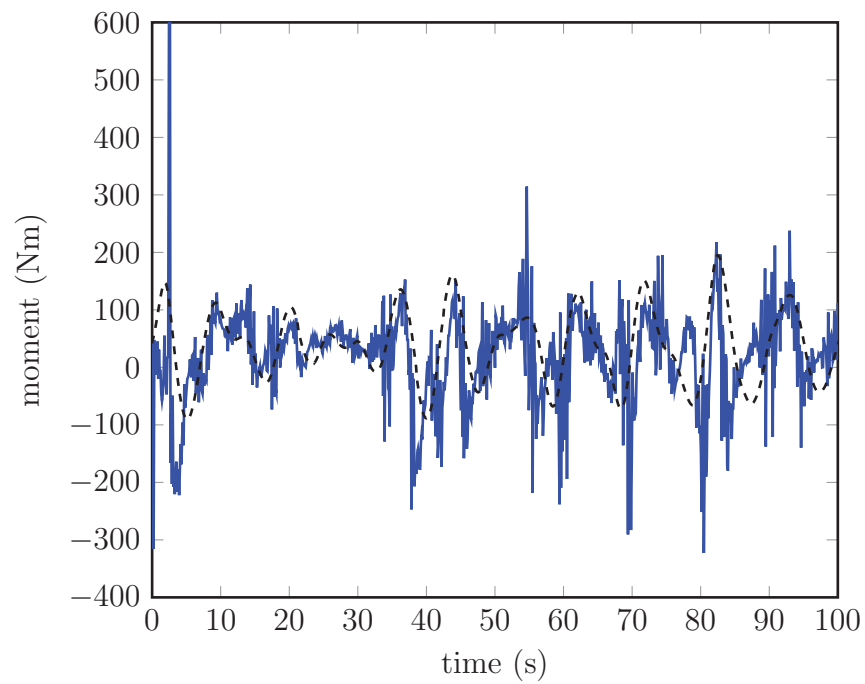


Figure 67: Vertical moment (M_z) computed using GRM3D (solid) and the load cell results from the experimentation (dashed).

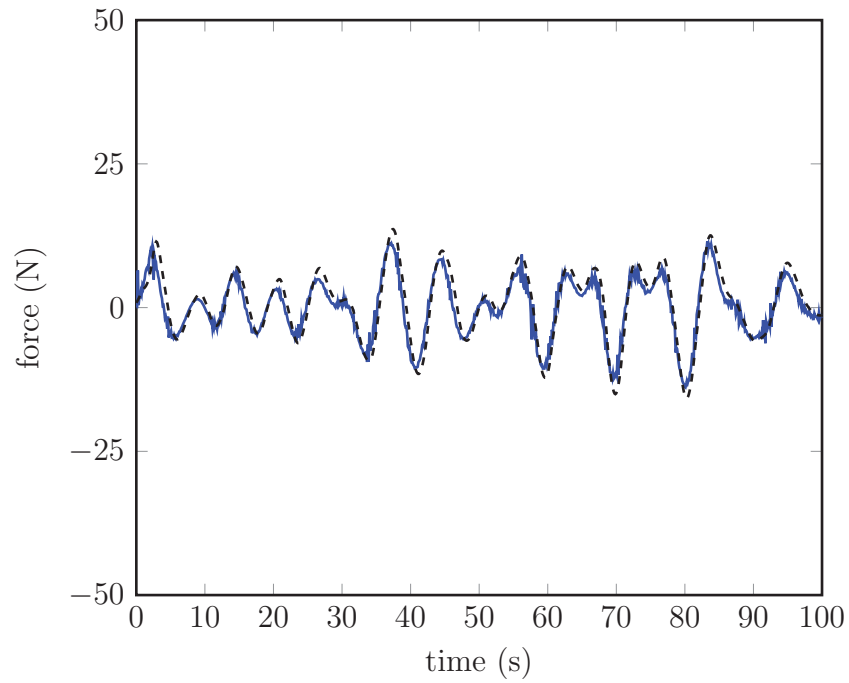


Figure 68: Longitudinal force (F_x) for computed using PSM3D (solid) and the load cell results from the experimentation (dashed).

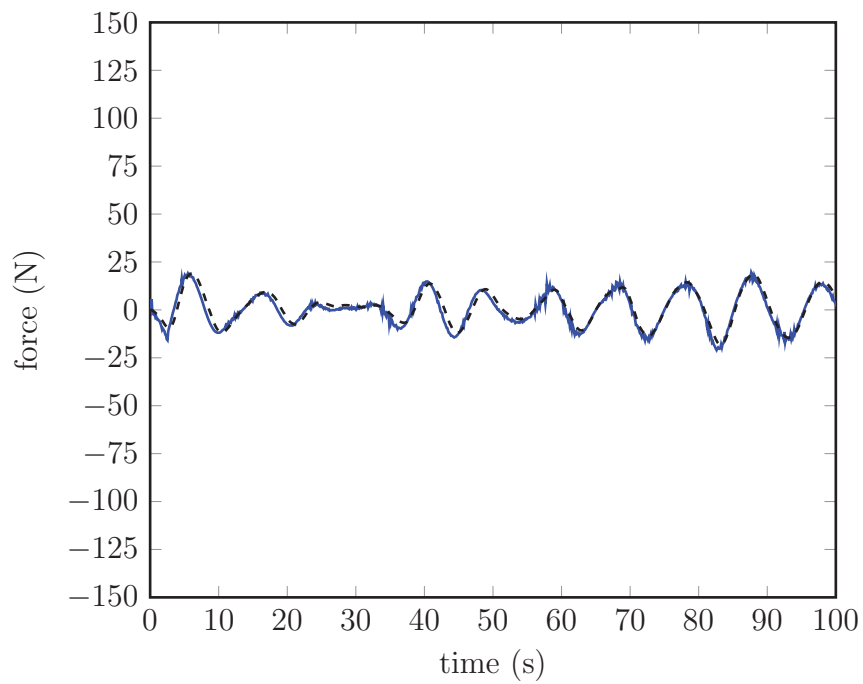


Figure 69: Lateral force (F_y) for computed using PSM3D (solid) and the load cell results from the experimentation (dashed).

Table 4: Simulation parameters used for CRT3D validation

Parameter	Value
m_1	78 kg
m_2	22 kg
I_{xx1}	10 kg m ²
I_{yy1}	10 kg m ²
I_{zz1}	1 kg m ²
I_{xx2}	10 kg m ²
I_{yy2}	10 kg m ²
I_{zz2}	1 kg m ²
$\mathbf{r}_{CG/A}^{MO}$	$\{0.0 \ 0.0 \ 0.9\}^T$ m
g	9.81 m/sec ²

Table 5: Results from translational forced frequency excitation on the cart for the case where $\zeta = 0.35$

$m = 20$ kg, $k = 1000$ N/m, $c = 100$ Ns/m, $f_n = 1.1$ rad/s, $\zeta = 0.35$				
Forced Freq. rad/s	Freq. Ratio Simulated	Freq. Ratio Calculated	Amp. Ratio Simulated	Amp. Ratio Calculated
0.8	0.77	0.73	1.27	1.3
1.0	0.86	0.91	1.22	1.2
1.4	1.24	1.27	0.95	1.0
1.8	1.58	1.64	0.55	0.60
2.2	1.97	2.00	0.34	0.35

to the expected theoretical values in the tables, the results are found to be similar and thus have validated the cart model.

As well as the constant frequency tests, a frequency sweep was performed to see the frequency response of the system over frequencies ranging from 0.1 rad/s to 3.0 rad/s. The frequency sweep was performed with a spring constant of 1000 N/m, a damping coefficient of 50 Ns/m, and a total cart mass of 20 kg in the translational direction. The resulting frequency response can be seen in Figure 71. It should be noted that at the natural frequency the amplitude multiplication factor should be approximately 2.8, which can be seen at the peak of the graph. A similar frequency sweep was performed for the rotational degree of freedom. For this test the forcing frequencies ranged from 0.1 rad/s to 3.0 rad/s with a spring constant of 1000 Nm/rad, a damping coefficient of 25 Nsm/rad, and a total cart moment of inertia of 20 kgm² in the rotational direction. The rotational frequency response can be seen in Figure 72. Again, the results are consistent with those expected.

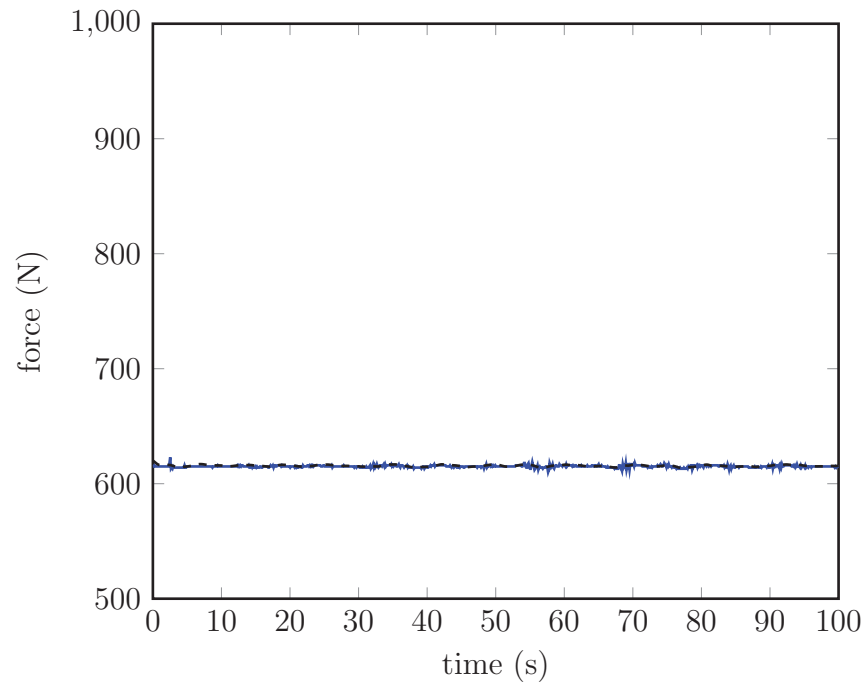


Figure 70: Vertical force (F_z) for computed using PSM3D (solid) and the load cell results from the experimentation (dashed).

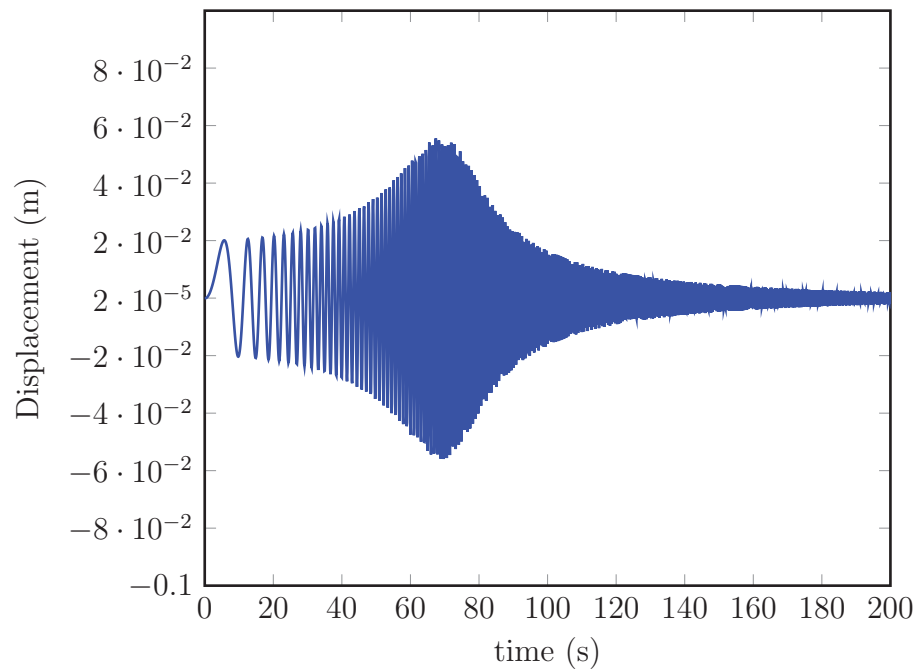


Figure 71: Frequency response for the cart model stabilized with a spring and damper in translation for the case where $\zeta = 0.17$.

Table 6: Results from translational forced frequency excitation on the cart for the case where $\zeta = 0.5$

$m = 20 \text{ kg}, k = 2000 \text{ N/m}, c = 200 \text{ Ns/m}, f_n = 1.6 \text{ rad/s}, \zeta = 0.5$				
Forced Freq. rad/s	Freq. Ratio Simulated	Freq. Ratio Calculated	Amp. Ratio Simulated	Amp. Ratio Calculated
0.8	0.47	0.50	1.14	1.1
1.0	0.65	0.63	1.24	1.2
1.4	0.90	0.88	1.22	1.25
1.8	1.05	1.13	0.92	0.90
2.2	1.29	1.38	0.61	0.65

Table 7: Results from translational forced frequency excitation on the cart for the case where $\zeta = 0.25$

$m = 20 \text{ kg}, k = 2000 \text{ N/m}, c = 100 \text{ Ns/m}, f_n = 1.6 \text{ rad/s}, \zeta = 0.25$				
Forced Freq. rad/s	Freq. Ratio Simulated	Freq. Ratio Calculated	Amp. Ratio Simulated	Amp. Ratio Calculated
0.8	0.51	0.50	1.26	1.25
1.0	0.62	0.63	1.62	1.55
1.4	0.85	0.88	1.97	2.00
1.8	1.14	1.13	1.87	1.90
2.2	1.32	1.38	1.22	1.25

Table 8: Results from rotational forced frequency excitation on the cart for the case where $\zeta = 0.35$

$I = 20 \text{ kgm}^2, k = 1000 \text{ Nm/rad}, c = 100 \text{ Nsm/rad}, f_n = 1.1 \text{ rad/s}, \zeta = 0.35$				
Forced Freq. rad/s	Freq. Ratio Simulated	Freq. Ratio Calculated	Amp. Ratio Simulated	Amp. Ratio Calculated
0.8	0.69	0.73	1.24	1.3
1.0	0.88	0.92	1.18	1.2
1.4	1.25	1.27	0.98	1.0
1.8	1.60	1.64	0.53	0.60
2.2	1.96	2.00	0.31	0.35

Table 9: Results from rotational forced frequency excitation on the cart for the case where $\zeta = 0.5$

$I = 20 \text{ kgm}^2, k = 2000 \text{ Nm/rad}, c = 200 \text{ Nsm/rad}, f_n = 1.6 \text{ rad/s}, \zeta = 0.5$				
Forced Freq. rad/s	Freq. Ratio Simulated	Freq. Ratio Calculated	Amp. Ratio Simulated	Amp. Ratio Calculated
0.8	0.53	0.50	1.15	1.1
1.0	0.64	0.63	1.22	1.2
1.4	0.92	0.88	1.27	1.25
1.8	1.14	1.13	0.88	0.90
2.2	1.39	1.38	0.60	0.65

Table 10: Results from rotational forced frequency excitation on the cart for the case where $\zeta = 0.25$

$I = 20 \text{ kgm}^2, k = 2000 \text{ Nm/rad}, c = 100 \text{ Nsm/rad}, f_n = 1.6 \text{ rad/s}, \zeta = 0.25$				
Forced Freq. rad/s	Freq. Ratio Simulated	Freq. Ratio Calculated	Amp. Ratio Simulated	Amp. Ratio Calculated
0.8	0.47	0.50	1.22	1.25
1.0	0.64	0.63	1.57	1.55
1.4	0.89	0.88	2.07	2.00
1.8	1.10	1.13	1.88	1.90
2.2	1.34	1.38	1.26	1.25

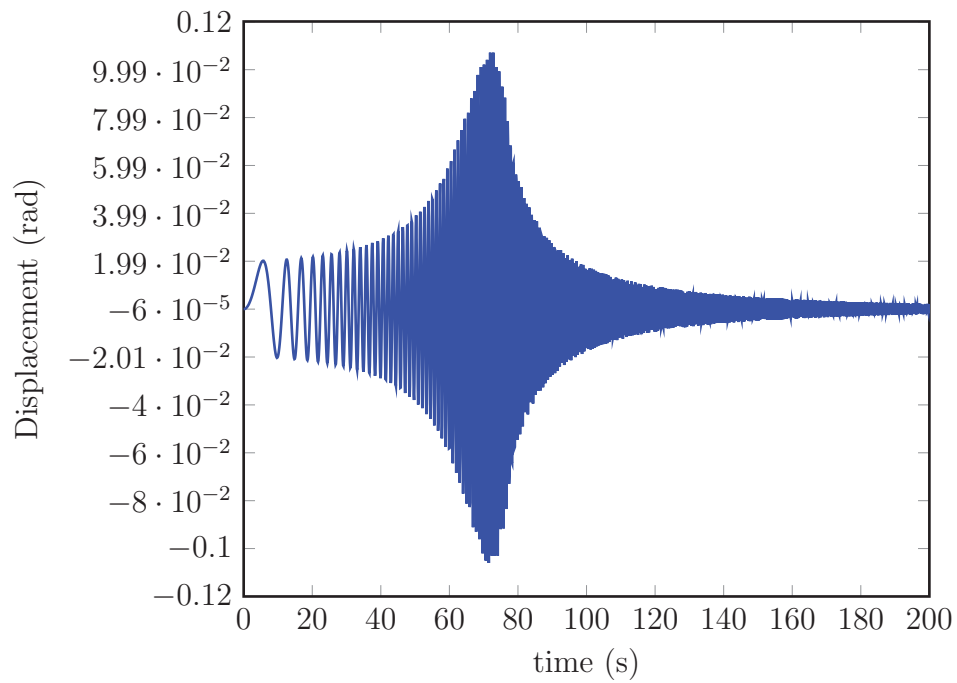


Figure 72: Frequency response for the cart model stabilized with a spring and damper in rotation for the case where $\zeta = 0.085$.

5.6 Validation of the Graham and Inverted Pendulum Stability Models Coupled to the Pendulum and Cart Loads through Experimentation

Once the validation of the individual models was completed, the models were coupled using the tension and compression link and therefore needed to be validated again in this coupled operating mode with the simulation results. The simulation model allowed for the coupling of the Graham model with either the pendulum or cart load models, resulting in two different configurations that needed to be validated. Both of the configurations were validated with the same input motions.

The parameters used for validating the coupled models were similar to those used to validate the models separately. The motion inputs used to validate the coupled models were linear sinusoidal sway motion with an amplitude of 0.1 m and a frequency of 0.5 rad/sec. A second motion profile was used to isolate an angular degree of freedom and was a constant frequency sinusoidal roll with an amplitude of 0.1 rad and a frequency of 0.5 rad/sec. To validate the model for all six degrees of freedom, ship motion was generated based on typical frigate and sea state data.

These coupled models were run for two different weights: 0 lbs (0 kg) and 70 lbs (31.75 kg), so that there were 1:1, 1:2, and 2:1 stability model to load model ratios. This allowed for more comprehensive validation using the different weights, which might have different effects on the physical models. Also, for the cart model, the point of rotation of the top mass could be altered, and two rotation configurations were investigated. The physical parameters used for the Graham model are the same as previously stated and provided in Table 3.

The results from the experimentation have been compared to the simulations. Sample results can be seen in Figures 73 through 78 that correspond to the general ship motion case with no additional mass plates on the Graham stability model and two mass plates on the pendulum load model. Figures 79 through 84 correspond to the general motion case with no additional mass plates on the Graham stability model and no mass plates on the cart load model. Figures 85 through 87 correspond to the sinusoidal motion case with no additional mass plates on the inverted pendulum stability model and two mass plates on the pendulum load model. The experimental data have been filtered using a fourth-order two-pass Butterworth filter to remove high frequency noise. The simulation data has been transformed from the experimental to the simulation coordinate frame using the method presented in the previous section. The results from both the simulation and experimentation are similar. The results show that the coupled models have been validated for the general ship motion case. The results for the longitudinal and lateral forces with the pendulum load attached showed variations from the experimental trends. This may be due to an error caused

by the rotation from the experimental to simulation frames. Also, the case with the cart load attached the results from the simulation for the lateral moment showed variations from the experimental trends.

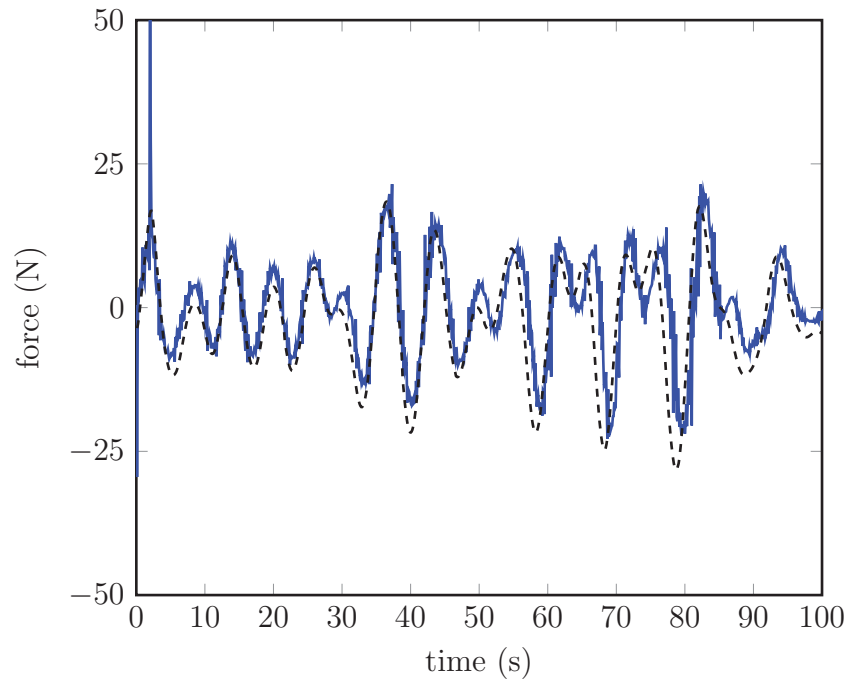


Figure 73: Longitudinal force (F_x) computed using GRM3D (solid) coupled to pendulum load and the load cell results from the experimentation (dashed).

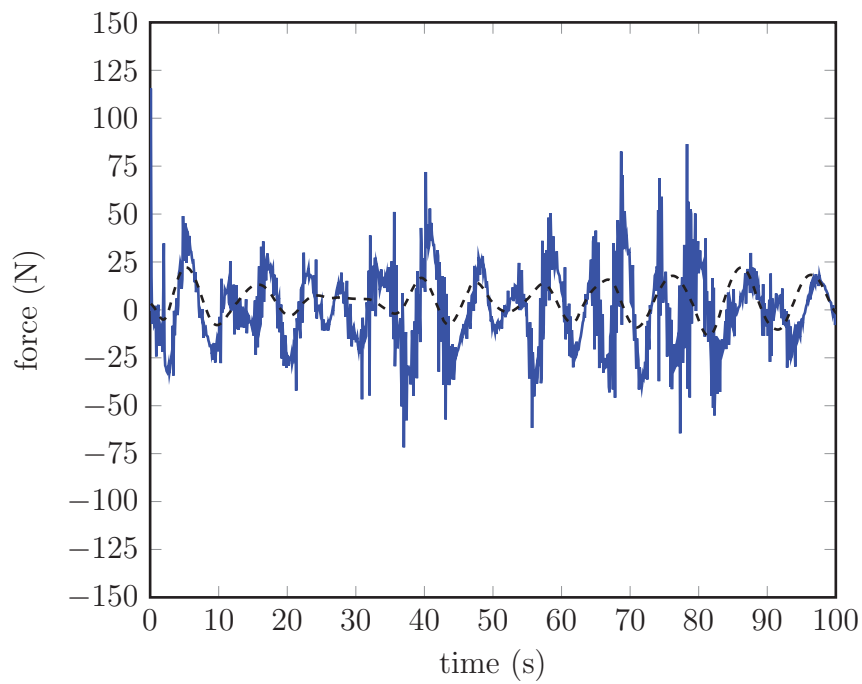


Figure 74: Lateral force (F_y) computed using GRM3D (solid) coupled to the pendulum load and the load cell results from the experimentation (dashed).

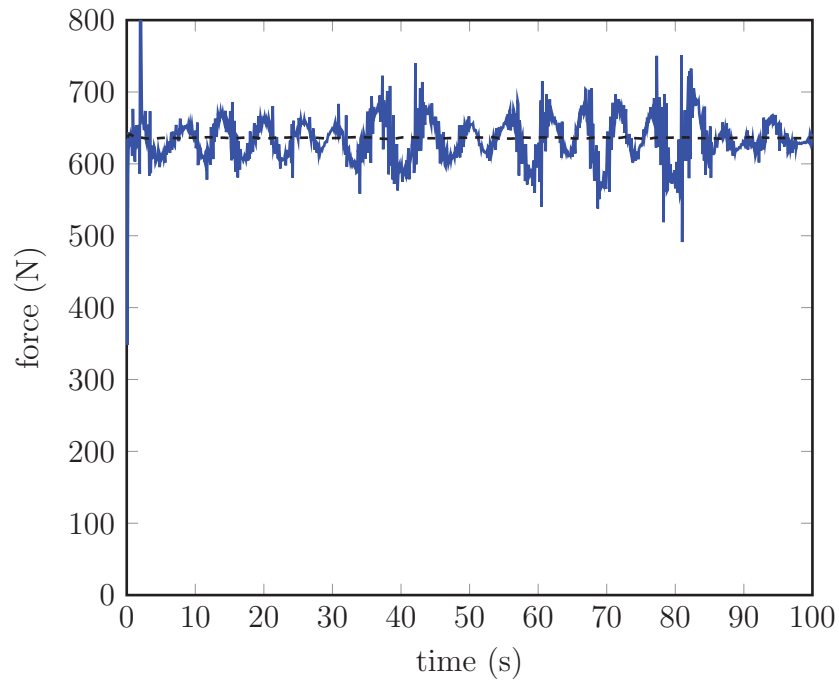


Figure 75: Vertical force (F_z) computed using GRM3D (solid) coupled to pendulum load and the load cell results from the experimentation (dashed).

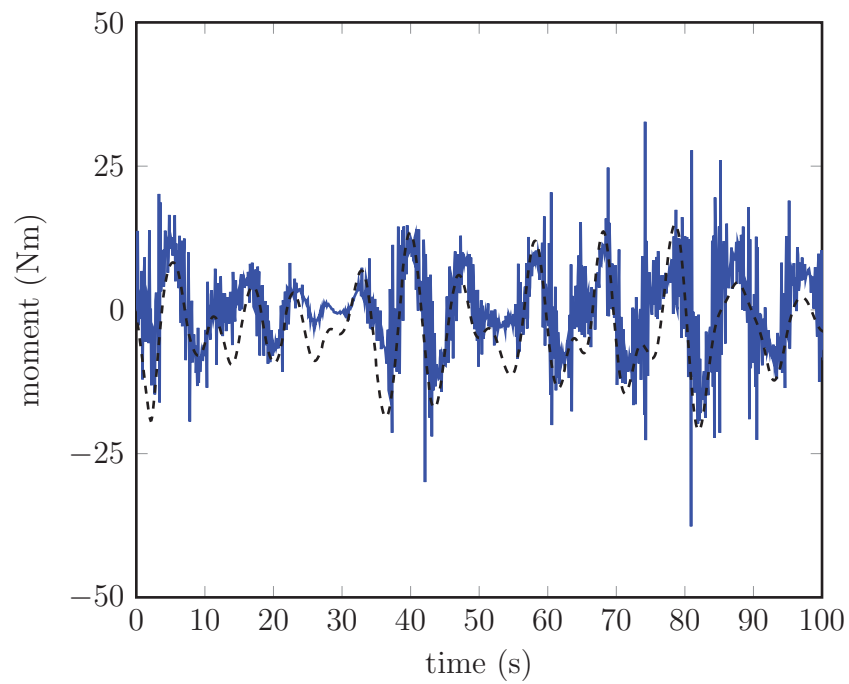


Figure 76: Longitudinal moment (M_x) computed using GRM3D (solid) coupled to pendulum load and the load cell results from the experimentation (dashed).

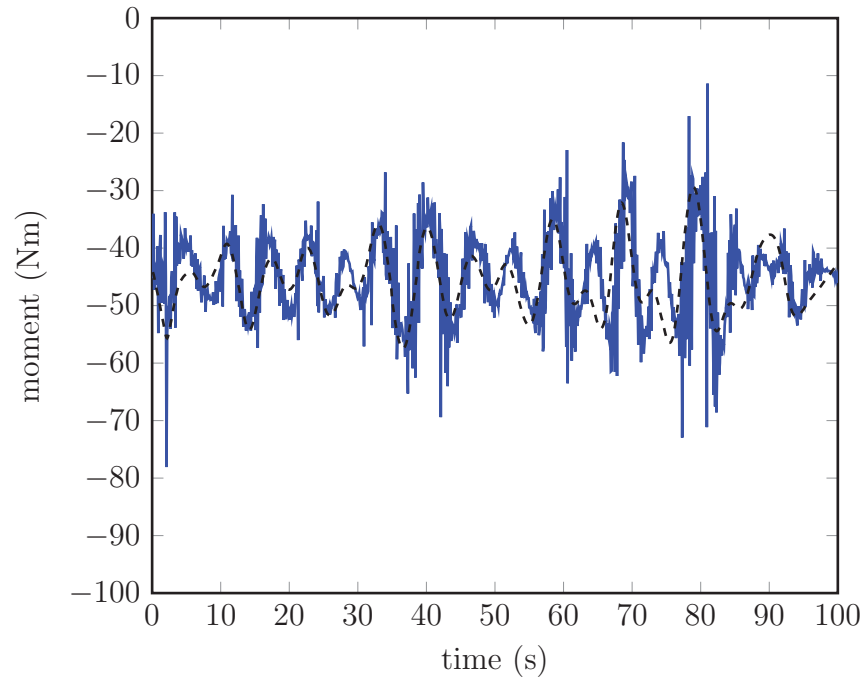


Figure 77: Lateral moment (M_y) computed using GRM3D (solid) coupled to pendulum load and the load cell results from the experimentation (dashed).

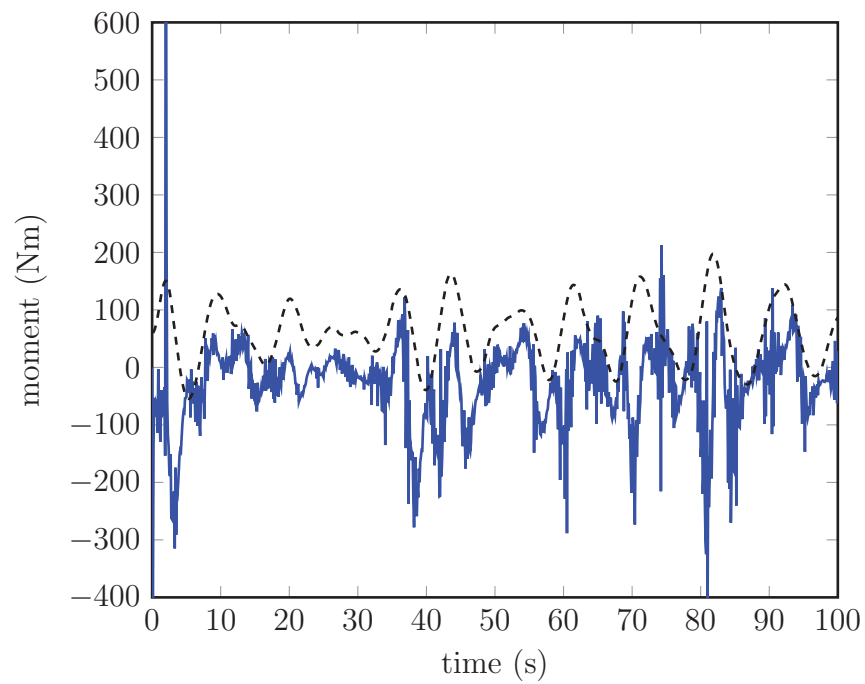


Figure 78: Vertical moment (M_z) computed using GRM3D (solid) couple to pendulum load and the load cell results from the experimentation (dashed).

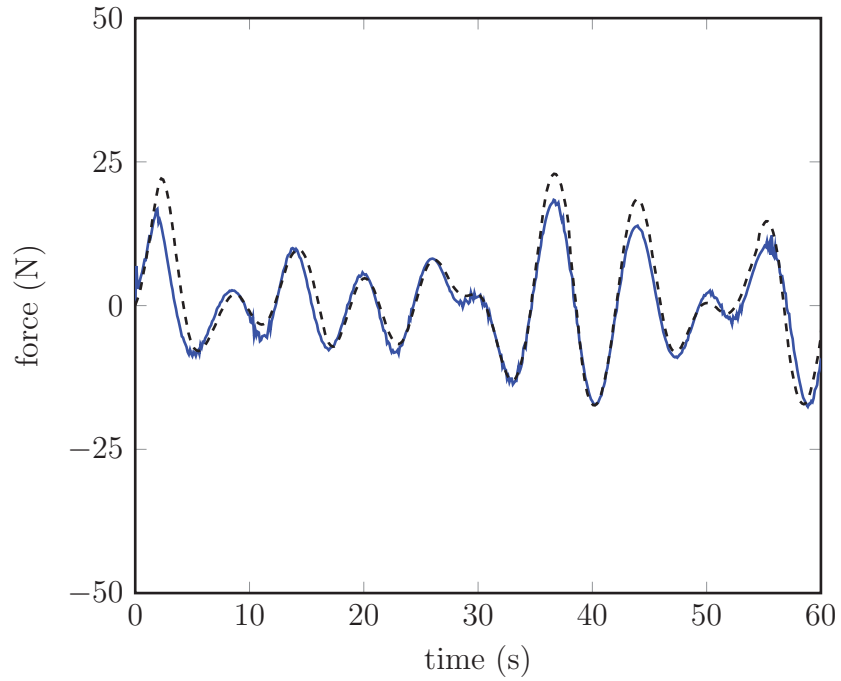


Figure 79: Longitudinal force (F_x) computed using coupled GRM3D (solid) coupled to cart load and the load cell results from the experimentation (dashed).

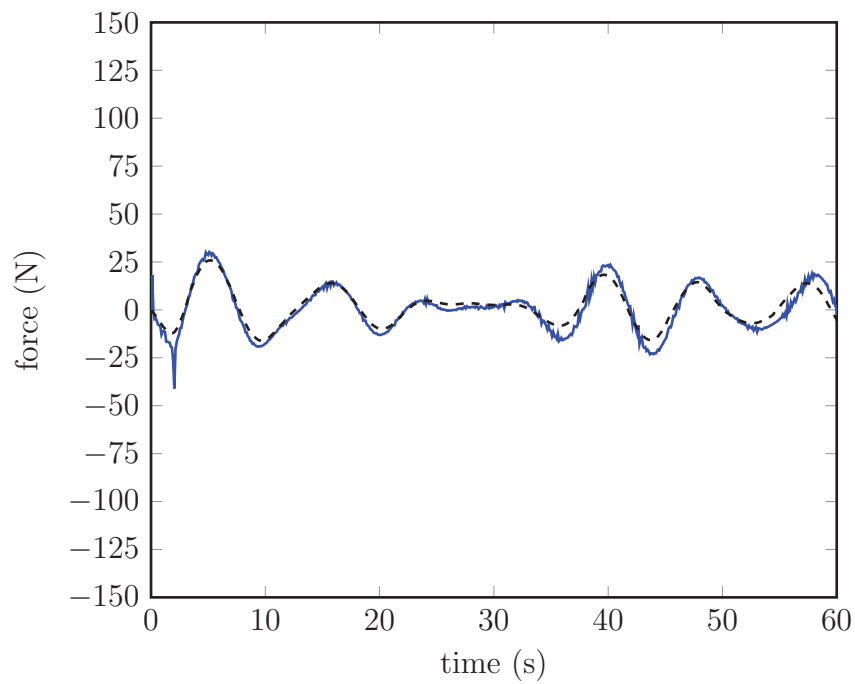


Figure 80: Lateral force (F_y) computed using coupled GRM3D (solid) coupled to cart load and the load cell results from the experimentation (dashed).

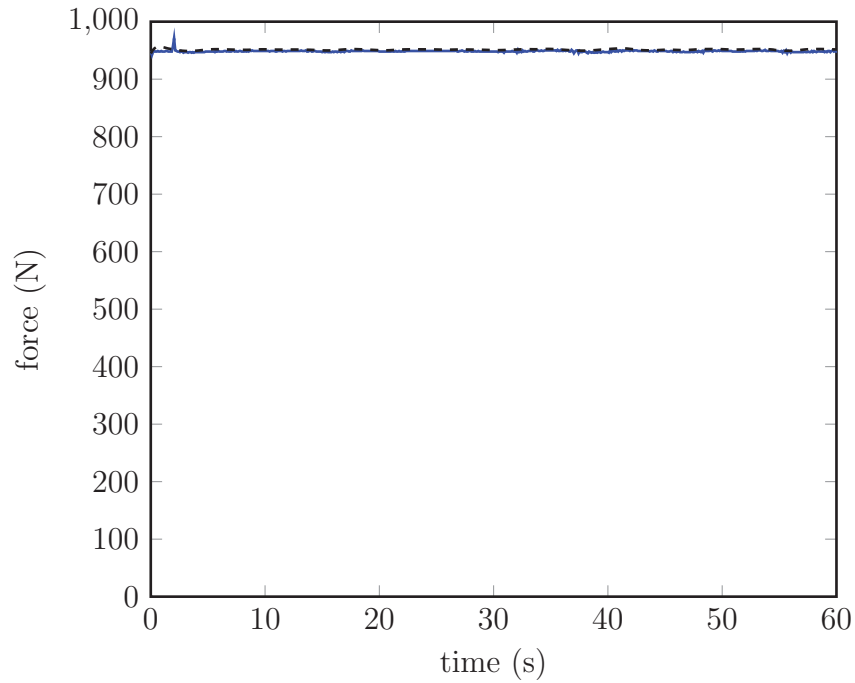


Figure 81: Vertical force (F_z) computed using coupled GRM3D (solid) coupled to cart load and the load cell results from the experimentation (dashed).

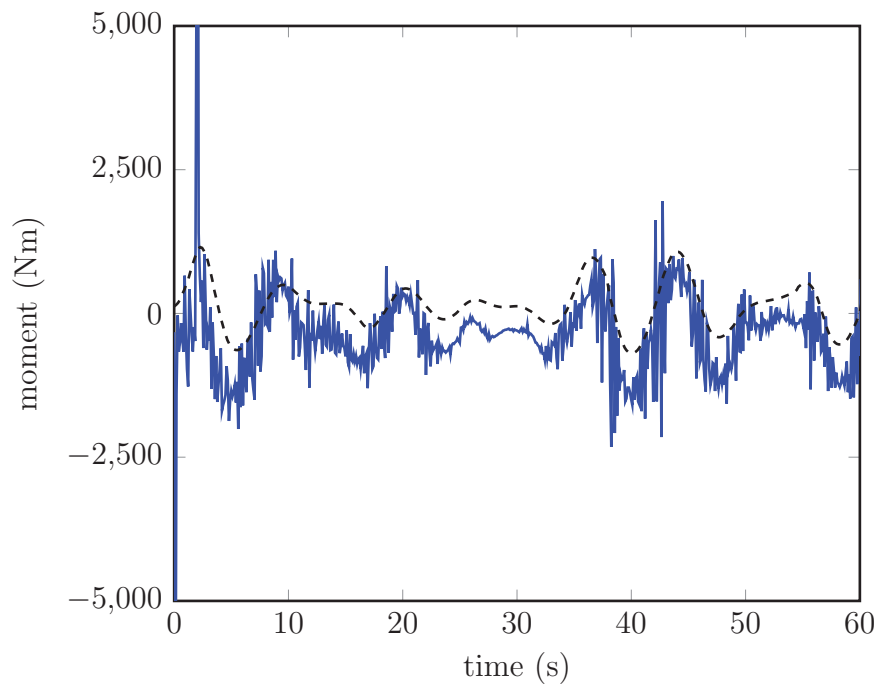


Figure 82: Longitudinal moment (M_x) computed using coupled GRM3D (solid) coupled to cart load and the load cell results from the experimentation (dashed).

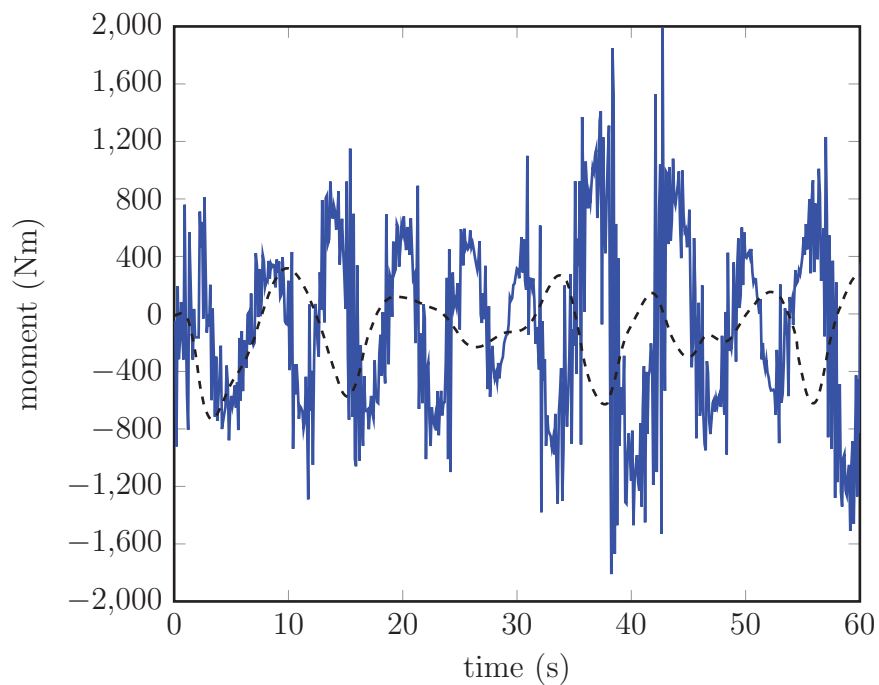


Figure 83: Lateral moment (M_y) computed using coupled GRM3D (solid) coupled to cart load and the load cell results from the experimentation (dashed).

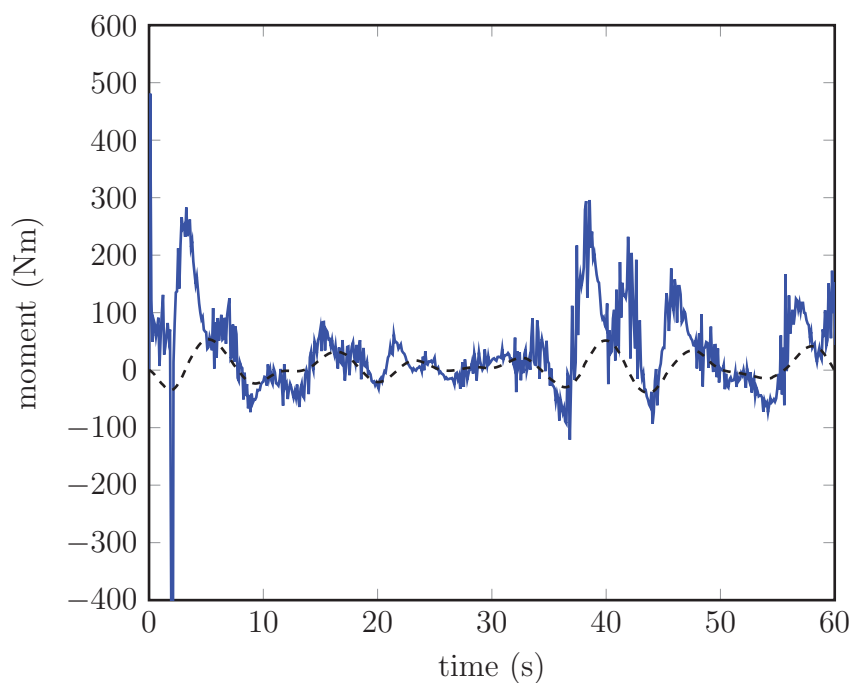


Figure 84: Vertical moment (M_z) computed using coupled GRM3D (solid) coupled to cart load and the load cell results from the experimentation (dashed).

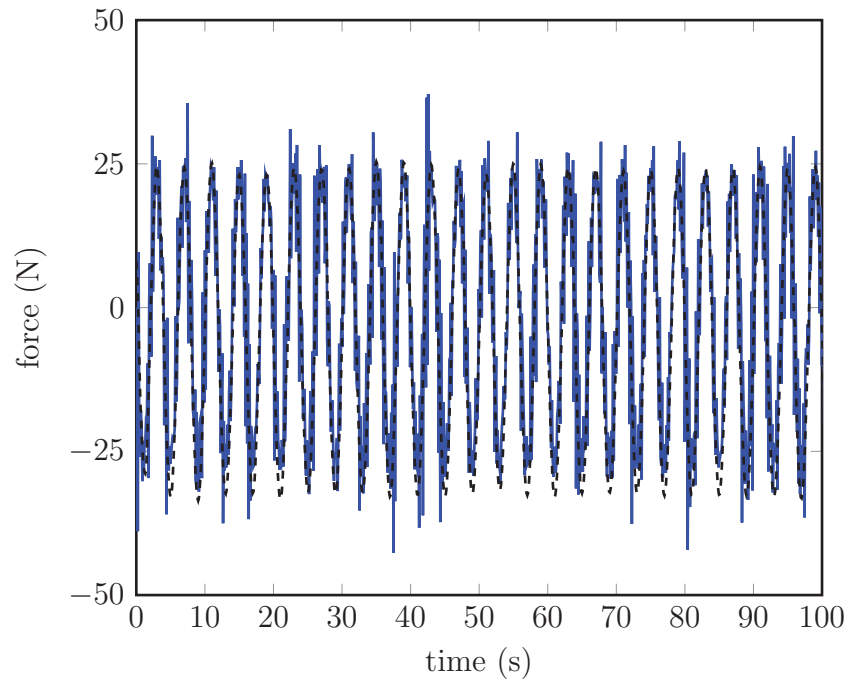


Figure 85: Longitudinal force (F_x) for computed using PSM3D (solid) and the load cell results from the experimentation (dashed).

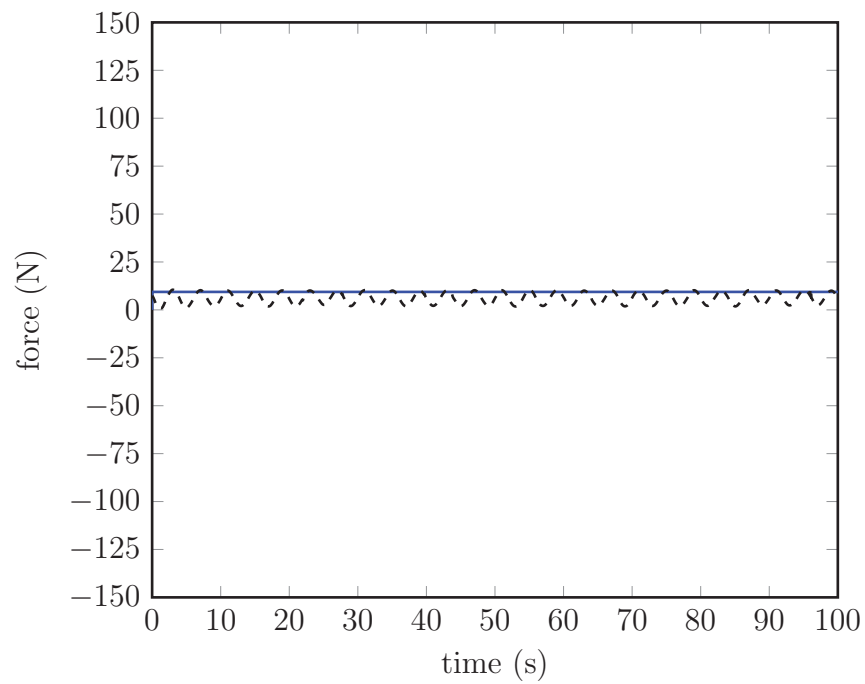


Figure 86: Longitudinal force (F_y) for computed using PSM3D (solid) and the load cell results from the experimentation (dashed).

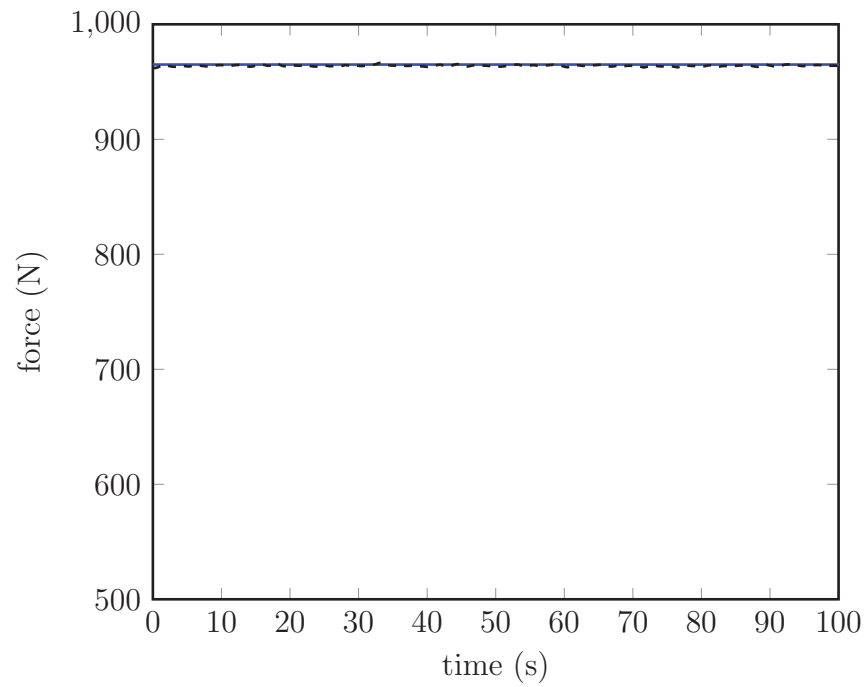


Figure 87: Vertical force (F_z) for computed using PSM3D (solid) and the load cell results from the experimentation (dashed).

6 Implementation and Verification of Federate Form

6.1 Development Environment

The solution of the mathematical models are implemented in two simulation environments. The first environment is a Fortran self-constrained simulation. The second is a distributed simulation environment running separate executables for each of the different models. The next section will explain the Fortran simulation environment.

The solutions for the dynamic systems for the stability and load models have been implemented in a Fortran function. The function solves the system of equations for the unknowns and then solves for the stability indices if required. The simulation is then controlled by a function that will call the required stability and load model functions for the simulation. The main function is compiled with the stability and load model functions and is called the Development Environment for Postural Stability Models (DEPSM). Each function has a required input file and will be discussed.

There are also required inputs for the DEPSM simulation. These inputs are all provided within a text file named `depsm.inp`. This input provides data on the length of the simulation, the incremental time step, type of motion selected, as well as the selection of which stability and load models will be used in the simulation. The length of the simulation and the time step are defined for the DEPSM function, and passed to the stability and load model functions. This environment allows for several different excitation motions. There is a sea motion based on the sea state and heading, prescribed motions from an input file, as well as no motion at all. These motions are provided to the stability and load functions and are defined about the centre of mass of the ship. These motions are converted in the stability or load model functions to the attachment point of the model on the deck. There is also the ability to select the required stability and load models for simulation. This was added for the ease of the user so that the DEPSM executable does not need to be recompiled for every stability to load model combination. Instead, it is just a selection in the input file.

As mentioned, each of the stability and load models have been implemented in a separate Fortran function. Each function solves the system of equations for that model. For the Graham model, Equations 52 and 91 are solved directly. The solution is propagated just using the equations of motion. However, for the inverted pendulum there needs to be a controller in order for the pendulum to remain upright. Also, for the solution the angular positions and velocities need to be known. These angles are found by integrating the angular acceleration using a fourth-order Runge-Kutta integrator. It was previously mentioned that the ship motion provided is the motion

of the centre of mass of the ship. This motion is converted in the stability and load model functions to the attachment point of the ship. From these solutions, the reaction forces and moments can be found at the attachment point. From the reaction forces and moments, the stability indices can be calculated as described in Section 3.4. For the load models, the stability indices do not need to be calculated but they are included for completeness.

The input files for the stability and load models require information on their geometry. There are certain distances that need to be known. For example, the position of the centre of mass compared to the attachment point a is needed for the Graham model. For the cart model there are additional lengths needed, such as the distance from the centre of mass m_1 to the rotation centre of mass m_2 , as well as the vector from the centre of mass m_2 to the location of the applied external force. Additional information required for the inverted pendulum includes the controller gains for the ankle torques. These can vary the results significantly and should be selected with care. One of the important input parameters for all the models is the placement on the ship deck. This could be defined as anywhere relative to the centre of mass location. An annotated sample input file is provided in Annex C.

The applied external forces on the models are based on their interaction with the other model to which they are coupled, and are calculated using the interface force model. This model has also been implemented in a Fortran function. The interface force can be limited to a prescribed level of force. This means that the force will not become excessive. As well, there are options available to not include the interface force at all, or to constrain it to be in tension only.

A visualization of the flow of the DEPSM simulation can be seen in Figure 88.

6.1.1 VFD-RT Environment

The Virtual Flight Deck - Real Time, VFD-RT, is a simulation environment originally developed in the Carleton University Applied Dynamics Laboratory by Kin Tsui. The motivation for developing this simulation environment was to make programming of a distributed simulation easy for new users, particularly where multiple stand-alone models must be combined and/or where compatibility with the structure of HLA-based simulation architectures is required. The full development of the software is presented in Reference [90]. The next section will provide a brief overview of the software followed by the implementation of the stability and load models in this simulation infrastructure.

The VFD-RT is a distributed simulation environment for simulation of maritime systems. This framework is similar to the comprehensive HLA simulation framework. The VFD-RT uses a provider and client method of establishing communications. A

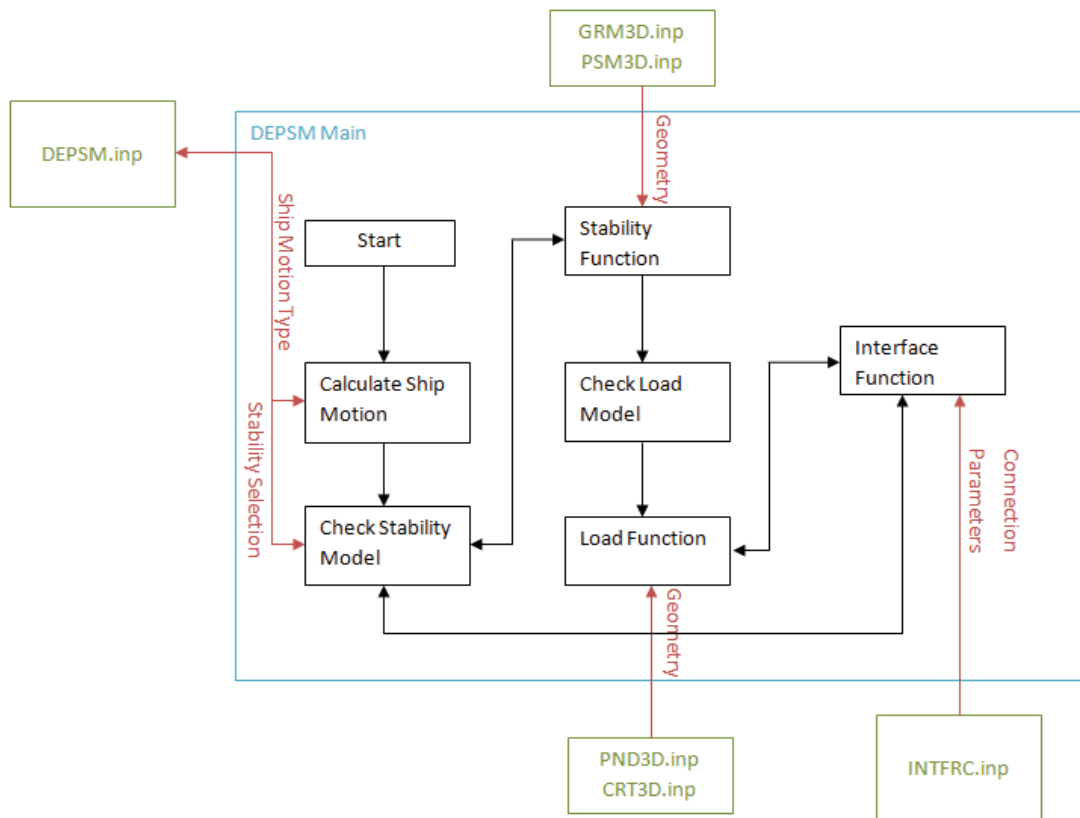


Figure 88: Visualization of DEPSM simulation environment and flow of solution.

provider is said to supply data for the other executables attached to the VFD-RT, whereas a client is said to take certain required data from the VFD-RT. In order to achieve communications between executables, they all must be connected to the VFD-RT. All connections and communication within the VFD-RT are done using the Windows communication protocols. For example, in order to connect to the main VFD-RT module, it searches for all registered windows running that have the VFD-RT id attached to them. Unlike the HLA, the executables attached to the VFD-RT do not need to be part of a federation, as well, the data sent between providers and clients does not need to follow a predefined class structure. This can be seen in Figure 89. The data transfer between executables attached to the VFD-RT have a limit on the data that can be passed. The data are transferred by copying the data to the windows clipboard, from which it is then picked up by the main VFD-RT program. The data size that is passed is an array with eighteen cells. This was selected by the developer based on the assumption that the larger data packages that would need to be passed in the simulation would be the ship motions for displacement, velocity, and acceleration. This was chosen in order to maintain simplicity for the user in creating new models. A unique identification number is provided to all executables as they are connected to the VFD-RT. This allows the source of data and the associated data format to be known. This also means that there is a requirement to know which executables will be needed for the simulation, and the order in which they will be connected to the VFD-RT.

Since the VFD-RT is a similar distributed simulation environment to the HLA architecture, the postural stability and load models are implemented in the VFD-RT framework. It has also been proven that a VFD-RT provider or client can quickly be converted into an HLA federate. Each of the stability models have been included as a VFD-RT provider/client application. A provider/client is both a provider and client at the same time. It is able to connect to the VFD-RT in such a way that allows it to both receive data from other clients and also to output data to the VFD-RT for use by other clients. A client is able to take data from two different provider sources. Figure 90 is the simulation diagram outlining data flow. The stability models require the ship motion input, which is provided from a ship motion provider, as well as the tension vector of the interface link. These models provide the position and velocity of the attachment points of the link that are required to calculate the interface force. The load models also receive the ship motion data and the tension vector applied to the link. They provide the location and velocity of the attachment point for subsequent calculation of the tension vector. The interface force model requires the data on the attachment points of each of the models, and provides the tension vector.

Each of the VFD-RT federates has the Fortran model linked to the executable. This is accomplished using Microsoft Visual Studio 2003, which applies a dynamic link to the object file. This ensures that the model being used is consistent between the DEPSM and VFD-RT simulations. They are both using the same subroutines to calculate the

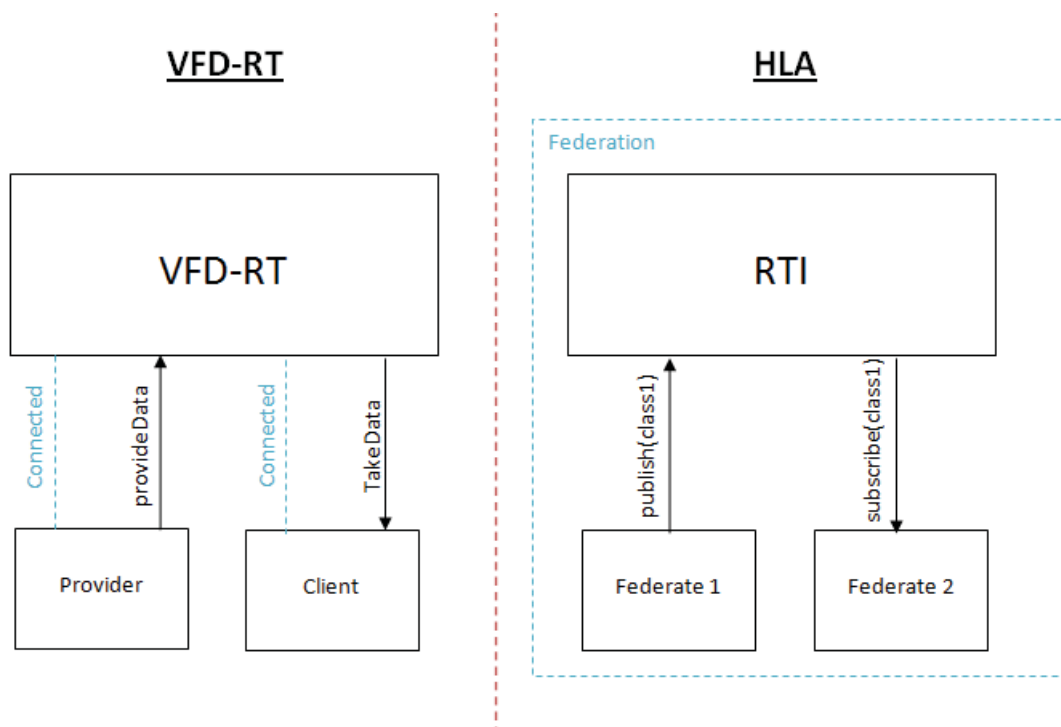


Figure 89: Connection and data transfer comparison between VFD-RT and HLA architectures.

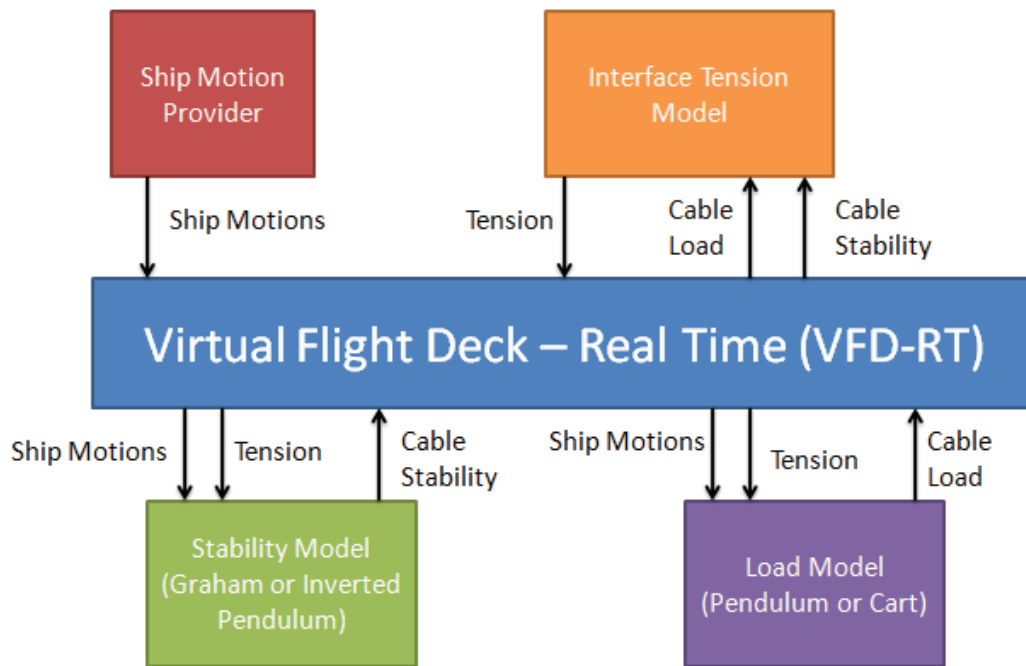


Figure 90: Connection and data transfer comparison between VFD-RT and HLA architectures.

motions and forces. This also provides a method of verifying the VFD-RT simulation with the DEPSM simulation.

6.2 VFD-RT Verification

Comparison of the two development environments, DEPSM and the VFD-RT, allows verification of the VFD-RT simulation using the DEPSM simulation. The verification will be performed using a general ship motion profile developed from sea state data.

In order for the ship motion to be provided to the VFD-RT, a previously developed and validated general motion provider is used.

There were several cases tested in order to verify the VFD-RT simulation environment. It was expected and required that all results be exactly the same value. This is because, as mentioned previously, the VFD-RT programs are using the same subroutines as the DEPSM simulation to calculate the model dynamics. This verification was intended to confirm mostly if communication between the executables is working correctly within the VFD-RT. The results obtained from testing the Graham model with the DEPSM environment and the VFD-RT environment can be seen in Figures 91 through 96. It can be seen that the results from the simulation running from the DEPSM environment and the VFD-RT environment are virtually identical (plotted traces are superimposed). Therefore, if either of the simulations are validated then both will have the same result and be valid.

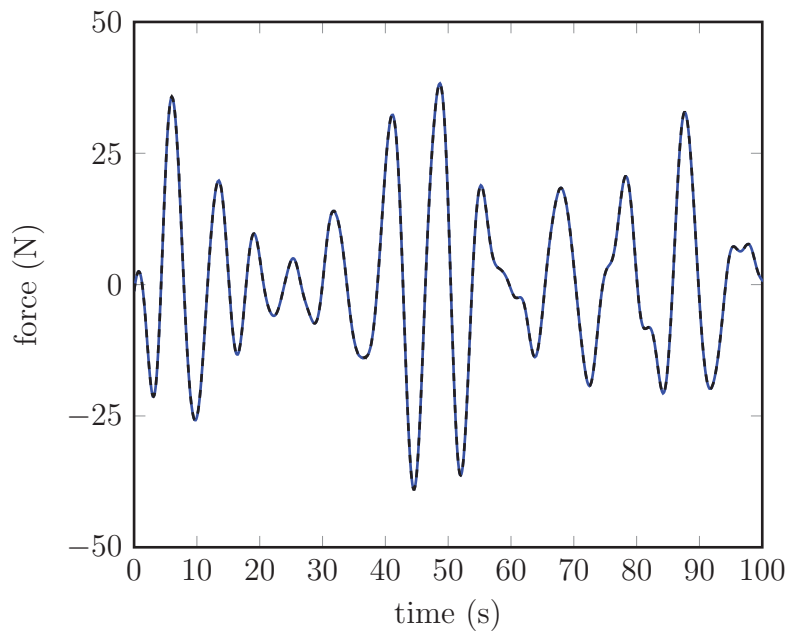


Figure 91: Longitudinal force (F_x) for computed using GRM3D from the VFD-RT (solid) and the DEPSM Simulation Environment (dashed).

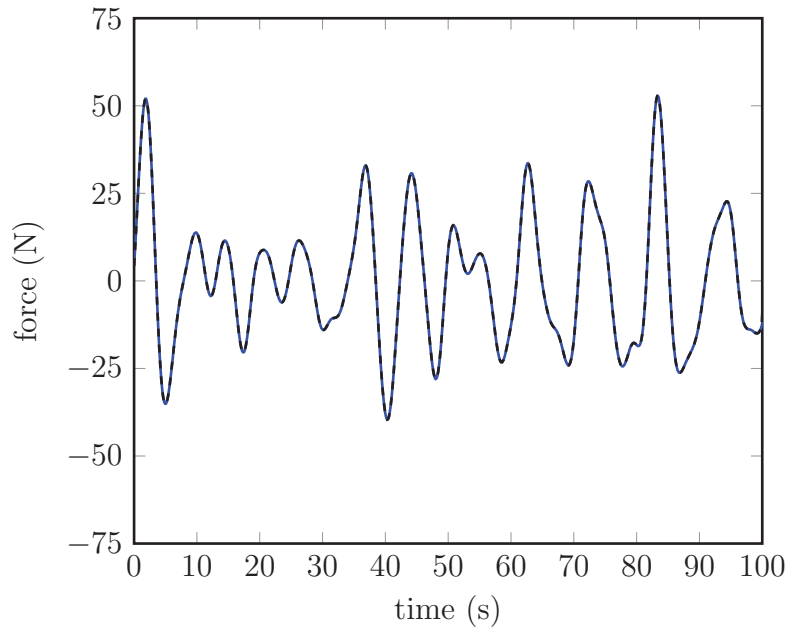


Figure 92: Longitudinal force (F_y) for computed using GRM3D from the VFD-RT (solid) and the DEPSM Simulation Environment (dashed).

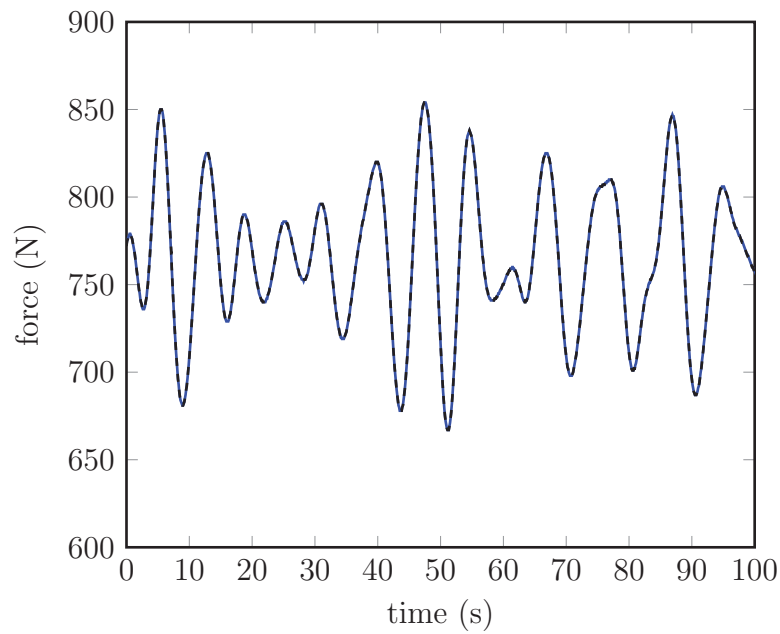


Figure 93: Vertical force (F_z) for computed using GRM3D from the VFD-RT (solid) and the DEPSM Simulation Environment (dashed).

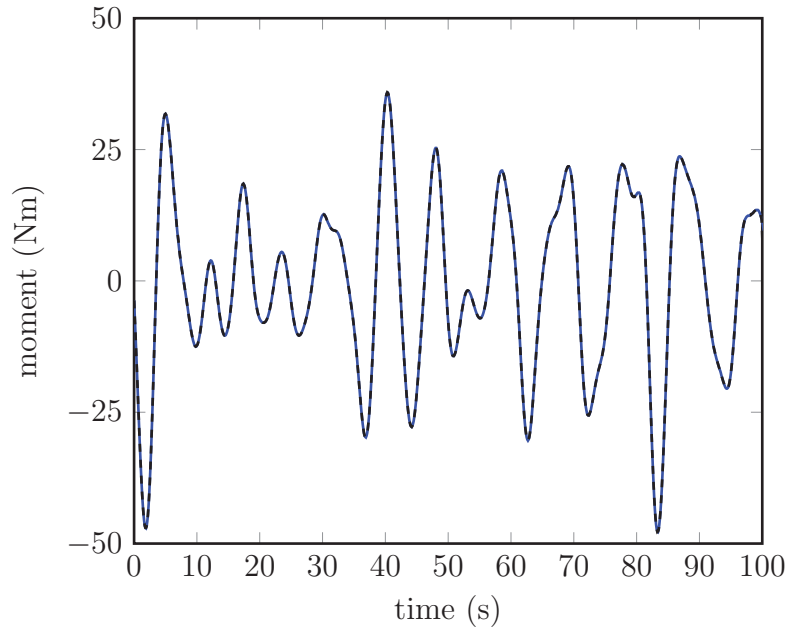


Figure 94: Reaction Moment (M_x) for computed using GRM3D from the VFD-RT (solid) and the DEPSM Simulation Environment (dashed).

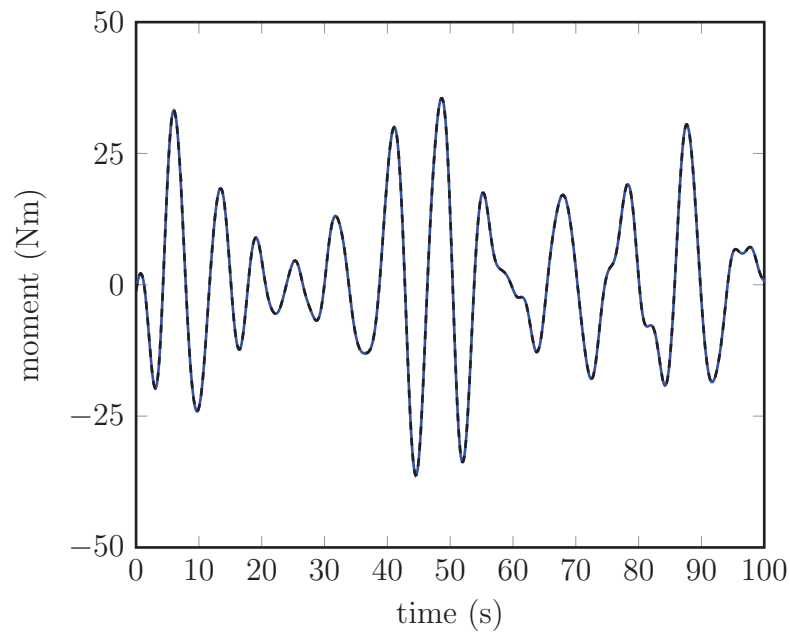


Figure 95: Reaction Moment (M_y) for computed using GRM3D from the VFD-RT (solid) and the DEPSM simulation environment (dashed).

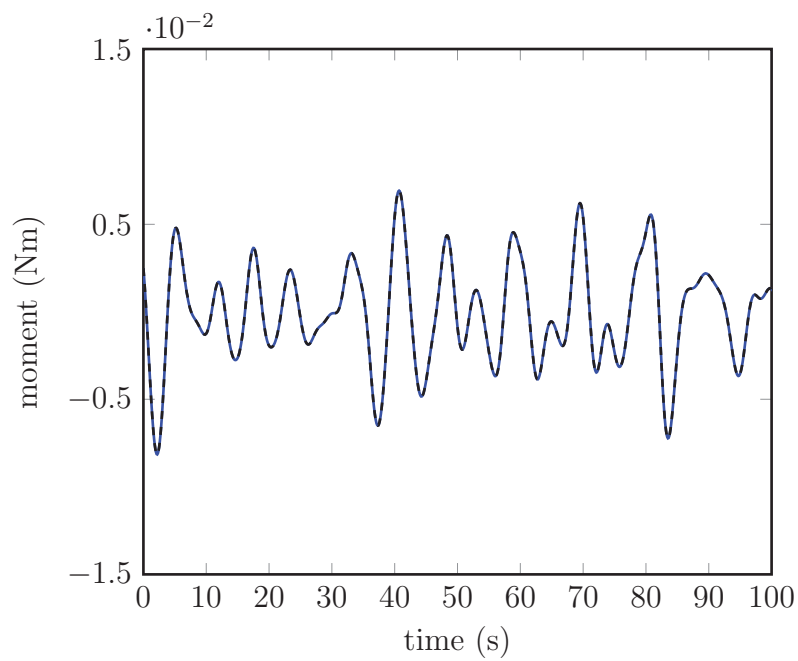


Figure 96: Reaction Moment (M_z) for computed using GRM3D from the VFD-RT (solid) and the DEPSM simulation environment (dashed).

7 Development of Model Tuning/Calibration Approach

7.1 Motivation

As part of this project, the Applied Dynamic Laboratory at Carleton University has developed complex models of human postural stability in shipboard environments. Recently, these models have been validated using mechanical experimental apparatuses. The final objective of these models is to be able to accurately predict human postural stability behaviour in moving environments. Therefore, the logical next step is to further tune and calibrate the models using human subjects in place of a mechanically-actuated inverted pendulum.

While the mechanical apparatus is excellent at providing experimental repeatability, it is limited in the range of control strategies that can be observed. This was especially obvious in the coupled pendulum experiment cases where there was very little movement and in the cart cases where there was too much movement.

An additional advantage of tuning the model with human subjects is that it is possible to record the instances of motion induced interruptions and relate them to the motions the subject was experiencing and the actions the subject was performing at the time of occurrence.

7.2 Equipment

The Applied Dynamics Laboratory has a variety of experimental equipment available for use in motion experiments with humans. The primary components that will be used are discussed below.

The 6DOF2000E MOOG Motion System is an electrically powered six degree of freedom Stewart platform. A diagram is shown in Figure 97. It contains its own power systems, servo-controls, safety monitors, overload protection, and computer interface for user interaction. Motion of the platform is attained through coordination of its six identical electro-mechanical actuators which incorporate high performance servomotors, bearings, low friction ball-screws, home/limit switches, and end of stroke cushioning.

The Tekscan F-Scan system uses instrumented shoe insoles to measure the pressure distribution applied to subjects' feet. A sample insole is shown in Figure 98. Pressure measurements are made by pressure sensitive ink that has an electrical resistance proportional to the compressive force applied to it. The insoles are typically trimmed to fit into a subject's footwear. The cable shown in the figure is connected to a nearby

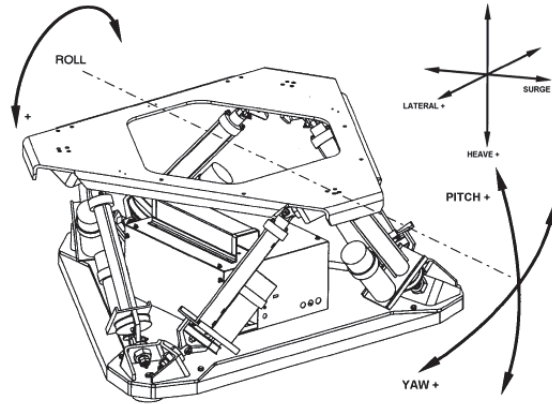


Figure 97: Moog 6DOF2000E motion system; available degrees of freedom [91].

computer via ethernet cables.

The OptiTrack camera system is a full body motion capture system. It uses up to thirty-four retro-reflective markers and eight infrared cameras to track the motion of a person or object in 3D space. In Figure 99 the four posts surrounding the motion platform hold the eight cameras.

Shown in Figure 100 is a six-axis load cell recently acquired by the Applied Dynamics Laboratory. It can measure forces up to ± 2500 N and torques up to ± 400 Nm. In the mechanical inverted pendulum experiment it was used to measure interface forces between the inverted pendulum and the motion platform. In experiments involving humans it could be used to measure forces under one of the subject's feet, or under a platform that the subject would be standing on. A single-axis load cell is also available for measuring interface forces between the human subject and the equipment with which they are physically interacting.

7.3 Safety

Subject safety is a primary consideration in the design of the proposed experiments due to the use of an electrically actuated motion platform, unsteady mechanical load models, and instrumentation apparatus that will be worn by the participants.

The 6DOF2000E MOOG Motion System possesses a number of safety features:

- Software limits, which restrict the maximum position, velocity, and acceleration that the platform may experience by monitoring and controlling the commands sent to the platform.

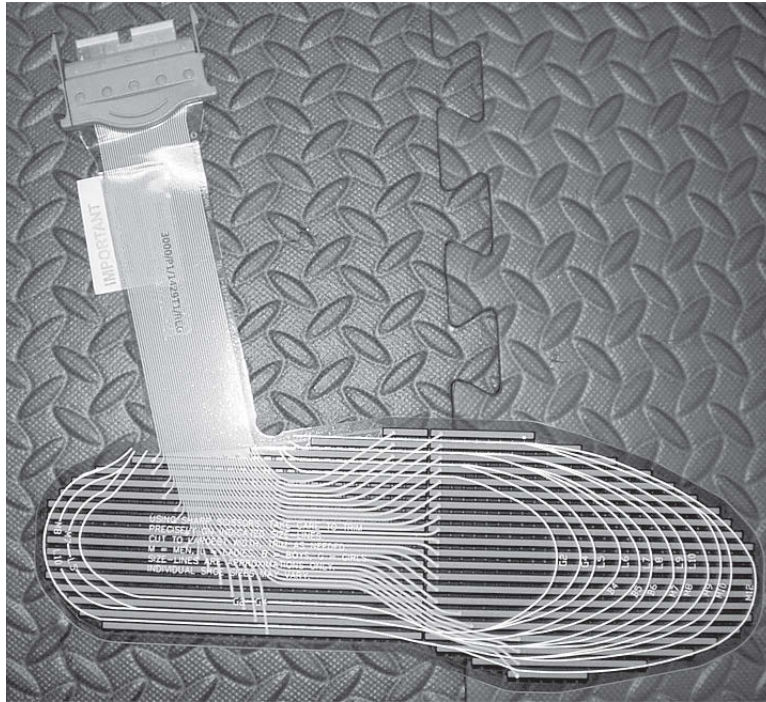


Figure 98: *F-Scan insole.*



Figure 99: *MOOG motion platform surrounded by OptiTrack camera system.*



Figure 100: Six-axis force/torque measurement system.

- Position and angular limits managed by the platform's control system, which acts as an intermediary between a user's commanded motions and the motion base's hardware.
- Hardware limit switches which prevent the platform from exceeding specific positions and angles.
- Emergency shutoff switches. When any switch is pressed, all communication with the motion base is halted, and the platform slowly returns to its parked position, managed only by gravity and the balance of weight on the platform.

7.3.1 Participant Health

If a subject is unwell on the day of the scheduled experiments, or if there is any indication of a health consideration which may make the experiment motion unsafe, then the experiment would be rescheduled for a future date.

7.3.2 Waiver

Participants would be required to sign that they consider themselves well and fit enough for the experimental study that they will not hold Carleton University or its

affiliates responsible for any unexpected or unintended side effects due to taking part in the study.

7.3.3 Ethics Approval

In order for these experiments to be carried out it would be necessary to obtain ethics approval from both Carleton University and DRDC. A comprehensive description of each experiment would be produced, detailing all of the safety procedures that would be carried out in order to ensure experiment success and participant well-being.

7.4 Experiment Descriptions

With a reasonable amount of effort the physical validation experiments could be converted into experiments involving humans. In general terms, the inverted pendulum would be replaced with a person, connections to the hanging pendulum and cart would be adjusted for a person, and the floor and sides of the motion base would be modified to accommodate standing requirements of the person, space requirements for the other objects, and safety requirements for both.

7.4.1 Human Subject Only

This study has two primary objectives for motion experiments with only a person maintaining balance. The first is to validate how well the inverted pendulum model matches a person when they are also trying to behave as an inverted pendulum. This means that most movement should take place at the person's ankles (ankle strategy). The second is to ask the subject to behave in a more natural way and to compare that to the results of the inverted pendulum model.

7.4.2 Human Subject and Hanging Mass

This study will simulate a person on board a ship attempting to manipulate a suspended pendulating mass. Subjects would be asked to stand on the motion platform while it is moving and while holding a cable connected to a free-hanging pendulum of varying weights. The pendulum's motion would be restricted by a cable connecting the end of the pendulum to the base of the platform. The subject's range of motion would also be limited in order to preclude the possibility of collision with the pendulum or falling off the platform.

7.4.3 Human Subject and Cart

This experiment would simulate a person on board a ship holding on to and manipulating a cart with varying degrees of freedom. Handles on the cart would allow it to

be translated toward and away from the subject. It would also be permitted to pivot about a fixed axis in some experimental cases. The cart's motion would be limited by only allowing it to translate along rails, which would have physical blocks limiting how far it can translate in each direction. The subject's range of motion would also be limited in order to prevent injury due to the cart's motions.

8 Conclusion

The project, as described in this report, achieved its intended objectives. The major accomplishments of the project are summarized below.

1. A comprehensive literature review of research relevant to shipboard human postural stability analysis was completed and documented.
2. A series of dynamic simulation models was developed to represent shipboard postural stability, typical unsteady shipboard loads, and coupling elements. Specifically, the following model development activity was completed.
 - (a) The planar Graham postural stability model was generalized such that it is now applicable in three dimensions, can be located and oriented arbitrarily on a ship, and is acted upon by an arbitrarily-placed and time-varying externally-applied load.
 - (b) A two-degree-of-freedom actively-controlled inverted pendulum postural stability model, previously developed within the Carleton University Applied Dynamics Lab, was extended to support arbitrary placement on a ship and an arbitrarily-placed and time-varying externally-applied load.
 - (c) The two-degree-of-freedom actively-controlled inverted pendulum postural stability model, previously developed within the Carleton University Applied Dynamics Lab, was modified such that it can be applied for representing an unsteady shipboard pendulating load, also having a time-varying external force acting on it.
 - (d) A two-degree-of-freedom unsteady shipboard cart load model was developed, also having a time-varying external force acting on it.
 - (e) A displacement-dependent force coupling model was developed representing a tension/compression, tension-only, or compression-only link acting between postural stability and unsteady shipboard load models.
3. The above dynamic and displacement-dependent force models were implemented in two stand-alone simulation environments. Specifically, the environments were as follows.
 - (a) A monolithic simulation was created where ship motion from a variety of sources could be used to stimulate the stability and load models described above. Each of the models was coded in an effectively independent subroutine such that, while monolithic in form, the overall simulation environment called and ran individual models in a way that mimics the way they would run in a distributed simulation.

- (b) A distributed simulation was developed based on the Carleton University Applied Dynamics Lab's VFD-RT simulation framework, using the same models implemented in the monolithic computer code. The VFD-RT framework was used to ensure that the models, as delivered upon completion of the project, are in a form that is readily compatible with the HLA distributed simulation standard. Since the project scope and budget did not support the software licences and technical staff required to implement the models in the same HLA framework used by DRDC Atlantic, the VFD-RT provided an effective means to ensure compatibility and provide a distributed environment in which the delivered models can be run immediately by DRDC-Atlantic.
- 4. Full-scale physical hardware was developed to allow experimental validation of the expanded/developed models using a six-degree-of-freedom electric motion base to simulate deck motion. Human subjects were not involved in these validation experiments.
- 5. A comprehensive series of computational and physical verification and validation experiments was run that provides confidence in the developed simulation models.
- 6. A proposed method for tuning the developed postural stability models to match the physical capabilities and responses of human subjects was presented and discussed.

Areas in which the project exceeded the initial objectives were the following.

- 1. Two shipboard postural stability models were developed, implemented, and delivered instead of one as was required by the contract.
- 2. All developed models were implemented in two simulation environments, allowing them to be run independently and without the need for additional third-party software licenses, whereas only one implementation of the simulation models was required by the contract.
- 3. The apparatus designed, manufactured, and used for validating the computational models was developed at full scale such that it is suitable for use in potential follow-on work to tune and validate the models using trials involving human subjects.

Overall, the project has resulted in tools for supporting the investigation of the effect of unsteady shipboard loads on human postural stability. These tools can subsequently be used to improve the safety and efficiency of shipboard personnel while performing tasks that involve interacting with unsteady shipboard loads.

References

- [1] Peeters, H., Caberg, H., and Mol, J. (1985), Evaluation of Biomechanical Models in Posturography, *Medical and Biological Engineering and Computing*, 23(5), 469–473. exp model ip.
- [2] Benvenuti, F. (2001), Physiology of Human Balance, *Advances in Neurology*, 87, 41–51.
- [3] Nashner, L. (1982), Adaptation of Human Movement to Altered Environments, *Trends in Neurosciences*, 5, 358–361.
- [4] Winter, D., Patla, A., Francois, P., Ishac, M., and Gielo-Perczak, K. (1998), Stiffness Control of Balance in Quiet Standing, *Journal of Neurophysiology*, 5, 1211–1221. con exp ip.
- [5] Bothner, K. and Jensen, J. (2001), How Do Non-Muscular Torques Contribute to the Kinetics of Postural Recovery Following a Support Surface Translation, *Journal of Biomechanics*, 34(2), 245–250. exp ps con.
- [6] Gubina, F., Hemami, H., and McGhee, R. B. (1974), On the Dynamic Stability of Bipe Locomotion, *IEEE Transactions on Biomedical Engineering*, 21(2), 102–108.
- [7] Chow, C. K. and Jacobson, D. H. (1972), Further Studies of Human Locomotion Postural Stability and Control, *Mathematical Biosciences*, 15, 93–108.
- [8] Murray, M., Seireg, A., and Sepic, S. (1975), Normal Postural Stability and Steadiness: Quantitative Assessment, *Journal of Bone and Joint Surgery*, 57, 510–516. exp.
- [9] Hemami, H. and Golliday, C. (1976), Postural Stability of the Two-Degree-Of-Freedom Biped by General Linear Feedback, *IEEE Transactions on Automatic Control*, AC-21, 74–79.
- [10] Hemami, H. (1977), The Inverted Pendulum and Biped Stability, *Mathematical Biosciences*, 34(2), 95–110. model ip.
- [11] Hemami, H. and Jaswa, V. (1978), On a Three-Link Model of the Dynamics of Standing Up and Sitting Down, *IEEE Transactions on Systems, Man and Cybernetics*, SMC-8, 120–135. model ip.

- [12] Hemami, H., Weimer, F., Robinson, C., Stockwell, C., and Cvetkovic, S. (1978), Biped stability considerations with vestibular models, *IEEE Trans. Automat. Contr.*, AC-23, 1074–1079.
- [13] Nashner, L. M. (1971), A Model Describing Vestibular Detection of Body Sway Motion, *Acta Otolaryngol*, 72, 429–436.
- [14] Koozekanani, S., Stockwell, C., McGhee, R., and Firoozmand, F. (1980), On the Role of Dynamic Models in Quantitative Posturography, *IEEE Transactions on Biomedical Engineering*, BME-27(10), 605–609. model ip.
- [15] Stockwell, C., Koozekanai, S., and Barin, K. (1981), A Physical Model of Human Postural Dynamics, *Annals of the New York Academy of Sciences*, 374, 722–730. exp model ip.
- [16] Hemami, H., Hines, M., Goddard, R., and Friedman, B. (1982), Biped Sway in the Frontal Plane with Locked Knees, *IEEE Transactions on Systems, Man and Cybernetics*, SMC-12(4), 577–582. model fr.
- [17] Hemami, H. and Chen, B. (1984), Stability Analysis and Input Design of a Two-Link Planar Biped, *The International Journal of Robotics Resesarch*, 3(2), 93–100.
- [18] Barin, K. (1989), Evaluation of a Generalized Model of Human Postural Dynamics and Control in the Sagittal Plane, *Journal of Biological Cybernetics*, 61, 37–50.
- [19] Riccio, G. E., Martin, E. J., and Stoffregen, T. A. (1992), The Role of Balance Dynamics in the Active Perception of Orientation, *Journal of Experimental Psycology Human Perception and Performance*, 18(3), 624–644.
- [20] Riccio, G. E. and Stoffregen, T. A. (1990), Gravitoinertial Force Versus the Direction of Balance in the Perception and Control of Orientation, *Psychological Review*, 97(1), 135–137.
- [21] Riccio, G. E. (1993), Information in Movement Variability About the Qualitative Dynamics of Posture and Orientation, *Variability and Motor Control*, pp. 317–357.
- [22] Iqbal, K., Hemami, H., and Simon, S. (1993), Stability and Control of a Frontal Four-Link Biped System, *IEEE Transations on Biomedical Engineering*, 40(10), 1007–1018.
- [23] Patton, J., Pai, Y., and Lee, W. (1997), A Simple Model of the Feasible Limits to Postural Stability, In *19th International IEEE Conference, Chicago, IL, USA*. exp ps.

- [24] Patton, J. L., Pai, Y. C., and Lee, W. A. (1999), Evaluation of a Model that Determines the Stability Limits of Dynamic Balance, *Gait and Posture*, 9, 38–49.
- [25] Slobounov, S. M., Moss, S. A., Slobounova, E. S., and Newell, K. M. (1998), Aging and Time to Instability in Posture, *Journal of Gerontology; Biological Sciences*, 53A(1), B71–B78.
- [26] Wu, Q., Thornton-Trump, A. B., and Sepehri, N. (1998), Lyapunov Stability Control of Inverted Pendulums with General Base Point Motion, *International Journal of Non-Linear Mechanics*, 33(5), 801–818.
- [27] Wu, Q. and Swain, R. (2000), On Lyapunov’s Stability Control of Two-Link Base Excited Inverted Pendulums with Applications to Human Locomotion, In *IEEE International Conference on Systems, Man, and Cybernetics*.
- [28] Hemami, H., Barin, K., and Pai, Y. (2006), Quantitative Analysis of the Ankle Strategy Under Translational Platform Disturbances, *IEEE Transactions on Neural Systems and Rehabilitation Engineering*, 14:4, 470–480.
- [29] Schmid, M. and Conforto, S. (2007), Stability Limits in the Assessment of Postural Control Through the Time-to-Boundary Function, In *Engineering in Medicine and Biology Society, 29th Annual Conference of the IEEE*, Lyon, France.
- [30] Humphrey, L., Hemami, H., Barin, K., and Krishnamurthy, A. (2010), Simulated Responses to Support Surface Disturbances in Humanoid Biped Model With a Vestibular-Like Apparatus, *IEEE Transactions on Systems, Man and Cybernetics*, 40(1), 109–119. ps model con.
- [31] Nashner, L. (1970), Sensory Feedback in Human Posture Control, Ph.D. thesis, Massachusetts Institute of Technology.
- [32] Geurssen, J., Altena, D., Massen, C.-H., and Verduin, M. (1976), A Model of the Standing Man for the Description of his Dynamic Behavior, *Agressologie*, 17B, 63–69. model ip.
- [33] Hemami, H. and Cvetkovic, V. (1977), Postural Stability of Two Biped Models via Lyapunov Second Method, *IEEE Transactions on Automatic Control*.
- [34] Ishida, A. (1980), Responses of the Posture-Control System to Pseudorandom Acceleration Disturbances, *Medical and Biological Engineering and Computing*, 18(4), 433–438. exp.
- [35] Hemami, H. and Stokes, B. (1983), A Qualitative discussion of mechanisms of feedback and feedforward in the control of locomotion, *IEEE Trans. Biomed. Eng.*, BME-30, 681–688.

- [36] Horak, F. and Nashner, L. (1986), Central programming of postural movements: adaptation to altered support-surface configurations, *Journal of Neurophysiology*, 55, 1369–1381.
- [37] Maki, B., Holliday, P., and Fernie, G. (1987), A Posture Control Model and Balance Test for the Prediction of Relative Postural Stability, *IEEE Transactions on Biomedical Engineering*, BME-34(10).
- [38] Horak, F. B., Nashner, L. M., and Diener, H. (1990), Postural strategies associated with somatosensory and vestibular loss, *Experimental Brain Research*, 82, 167–177.
- [39] Horstmann, G. and Dietz, V. (1990), A basic posture control mechanism: the stabilization of the centre of gravity, *Electroenceph. Clin. Neurophys.*, 76, 165–176.
- [40] He, J., Levine, W., and Loeb, G. (1991), Feedback gains for correcting small perturbations to standing posture, *IEEE Trans*, 36, 322–332.
- [41] Hasan, S., Shiavi, R., Peterson, S., and Bonds, A. (1992), Postural Control of a Two Degree of Freedom Biped Using a Simple Neural Network, In *Engineering in Medicine and Biology Society, 14th Annual International Conference of the IEEE*, Vol. 1, pp. 37–38, Paris.
- [42] Kuo, A. and Zajac, F. (1993), Human standing posture: Multijoint movement strategies based on biomechanical constraints, *Progress in Brain Research*, 97, 349–358.
- [43] Kuo, A. (1995), An Optimal Control Model for Analyzing Human Postural Balance, *IEEE Transactions on Biomedical Engineering*, 42(1), 87–101. con.
- [44] Tian, C. and He, J. (1997), Simulation Study of Human Posture Control Under External Perturbation, In *IEEE Conference on Decision and Control*, San Diego, CA, USA. con ps.
- [45] Henry, S., Fung, J., and Horak, F. (1998), Control of Stance During Lateral and Anterior/Posterior Surface Translations, *IEEE Transactions on Rehabilitation Engineering*, 6, 32–42. exp ps con.
- [46] van der Kooij, H., Jacobs, R., Koopman, B., and Groontenboer, H. (1999), A Multisensory Integration Model of Human Stance Control, *Biological Cybernetics*, 80, 299–308. con 3-link ip.
- [47] van der Kooij, H., Jacobs, R., Kiipan, B., and van der Helm, F. (2001), An Adaptive Model of Sensory Integration in a Dynamic Environment Applied to Human Stance Control, In *American Control Conference*, pp. 2297–2298.

- [48] Corna, S., Tarantola, J., Nardone, A., Giordano, A., and Schieppati, M. (1999), Standing on a Continuously Moving Platform: Is body inertial counteracted or exploited?, *Experimental Brain Research*, 124(3), 331–341. exp ps con.
- [49] Wang, Q. and He, J. (1999), Control Model of Postural Stability Using LQR and Fuzzy Logic Controller, In *Proceedings of The First Joint BMES/EMBS Conference Serving Humanity, Advancing Technology*.
- [50] He, J., Maltenfort, M., Wang, Q., and Hamm, T. (2001), Learning From Biological Systems: Modeling Neural Control, *Control Systems, IEEE*, 21:4, 55–69.
- [51] Wu, Q. (1999), Lyapunov’s Stability Control of Constrained Inverted Pendulum, In *Proceedings of the American Control Conference*.
- [52] Ito, S. and Kawasaki, H. (2000), A Standing Posture Control Based on Ground Reaction Force, In *Proceedings of the 2000 IEEE/RSJ International Conference on Intelligent Robots and Systems*.
- [53] Mihelj, M., Matjacic, Z., and Bajd, T. (2000), Postural Activity of Constrained Subject in Response to Disturbance in Sagittal Plane, *Gait and Posture*, 12, 94–104.
- [54] Matjacic, Z., Voigt, M., Popovic, D., and Sinkjaer, T. (2001), Functional Postural Responses After Perturbations in Multiple Directions in a Standing Man: A Principle of Decoupled Control, *Journal of Biomechanics*, 34(2), 187–196. exp ps.
- [55] Micheau, P., Kron, A., and Bourassa, P. (2001), Analysis of Human Postural Stability Based on the Inverted Pendulum Model with Time-Delay in Feedback, In *American Control Conference*, pp. 2297–2298. model ip con.
- [56] Iqbal, K., Roy, A., and Imran, M. (2003), Passive and Active Contributors to Postural Stabilization, *IEEE International Conference on Systems, Man and Cybernetics*, 5, 4502–4507.
- [57] Roy, A. and Iqbal, K. (2003), PID Controller Stabilization of a Single-Link Biomechanical Model with Multiple Delayed Feedbacks, In *IEEE International Conference on Systems, Man and Cybernetics*.
- [58] Frazier, P. and Chouikha, M. (2004), A Novel Control Model for Elucidating Human Postural Balance, In *Proceedings of the 5th World Congress on Intelligent Control and Automation*.
- [59] Lydoire, F. and Poignet, P. (2005), Nonlinear Model Predictive Control via Interval Analysis, In *Proceedings of the 44th IEEE Conference on Decision and Control*.

- [60] Jiang, Y. and Kimura, H. (2006), A PID Model of Balance Keeping Control and Its Application to Stability Assessment, In *Proceedings of the 2006 IEEE/RSJ International Conference on Intelligent Robots and Systems*.
- [61] Scrivens, J., Ting, L., and DeWeerth, S. (2006), Effects of Stance Width on Control Gain in Standing Balance, In *Proceedings of the 28th IEEE EMBS Annual International Conference*.
- [62] Virk, S. and McConville, K. (2006), Virtual Reality Applications in Improving Postural Control and Minimizing Falls, In *Proceedings of the 28th IEEE EMBS Annual International Conference*, New York.
- [63] Bustamante Valles, K., Schneider, J., Long, J., Riedel, S., Johnson, M., and Harris, G. (2006), Combined Sagittal and Coronal Plane Postural Stability Model, In *Proceedings of the 28th IEEE EMBS Annual International Conference*.
- [64] Bustamante Valles, K., Long, J., Riedel, S., Graf, A., Krzak, J., Hassani, S., Sturm, P., and Harris, G. (2009), Using a Bi-Planar Postural Stability Model to Assess Children with Scoliosis, In *31st Annual International Conference of the IEEE EMBS*.
- [65] Pilkar, R., Moosbrugger, J., Bhatkar, V., Schilling, R., Storey, C., and Robinson, C. (2007), A Biomechanical Model of Human Ankle Angle Changes Arising From Short Peri-Threshold Anterior Translations of Platform on Which a Subject Stands, In *Proceedings of the 29th Annual International Conference of the IEEE EMBS Cite Internationale*.
- [66] Finley, J., Dhaher, Y., and Perreault, E. (2009), Regulation of Feed-Forward and Feedback Strategies at the Human Ankle During Balance Control, In *31st Annual International Conference of the IEEE EMBS*.
- [67] Xinjilefu, V., Hayward and Michalska, H. (2009), Stabilization of the Spatial Double Inverted Pendulum Using Stochastic Programming Seen as a Model of Standing Postural Control, In *9th IEEE-RAS International Conference on Humanoid Robots*.
- [68] Langlois, R. G. (2010), Development of a Spatial Inverted Pendulum Shipboard Postural Stability Model, In *International Conference on Human Performance at Sea*, Glasgow, Scotland. ps ip con model.
- [69] Sovol, A., Bustamante Valles, K., Riedel, S., and Harris, G. (2010), Bi-Planar Postural Stability Model: Fitting Model Parameters to Patient Data Automatically, In *32nd Annual International Conference of the IEEE IMBS*.

- [70] Davidson, B., Madigan, M., Southward, S., and Nussbaum, M. (2011), Neural Control of Posture During Small Magnitude Perturbations: Effects of Aging and Localized Muscle Fatigue, *IEEE Transactions on Biomedical Engineering*, Vol. 58.
- [71] Matthews, J., Mackinnon, S., Albert, W., Holmes, M., and Patterson, A. (2007), Effects of Moving Environments on the Physical Demands of Heavy Materials Handling Operators, *International Journal of Industrial Ergonomics*, 37(1), 43–50. ps.
- [72] Baitis, A., Applebee, T., and McNamara, T. (1984), Human Factors Considerations Applied to Operations of the FFG-8 and Lamps MK III, *Naval Engineers Journal*, 97(4), 191–199.
- [73] Graham, R., Baitis, A., and Meyers, W. (1992), On the Development of Seakeeping Criteria, *Naval Engineers Journal*, 104, 259–275. mii.
- [74] Graham, R. (1990), Motion Induced Interruptions as Ship Operability Criteria, *Naval Engineers Journal*, 102, 65–71.
- [75] Maki, B., W.E., M., and Perry, S. (1996), Influence of Lateral Destabilization on Compensatory Stepping Responses, *Journal of Biomechanics*, 29(3), 343–353. exp step.
- [76] Crossland, P. (1996), Using the Large Motion Simulator (LMS) at DRA Bedford to Investigate the Effects of Ship Motions on Motion Induced Interruptions, (Technical Report DRA/SS/SSHE/CR96008) Defence Research Agency.
- [77] Crossland, P., Rich, K., and Granshaw, D. (1997), Validating a Model for Predicting Motion Induced Interruptions to Task Performance Using Simulated Motions From the FFG-8 and Type 23 Frigate, (Technical Report DERA/SS/HE/CR971017) Defence Evaluation and Research Agency.
- [78] Crossland, P. and Rich, K. (1998), Validating a Model of the Effects of Ship Motion on Postural Stability, *International Conference of Environmental Ergonomics*, pp. 385–388. exp mii.
- [79] McIlroy, W. and Maki, B. (1993), Task Constraints on Foot Movement and the Incidence of Compensatory Stepping Following Perturbation of Upright Stance, *Brain Research*, 616, 30–38.
- [80] Maki, B. and McIlroy, W. (1997), The Role of Limb Movements in Maintaining Upright Stance: The “Change-in-Support” Strategy, *Physical Therapy*, 77(5), 488–507.

- [81] Mckee, J. (2004), Simulating the Effects of Ship Motion on Postural Stability Using Articulated Dynamic Models, Ph.D. thesis, Carleton University.
- [82] Baitis, A., Holcomb, F., Conwell, S., Crossland, P., Patton, J., and Strong, R. (1995), Motion Induced Interruption (MII) and Motion Induced Fatigue (MIF) experiments at the Naval Biodynamics Laboratory, (Technical Report CRDKNSWE-HD-1423-01) Carderock Division, Naval Surface Warfare Center.
- [83] Duncan, C. A., MacKinnon, S. N., Alberta, W. J., Antlec, D. M., and Matthews, J. (2007), Effect of simulated vessel motions on thoracolumbar and centre of pressure kinematics, *Occupational Ergonomics*, 7, 265–274.
- [84] Duncan, C., MacKinnon, S., and Albert, W. (2009), Changes in thoracolumbar kinematics and centre of pressure when performing stationary tasks in moving environments, Technical Report Memorial University of Newfoundland.
- [85] Hasson, C. J., Emmerik, R. E. V., and Caldwell, G. E. (2008), Predicting dynamic postural instability using center of mass time-to-contact information, *Journal of Biomechanics*, pp. 2121–2129.
- [86] Hof, A., Gazendam, M., and Sinke, W. (2005), The condition for dynamic stability, *Journal of Biodynamics*, 38, 1–8.
- [87] Langlois, R., Mackinnon, S., and Duncan, C. (2009), Modelling Sea Trial Motion Induced Interruption Data Using an Inverted Pendulum Articulated Postural Stability Model, *International Journal of Maritime Engineering*, Vol. 151. mii ip.
- [88] Nikravesh, P. E. (1988), Computer-aided Analysis of Mechanical Systems, New Jersey, USA: Prentice-Hall, Inc.
- [89] Military Agency for Standardization (1983), Standardized Wave and Wind Environments and Shipboard Reporting of Sea Conditions, (Standardization Agreement (STANAG) 4194) North Atlantic Treaty Organization.
- [90] Tsui, K. and Langlois, R. (2008), Development of the Virtual Flight Deck - Real Time (VFD-RT) simulation environment, In *Proceedings of the 2008 Spring Simulation Multiconference (SpringSim'08)*, Society for Modeling and Simulation International (SCS), Ottawa, Canada.
- [91] (2008), MOOG FCS 6DOF2000E (Model 170-131) Motion System User's Manual, Cds7238 ed.

Annex A: Matrices $[\dot{T}_{SHIN}]$ and $[\ddot{T}_{SHIN}]$

A.1 Matrix \dot{T}_{SHIN}

Individual entries in the matrix \dot{T}_{SHIN} are as follows.

$$\begin{aligned}\dot{T}_{SHIN}(1,1) &= -s\theta_J\dot{\theta}_Jc\theta_K - c\theta_Js\theta_K\dot{\theta}_K \\ \dot{T}_{SHIN}(1,2) &= s\theta_J\dot{\theta}_Js\theta_K - c\theta_Jc\theta_K\dot{\theta}_K \\ \dot{T}_{SHIN}(1,3) &= c\theta_J\dot{\theta}_J \\ \dot{T}_{SHIN}(2,1) &= -s\theta_I\dot{\theta}_Is\theta_K + c\theta_Ic\theta_K\dot{\theta}_K + c\theta_I\dot{\theta}_Is\theta_Jc\theta_K \\ &\quad + s\theta_Ic\theta_J\dot{\theta}_Jc\theta_K - s\theta_Is\theta_Js\theta_K\dot{\theta}_K \\ \dot{T}_{SHIN}(2,2) &= -s\theta_I\dot{\theta}_Ic\theta_K - c\theta_Is\theta_K\dot{\theta}_K - c\theta_I\dot{\theta}_Is\theta_Js\theta_K \\ &\quad - s\theta_Ic\theta_J \\ \dot{T}_{SHIN}(2,3) &= \dot{\theta}_Js\theta_K - s\theta_Is\theta_Jc\theta_K\dot{\theta}_K - c\theta_I\dot{\theta}_Ic\theta_J \\ &\quad + s\theta_Is\theta_J\dot{\theta}_J \\ \dot{T}_{SHIN}(3,1) &= c\theta_I\dot{\theta}_Is\theta_K + s\theta_Ic\theta_K\dot{\theta}_K + s\theta_I\dot{\theta}_Is\theta_Jc\theta_K \\ &\quad - c\theta_Ic\theta_J \\ \dot{T}_{SHIN}(3,2) &= \dot{\theta}_Jc\theta_K + c\theta_Is\theta_Js\theta_K\dot{\theta}_Kc\theta_I\dot{\theta}_Ic\theta_K \\ &\quad - s\theta_Is\theta_K\dot{\theta}_K - s\theta_I\dot{\theta}_Is\theta_Js\theta_K + c\theta_Ic\theta_J \\ \dot{T}_{SHIN}(3,3) &= \dot{\theta}_Js\theta_K + c\theta_Is\theta_Jc\theta_K\dot{\theta}_K - s\theta_I\dot{\theta}_Ic\theta_J \\ &\quad - c\theta_Is\theta_J\dot{\theta}_J\end{aligned}$$

A.2 Matrix \ddot{T}_{SHIN}

Individual entries in the matrix \ddot{T}_{SHIN} are as follows.

$$\begin{aligned}
\ddot{T}_{SHIN}(1,1) &= -c\theta_J\dot{\theta}_J^2c\theta_K - s\theta_J\ddot{\theta}_Jc\theta_K + 2s\theta_J\dot{\theta}_J s\theta_K\dot{\theta}_K - c\theta_Jc\theta_K\dot{\theta}_K^2 \\
&\quad - c\theta_Js\theta_K\ddot{\theta}_K \\
\ddot{T}_{SHIN}(1,2) &= c\theta_J\dot{\theta}_J^2s\theta_K + s\theta_J\ddot{\theta}_J s\theta_K + 2s\theta_J\dot{\theta}_J c\theta_K\dot{\theta}_K + c\theta_Js\theta_K\dot{\theta}_K^2 \\
&\quad - c\theta_Jc\theta_K\ddot{\theta}_K \\
\ddot{T}_{SHIN}(1,3) &= -s\theta_J\dot{\theta}_J^2 + c\theta_J\ddot{\theta}_J \\
\ddot{T}_{SHIN}(2,1) &= -c\theta_I\dot{\theta}_I^2s\theta_K - s\theta_I\ddot{\theta}_I s\theta_K - 2s\theta_I\dot{\theta}_I c\theta_K\dot{\theta}_K - c\theta_I s\theta_K\dot{\theta}_K^2 \\
&\quad + c\theta_Ic\theta_K\ddot{\theta}_K - s\theta_I\dot{\theta}_I^2s\theta_Jc\theta_K + c\theta_I\ddot{\theta}_I s\theta_Jc\theta_K + 2c\theta_I\dot{\theta}_I c\theta_J\dot{\theta}_Jc\theta_K \\
&\quad - 2c\theta_I\dot{\theta}_I s\theta_Js\theta_K\dot{\theta}_K - s\theta_I s\theta_J\dot{\theta}_J^2c\theta_K + s\theta_Ic\theta_J\ddot{\theta}_Jc\theta_K - 2s\theta_Ic\theta_J\dot{\theta}_J s\theta_K\dot{\theta}_K \\
&\quad - s\theta_I s\theta_Jc\theta_K\dot{\theta}_K^2 - s\theta_I s\theta_Js\theta_K\ddot{\theta}_K \\
\ddot{T}_{SHIN}(2,2) &= -c\theta_I\dot{\theta}_I^2c\theta_K - s\theta_I\ddot{\theta}_I c\theta_K + 2s\theta_I\dot{\theta}_I s\theta_K\dot{\theta}_K \\
&\quad - c\theta_Ic\theta_K\dot{\theta}_K^2 - c\theta_I s\theta_K\ddot{\theta}_K + s\theta_I\dot{\theta}_I^2s\theta_Js\theta_K \\
&\quad - c\theta_I\ddot{\theta}_I s\theta_Js\theta_K - 2c\theta_I\dot{\theta}_I c\theta_J\dot{\theta}_J s\theta_K \\
&\quad - 2c\theta_I\dot{\theta}_I s\theta_Jc\theta_K\dot{\theta}_K + s\theta_I s\theta_J\dot{\theta}_J^2s\theta_K \\
&\quad - s\theta_Ic\theta_J\ddot{\theta}_J s\theta_K - 2s\theta_Ic\theta_J\dot{\theta}_Jc\theta_K\dot{\theta}_K \\
&\quad + s\theta_I s\theta_Js\theta_K\dot{\theta}_K^2 - s\theta_I s\theta_Jc\theta_K\ddot{\theta}_K \\
\ddot{T}_{SHIN}(2,3) &= s\theta_I\dot{\theta}_I^2c\theta_J - c\theta_I\ddot{\theta}_I c\theta_J + 2c\theta_I\dot{\theta}_I s\theta_J\dot{\theta}_J \\
&\quad + s\theta_Ic\theta_J\dot{\theta}_J^2 + s\theta_I s\theta_J\ddot{\theta}_J^2 \\
\ddot{T}_{SHIN}(3,1) &= -s\theta_I\dot{\theta}_I^2s\theta_K + c\theta_I\ddot{\theta}_I s\theta_K + 2c\theta_I\dot{\theta}_I c\theta_K\dot{\theta}_K \\
&\quad - s\theta_I s\theta_K\dot{\theta}_K^2 + s\theta_Ic\theta_K\ddot{\theta}_K + c\theta_I\dot{\theta}_I^2s\theta_Jc\theta_K \\
&\quad + s\theta_I\ddot{\theta}_I s\theta_Jc\theta_K + 2s\theta_I\dot{\theta}_I c\theta_J\dot{\theta}_Jc\theta_K \\
&\quad - 2s\theta_I\dot{\theta}_I s\theta_Js\theta_K\dot{\theta}_K + c\theta_I s\theta_J\dot{\theta}_J^2c\theta_K \\
&\quad - c\theta_Ic\theta_J\ddot{\theta}_Jc\theta_K + 2c\theta_Ic\theta_J\dot{\theta}_J s\theta_K\dot{\theta}_K \\
&\quad + c\theta_I s\theta_Jc\theta_K\dot{\theta}_K^2 + c\theta_I s\theta_Js\theta_K\ddot{\theta}_K \\
\ddot{T}_{SHIN}(3,2) &= -s\theta_I\dot{\theta}_I^2c\theta_K + c\theta_I\ddot{\theta}_I c\theta_K - 2c\theta_I\dot{\theta}_I s\theta_K\dot{\theta}_K \\
&\quad - s\theta_Ic\theta_K\dot{\theta}_K^2 - s\theta_I s\theta_K\ddot{\theta}_K - c\theta_I\dot{\theta}_I^2s\theta_Js\theta_K \\
&\quad - s\theta_I\ddot{\theta}_I s\theta_Js\theta_K - 2s\theta_I\dot{\theta}_I c\theta_J\dot{\theta}_J s\theta_K \\
&\quad - 2s\theta_I\dot{\theta}_I s\theta_Jc\theta_K\dot{\theta}_K - c\theta_I s\theta_J\dot{\theta}_J^2s\theta_K \\
&\quad + c\theta_Ic\theta_J\ddot{\theta}_J s\theta_K + 2c\theta_Ic\theta_J\dot{\theta}_Jc\theta_K\dot{\theta}_K \\
&\quad - c\theta_I s\theta_Js\theta_K\dot{\theta}_K^2 + c\theta_I s\theta_Jc\theta_K\ddot{\theta}_K \\
\ddot{T}_{SHIN}(3,3) &= -c\theta_I\dot{\theta}_I^2c\theta_J - s\theta_I\ddot{\theta}_I c\theta_J + 2s\theta_I\dot{\theta}_I s\theta_J\dot{\theta}_J \\
&\quad - c\theta_Ic\theta_J\dot{\theta}_J^2 - c\theta_I s\theta_J\ddot{\theta}_J
\end{aligned}$$

Annex B: Mass Property Data Sheets

```

VOLUME = 3.6884442e+02 INCH^3
SURFACE AREA = 2.0254911e+03 INCH^2
AVERAGE DENSITY = 2.4558492e-01 POUND / INCH^3
MASS = 9.0582628e+01 POUND

CENTER OF GRAVITY with respect to ROTATION_CENTRE coordinate frame:
X Y Z 4.4248974e-02 -3.4922689e+00 5.5597137e+00 INCH

INERTIA with respect to ROTATION_CENTRE coordinate frame: (POUND * INCH^2)

INERTIA TENSOR:
Ixx Ixy Izx 1.9156651e+04 1.0846687e+00 -5.4692351e-01
Iyx Iyy Iyz 1.0846687e+00 1.5685799e+04 8.0521169e+02
Izx Izy Izz -5.4692351e-01 8.0521169e+02 3.9193450e+03

INERTIA at CENTER OF GRAVITY with respect to ROTATION_CENTRE coordinate frame: (POUND * INCH^2)

INERTIA TENSOR:
Ixx Ixy Izx 1.5251964e+04 -1.2913003e+01 2.1737456e+01
Iyx Iyy Iyz -1.2913003e+01 1.2885674e+04 -9.5354200e+02
Izx Izy Izz 2.1737456e+01 -9.5354200e+02 2.8144272e+03

PRINCIPAL MOMENTS OF INERTIA: (POUND * INCH^2)
I1 I2 I3 2.7249079e+03 1.2975063e+04 1.5252095e+04

ROTATION MATRIX from ROTATION_CENTRE orientation to PRINCIPAL AXES:
-0.00163 0.00654 -0.99998
0.09343 0.99561 0.00636
0.99562 -0.09342 -0.00224

ROTATION ANGLES from ROTATION_CENTRE orientation to PRINCIPAL AXES (degrees):
angles about x y z -109.370 -89.614 -104.010

RADII OF GYRATION with respect to PRINCIPAL AXES:
R1 R2 R3 5.4847073e+00 1.1968295e+01 1.2976043e+01 INCH

-----

MASS PROPERTIES OF COMPONENTS OF THE ASSEMBLY
(in assembly units and the ROTATION_CENTRE coordinate frame)

DENSITY MASS C.G.: X Y Z
DRIVE_JOINT_SIDING MATERIAL: UNKNOWN
2.83600e-01 3.83449e+00 2.83200e-16 4.62500e+00 3.24040e+00
IPM_BEARING MATERIAL: STEEL
2.82771e-01 1.26122e+00 2.66746e-16 4.35630e+00 0.00000e+00
DRIVE_JOINT MATERIAL: UNKNOWN
2.83600e-01 2.50376e+01 1.57434e-01 1.57434e-01 2.69490e-03
IPM_BEARING MATERIAL: STEEL
2.82771e-01 1.26122e+00 -2.66710e-16 -4.35570e+00 0.00000e+00
IPM_BEARING MATERIAL: STEEL
2.82771e-01 1.26122e+00 4.35570e+00 -1.44551e-09 0.00000e+00
IPM_BEARING MATERIAL: STEEL
2.82771e-01 1.26122e+00 -4.35570e+00 -1.44551e-09 0.00000e+00
DRIVE_JOINT_SIDING MATERIAL: UNKNOWN
2.83600e-01 3.83449e+00 -2.83163e-16 -4.62440e+00 3.24040e+00
DRIVEJOINT_BASEPLATE MATERIAL: UNKNOWN
2.83600e-01 2.35742e+00 0.00000e+00 0.00000e+00 8.06250e+00
IPM_SHAFT MATERIAL: UNKNOWN
2.83600e-01 1.08176e+01 4.61038e-24 7.52933e-08 3.20888e+01
SET_SCREW_COLLAR MATERIAL: UNKNOWN
2.83600e-01 9.71059e-01 1.08234e-03 2.97207e-08 3.70625e+01
IMP_FILLET MATERIAL: UNKNOWN
2.83600e-01 1.06350e-01 -1.61667e+00 6.25000e-02 9.12500e+00
IMP_FILLET MATERIAL: UNKNOWN
2.83600e-01 1.06350e-01 1.61667e+00 -6.25000e-02 9.12500e+00
IMP_FILLET MATERIAL: UNKNOWN
2.83600e-01 1.06350e-01 -6.25000e-02 1.61727e+00 9.12500e+00

```

Figure B.1: Inverted pendulum stability model with rotating mass and no additional mass plates. 1 of 2.

23/02/2012

IMP_FILLET	MATERIAL:	UNKNOWN
2.83600e-01 1.06350e-01 6.25000e-02 -1.61667e+00 9.12500e+00		
GEARBOX_WASHER1	MATERIAL:	UNKNOWN
2.83600e-01 5.07008e-01 -2.94797e-16 -4.81440e+00 0.00000e+00		
GEARBOX_WASHER2	MATERIAL:	UNKNOWN
2.83600e-01 6.76089e-01 -3.06431e-16 -5.00440e+00 0.00000e+00		
GEARBOX_WASHER3	MATERIAL:	UNKNOWN
2.83600e-01 1.51838e-01 -3.15999e-16 -5.16065e+00 0.00000e+00		
GEARBOX_WASHER2	MATERIAL:	UNKNOWN
2.83600e-01 6.76089e-01 -3.25566e-16 -5.31690e+00 0.00000e+00		
GEARBOX_WASHER1	MATERIAL:	UNKNOWN
2.83600e-01 5.07008e-01 2.94834e-16 4.81500e+00 0.00000e+00		
AER1202-P0403300603	MATERIAL:	UNKNOWN
1.84249e-01 2.47134e+01 -1.15915e-03 -8.94245e+00 4.56092e-01		
AKM42X-ACCNC-00	MATERIAL:	UNKNOWN
2.60117e-01 7.54239e+00 1.44464e-02 -1.21348e+01 7.29528e+00		
IPM_JOINT_BRACKET1	MATERIAL:	UNKNOWN
2.83600e-01 2.39277e-01 -3.43750e+00 2.99213e-04 7.49999e+00		
IPM_JOINT_BRACKET1	MATERIAL:	UNKNOWN
2.83600e-01 2.39277e-01 3.43750e+00 2.99213e-04 7.49999e+00		
IPM_JOINT_BRACKET1	MATERIAL:	UNKNOWN
2.83600e-01 2.39277e-01 -6.25000e-02 2.99213e-04 7.49999e+00		
IPM_JOINT_SIDEBRACKET	MATERIAL:	UNKNOWN
2.83600e-01 4.72080e-02 -1.00000e+00 4.91121e+00 5.37500e+00		
IPM_JOINT_SIDEBRACKET	MATERIAL:	UNKNOWN
2.83600e-01 4.72080e-02 -1.00000e+00 -4.91062e+00 5.37500e+00		
IPM_JOINT_SIDEBRACKET	MATERIAL:	UNKNOWN
2.83600e-01 4.72080e-02 1.00000e+00 4.91121e+00 5.37500e+00		
IPM_JOINT_SIDEBRACKET	MATERIAL:	UNKNOWN
2.83600e-01 4.72080e-02 1.00000e+00 -4.91062e+00 5.37500e+00		
DRIVE_JOINT_SIDING_THICKENER	MATERIAL:	UNKNOWN
2.83600e-01 1.28965e+00 2.67891e-16 4.37500e+00 0.00000e+00		
DRIVE_JOINT_SIDING_THICKENER	MATERIAL:	UNKNOWN
2.83600e-01 1.28965e+00 -2.67855e-16 -4.37440e+00 0.00000e+00		

Figure B.2: Inverted pendulum stability model with rotating mass and no additional mass plates, 2 of 2.

This page intentionally left blank.

Annex C: Sample Input Files

```

*** Model title ***
testpsm3d.inp test file (10/04/05) run title
*** Model parameters ***
78. mass
47.2 0. 0. inertia matrix (about the CM)
47.2 0.
1.
0. 0. 0.87 Rab(x,y,z)
0. 0. 0. 0. jointStiffness(2,2)
0. 0. 0. 0. jointDamping(2,2)
-90. 90. -90. 90. jointLimits(2,2)
1.e6 -1.e6 1.e6 -1.e6 jointTorqueLimits(2,2)
750. 50. 750. 50. controllerGains(2,2)
9.81 gravity
*** Model orientation ***
90. orientation (beta)
*** Ship motion parameters ***
Hotel-Port.txt
*** Integration parameters ***
0.2 1258.4 0.2 start time, end time, dt
0. 0. initial inclination angles (x,y), deg
0. 0. initial inclination rates (x,y), deg/s
*** Output parameters ***
1 1 output selection (screen,file)

```

Figure C.1: Sample GRM3D input file.


```

*** Model title ***
psm3d.inp test file (11/03/19)      run title
*** Rotational coordinate system ***
1 Euler angle sequence for incoming ship motion (1=XYZ,2=ZYX)
*** Model parameters ***
78. mass
47.2 0. 0.          inertia matrix (about the CM)
47.2 0.
1.
0. 0. 0.9          Rab(x,y,z)
0. 0. 0. 0.        jointStiffness(2,2)
0. 0. 0. 0.        jointDamping(2,2)
-90. 90. -90. 90.   jointLimits(2,2)
1.d6 -1.d6 1.d6 -1.d6 jointTorqueLimits(2,2)
2472.22 1972.22 2472.22 1972.22 controllerGains(2,2)
9.81              gravity
*** Model orientation ***
-50. 2. 6.44d0 rAGsh (inverted pendulum location in ship frame)
0.              orientation angle (beta)
*** Integration parameters ***
0.12           dt (internal to PSM3D subroutine)
0. 0.          initial inclination angles (x,y), deg
0. 0.          initial inclination angular rates (x,y), deg/s
0. 0.          dof constraint flags (q1,q2)
*** Output parameters ***
1 1           output selection (screen,file)

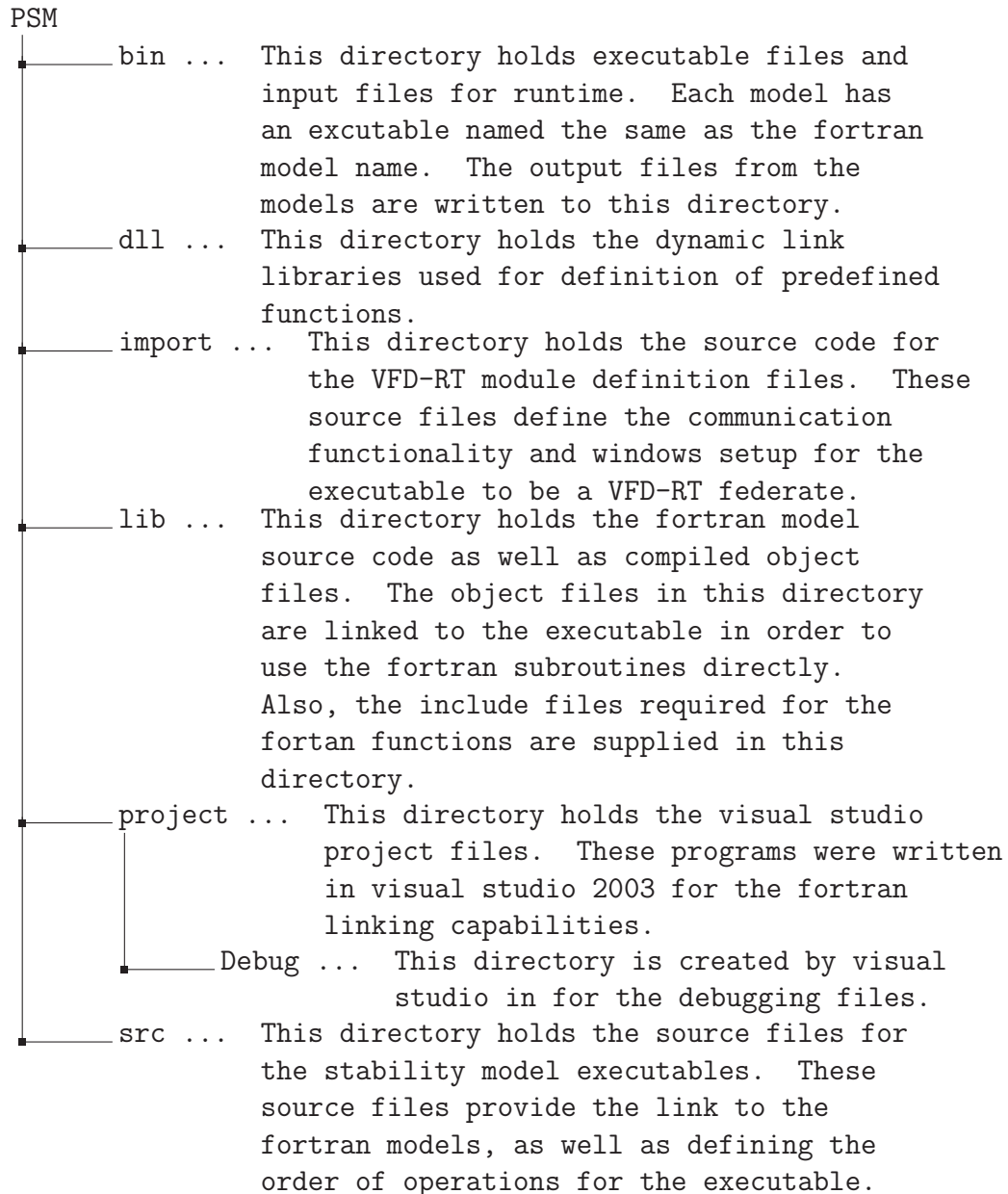
```

Figure C.2: Sample PSM3D input file.

This page intentionally left blank.

Annex D: Software Archive

The software is supplied using this file tree. The contents of each of the folders is explained in the directory tree provided. This tree is for the VFD-RT Federation. All of the Fortran models are provided in one folder.



This page intentionally left blank.

Annex E: DEPSM User Guide

The stability models provided have been implemented in two forms. This guide supports the DEPSM architecture version of the software. This simulation model was developed in a Fortran environment, and is all contained within the executable file provided called DEPSM.exe. All model parameters are specified within the input files.

The first step required to run the DEPSM simulation is to determine the mass properties and geometry of all the persons or objects to be modelled. For example, if the Graham stability model is being used, one would have to modify the grm3d.inp file with the appropriate mass properties and geometry. For the inverted pendulum, psm3d.inp would be modified; for the pendulum load, pnd3d.inp would be modified; for the cart load, crt3d.inp would be modified; and for the interface force, intfc.inp would be modified. Samples of these files have been supplied and are in the folder with the executable. All of the input parameters are explained in the files, as well as previously in Annex C.

The next input file that needs to be modified is the depsm.inp file. This file contains information on the simulation duration, the time step, as well as the source for ship motion. Again, all the input parameters are defined within the input files themselves. Finally, within the depsm.inp file there are options for which models will be used. The GRM3D or PSM3D stability models can be coupled to either the CRT3D or PND3D load model. To uncouple the models, open the interface force input file, and set the maximum tension to 0.

To execute the simulation, run the DEPSM.exe file. Key variables, such as time and tension in the coupling link/cable, will be displayed in the command prompt window while running. After the simulation has completed there will be a command prompt message to this effect. The results of the simulation will be stored in the same folder as the executable and will be labelled according to the models selected. For example, if the Graham model was used, the output would be in the file grm3d.out.

This page intentionally left blank.

Annex F: VFD-RT User Guide

The VFD-RT simulation uses a distributed framework, therefore the models are compiled within separate executables and are linked with a central program. This guide gives step-by-step instructions on how to run the simulation.

The main program is called VFD-RT.exe. This is the main communication hub for the distributed simulation. This program coordinates communication of data between simulation data providers and clients. The display of the VFD-RT program is illustrated in Figure F.1. On the left-hand side of the window are controls for setting simulation parameters including the start time and time step (in Hz) as well as controls for starting and stopping the simulation. It is important to have all the time steps consistent within the simulation, paying particular attention to the integration time steps in the stability and load model input files. The middle of this window shows the providers that are connected to the simulation. Providers are programs that provide data to the VFD-RT. Also, connect and disconnect buttons can be seen for the providers. The right-hand side of the window shows the clients that are connected to the VFD-RT. The clients are programs that take data from the VFD-RT.

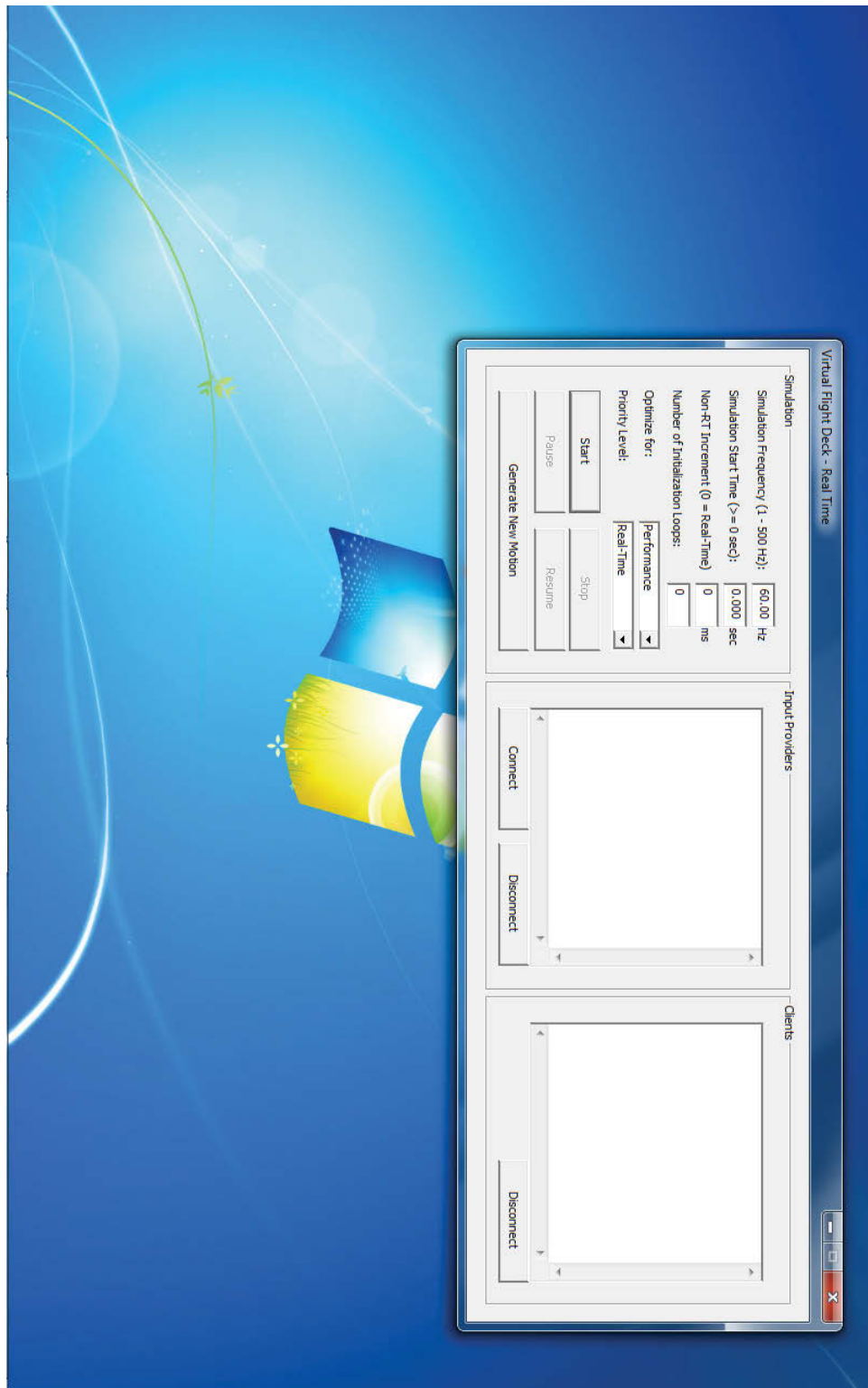


Figure F.1: VFD-RT executable graphical user interface.

In order to run the simulation, the VFD-RT.exe executable must first be started. Once it has started, the next step is to attach the providers. For this tutorial, the stability model used is the Graham model and the load model is the pendulum load. The procedure would be the same if the Graham model were switched to the inverted pendulum model and/or the pendulum load model were switched to the cart load model. There can only be one stability model and one load model running at the same time.

The first provider that needs to be connected to the VFD-RT is the ship motion provider. Two providers have been supplied with the software package. The first is entitled VFD-RT EMP.exe which stands for Experimental Motion Provider. This motion provider sends ship motion data to the VFD-RT from a tab delimited file. The second ship motion provider generates ship motion from the ShipMo3D library and is entitled vrs-sm3d.exe. This allows motions corresponding to different ships to be generated by modifying the ShipMo3D input files particular to the particular ship of interest. To connect the provider to the VFD-RT, press the connect button in the middle section of the window, the provider section, and a pop-up window as shown in Figure F.2 will appear. The pop-up window, named 'Select an Input Provider', will have a list of providers that are open and can be connected to the VFD-RT. To connect to the ShipMo3D provider select 'ShipMo3D20 Ship Motion' from the list and then press connect on the 'Select an Input Provider' window. It can then be seen on the VFD-RT window that in the input providers section, the ShipMo3D20 Ship Motion has been added to the list of providers.

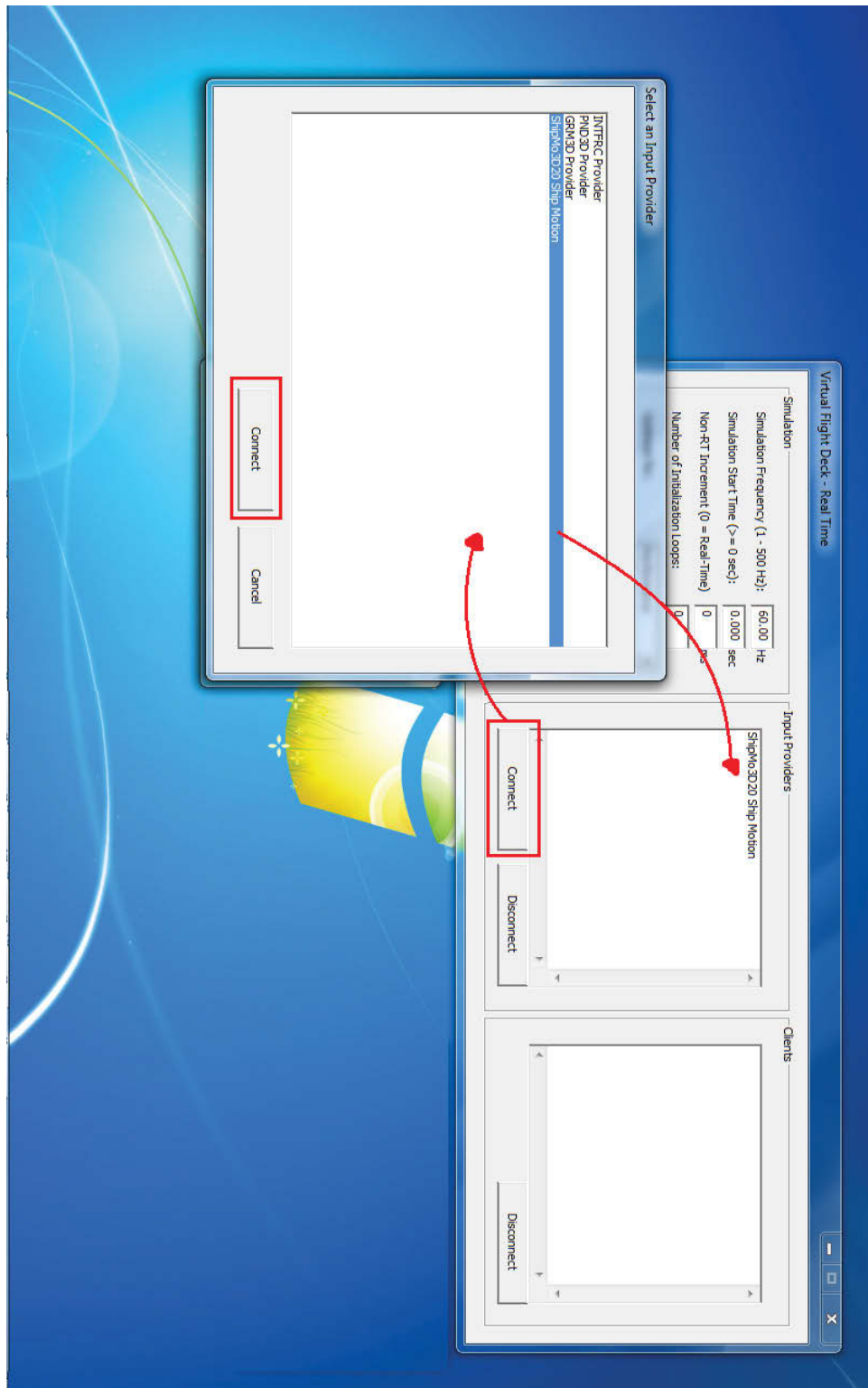


Figure F.2: Connecting providers to the VFD-RT.

Next the stability, load, and interface force models need to be connected. It is very important that the models be connected in the same order as stated in this tutorial. As each provider is connected, it is assigned a sequential number and the data locations are hard coded based on specific models being certain numbers. If the models are not connected in the appropriate order, the data will be sent to the wrong models. The models are connected to the VFD-RT in the same way as the ship motion provider. The Graham model is labeled GRM3D, the pendulum load is labeled PND3D, and the interface force is labeled INTFRC. After all the providers have been connected, the windows should look like those in Figure F.3. Finally, to ensure that all of the providers have been connected properly, in each of the model executable windows the provider status should show as 'Connected'.

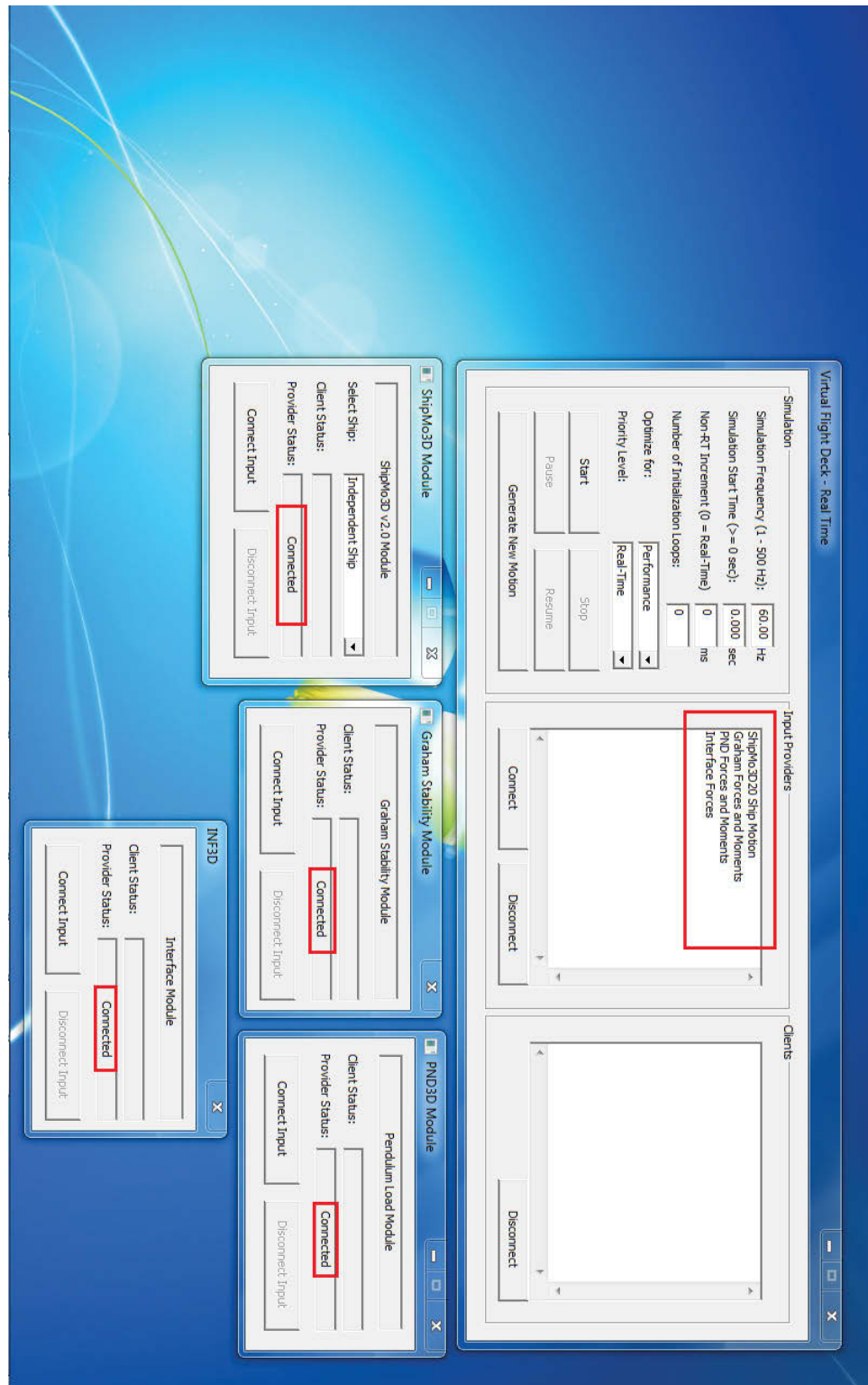


Figure F.3: Verification of connection of providers to the VFD-RT.

The next step is to connect all of the clients to the VFD-RT. All the stability and load models are providers and clients. So, first the stability and load models can be connected to the VFD-RT. The models are connected to the VFD-RT from the model executable and not from the VFD-RT. On each of the model executable windows there is a 'Connect Input' button. Pressing this button will connect the client to the VFD-RT. This can be seen in Figure F.4. When the 'Connect Input' button is pressed, the name of the client will also be added to the VFD-RT window. This lets the user know which clients are connected to the VFD-RT. Also, on the model window the 'Client Status' is shown and should be 'Connected'.

These are all the steps that are required before running the simulation, but an additional client can be used in order to see the data as the simulation is running. It is not necessary to enable this client for the results to be logged to the output files, but it may be useful when running the simulation to be able to monitor variables such as simulation time. The additional client is a viewer client and is named VFDRT-VTC.exe. This client can be connected to the VFD-RT in the same way as the other clients.

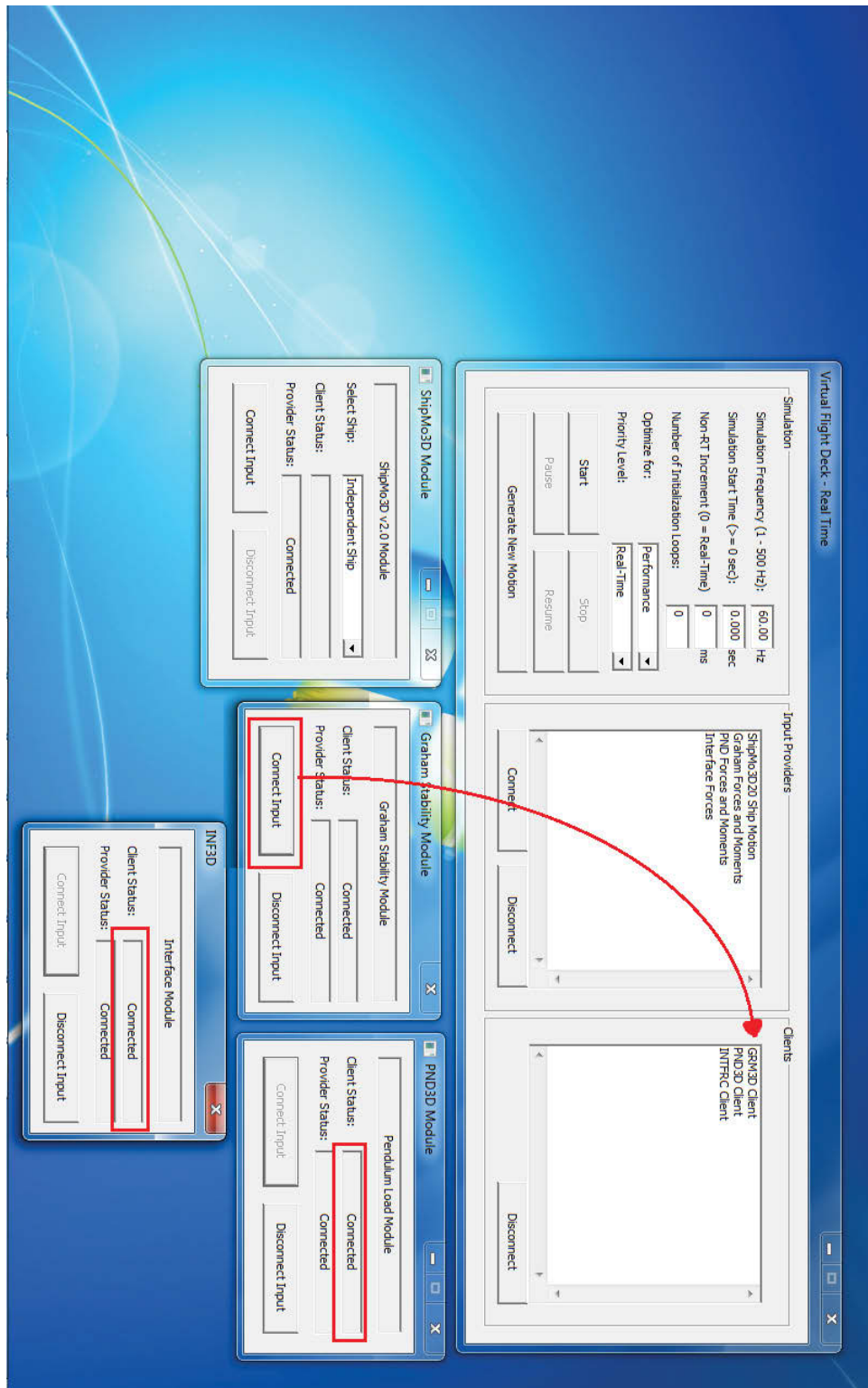


Figure F.4: Connecting clients to the VFD-RT.

Now that everything is connected to the VFD-RT, and all of the input files are corrected with matching time steps, the simulation can be run. To run the simulation, press the ‘Start’ button on the VFD-RT window. The simulation will run until either the ‘Stop’ or ‘Pause’ buttons are pressed. The ‘Stop’ button will stop the simulation, and if restarted will cause the simulation to restart from time zero. If ‘Pause’ is pressed, the simulation will stop but if restarted will start from the time when it was paused. The viewer client that was connected can be seen with the data being provided. All the data that is displayed by the viewer client as passed from the providers can be seen in Figure F.5. Results from the simulation are written to the same output files used by the DEPSM simulation. These output files can be found in the same folder that the model executables are run in.

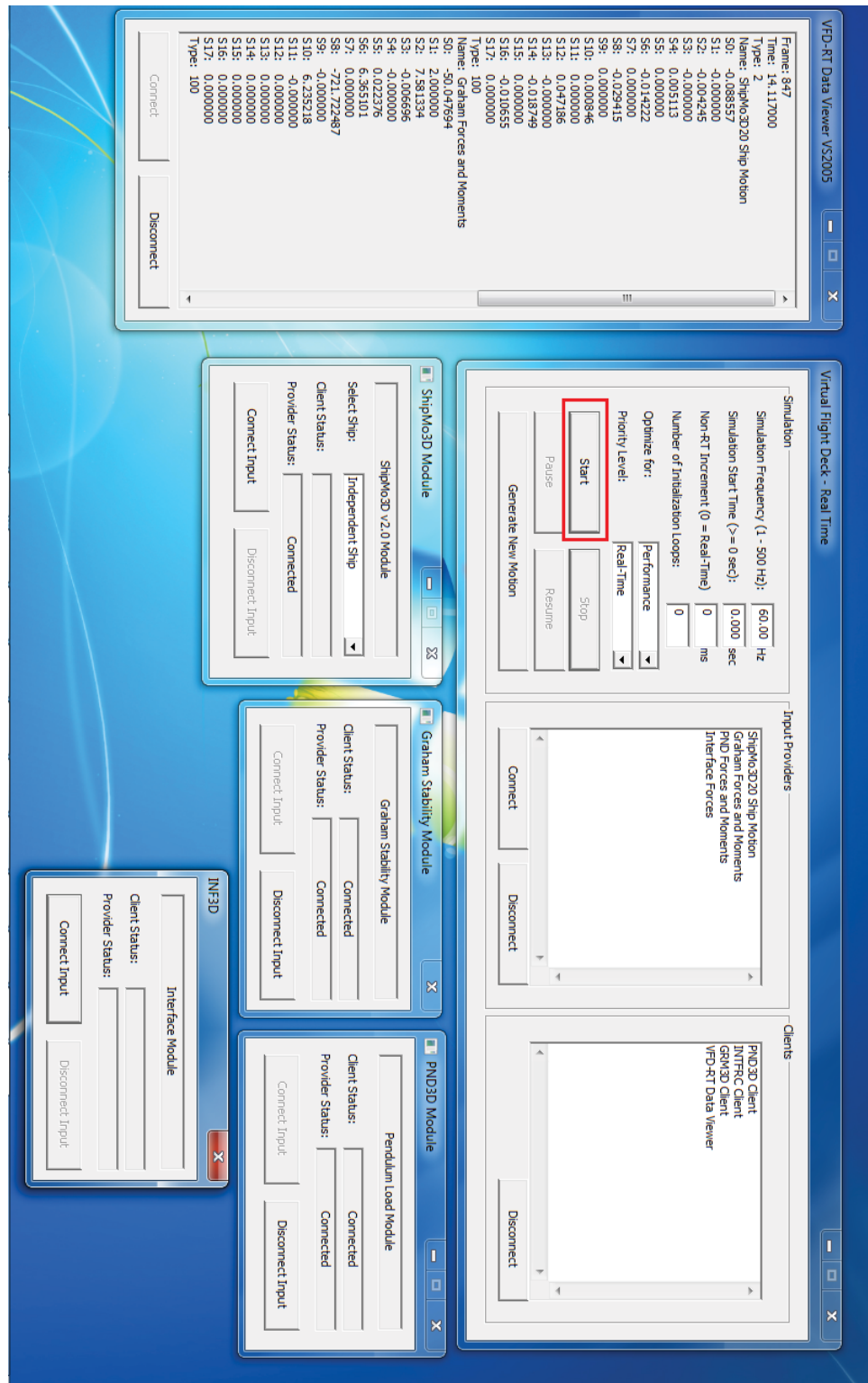


Figure F.5: PSM simulation running.

DOCUMENT CONTROL DATA		
(Security markings for the title, abstract and indexing annotation must be entered when the document is Classified or Designated.)		
1. ORIGINATOR (The name and address of the organization preparing the document. Organizations for whom the document was prepared, e.g. Centre sponsoring a contractor's report, or tasking agency, are entered in section 8.) Department of Aerospace and Mechanical Engineering, Carleton University 1125 Colonel By Drive, Ottawa, Ontario, K1S 5B6		2a. SECURITY MARKING (Overall security marking of the document, including supplemental markings if applicable.) UNCLASSIFIED
		2b. CONTROLLED GOODS (NON-CONTROLLED GOODS) DMC A REVIEW: GCEC APRIL 2011
3. TITLE (The complete document title as indicated on the title page. Its classification should be indicated by the appropriate abbreviation (S, C or U) in parentheses after the title.) Human Postural Stability Models		
4. AUTHORS (Last name, followed by initials – ranks, titles, etc. not to be used.) Langlois, R.; Bourgeois, N.; Leveille, M. J.; Morris, H.; Wice, A. M.		
5. DATE OF PUBLICATION (Month and year of publication of document.) November 2013	6a. NO. OF PAGES (Total containing information. Include Annexes, Appendices, etc.) 184	6b. NO. OF REFS (Total cited in document.) 91
7. DESCRIPTIVE NOTES (The category of the document, e.g. technical report, technical note or memorandum. If appropriate, enter the type of report, e.g. interim, progress, summary, annual or final. Give the inclusive dates when a specific reporting period is covered.) Contract Report		
8. SPONSORING ACTIVITY (The name of the department project office or laboratory sponsoring the research and development – include address.) Defence Research and Development Canada – Atlantic PO Box 1012, Dartmouth NS B2Y 3Z7, Canada		
9a. PROJECT OR GRANT NO. (If appropriate, the applicable research and development project or grant number under which the document was written. Please specify whether project or grant.) 11ge03	9b. CONTRACT NO. (If appropriate, the applicable number under which the document was written.) W7707-115204/001/HAL	
10a. ORIGINATOR'S DOCUMENT NUMBER (The official document number by which the document is identified by the originating activity. This number must be unique to this document.) DRDC Atlantic CR 2013-083	10b. OTHER DOCUMENT NO(s). (Any other numbers which may be assigned this document either by the originator or by the sponsor.)	
11. DOCUMENT AVAILABILITY (Any limitations on further dissemination of the document, other than those imposed by security classification.) <input checked="" type="checkbox"/> (X) Unlimited distribution <input type="checkbox"/> () Defence departments and defence contractors; further distribution only as approved <input type="checkbox"/> () Defence departments and Canadian defence contractors; further distribution only as approved <input type="checkbox"/> () Government departments and agencies; further distribution only as approved <input type="checkbox"/> () Defence departments; further distribution only as approved <input type="checkbox"/> () Other (please specify):		
12. DOCUMENT ANNOUNCEMENT (Any limitation to the bibliographic announcement of this document. This will normally correspond to the Document Availability (11). However, where further distribution (beyond the audience specified in (11)) is possible, a wider announcement audience may be selected.)		

13. ABSTRACT (A brief and factual summary of the document. It may also appear elsewhere in the body of the document itself. It is highly desirable that the abstract of classified documents be unclassified. Each paragraph of the abstract shall begin with an indication of the security classification of the information in the paragraph (unless the document itself is unclassified) represented as (S), (C), or (U). It is not necessary to include here abstracts in both official languages unless the text is bilingual.)

During naval operations in waves, loss of postural stability by crew members can cause degradations to operational effectiveness and safety. Motion-induced interruptions (MIIs) are often predicted using simplified models that assume a human being to be a rigid body. The accuracy of such models is often limited because they ignore the complexity of human dynamics. This report describes new postural stability models that consider the dynamics of humans subjected to external motions. The resulting models were validated experimentally at full scale using purpose-built physical apparatus representing the stability and load models as well as the coupling link between them. A comprehensive series of parametric experiments using the developed hardware was performed. The resulting validated models were then implemented in a distributed simulation environment.

14. KEYWORDS, DESCRIPTORS or IDENTIFIERS (Technically meaningful terms or short phrases that characterize a document and could be helpful in cataloguing the document. They should be selected so that no security classification is required. Identifiers, such as equipment model designation, trade name, military project code name, geographic location may also be included. If possible keywords should be selected from a published thesaurus. e.g. Thesaurus of Engineering and Scientific Terms (TEST) and that thesaurus identified. If it is not possible to select indexing terms which are Unclassified, the classification of each should be indicated as with the title.)

postural stability, motion-induced interruption, MII, distributed simulation, VFD-RT, shipboard mechanical systems, dynamic modelling

This page intentionally left blank.

Defence R&D Canada

Canada's leader in defence
and National Security
Science and Technology

R & D pour la défense Canada

Chef de file au Canada en matière
de science et de technologie pour
la défense et la sécurité nationale



www.drdc-rddc.gc.ca